

Institut für Ionenstrahlphysik und Materialforschung  
Helmholtz-Zentrum Dresden-Rossendorf

**Multiscale modeling of oxygen and vacancy diffusion in  
dilute ferritic iron alloys**

Dissertation

Zur Erlangung des akademischen Grades  
Doctor rerum naturalium (Dr. rer. nat.)

Vorgelegt der Fakultät Physik  
der Technischen Universität Dresden

von

Xiaoshuang Wang

geboren am 28. 07. 1991 in China

Eingereicht am 26.06.2020

Verteidigt am 26.10.2020

Gutachter:

1. Prof. Dr. Jürgen Faßbender (TU Dresden and HZDR)
2. Prof. Dr. Karsten Albe (TU Darmstadt)

## ABSTRACT

Iron-based ferritic alloys are used for a plethora of industrial applications. These alloys contain foreign atoms purposely employed to improve certain properties as well as some unwanted impurities introduced during fabrication. Materials properties are decisively influenced by diffusion processes. Very often diffusion cannot be avoided during fabrication and application. Therefore, many efforts are made to understand the underlying atomic-level mechanisms by both experimental and theoretical investigations. In this thesis work a multiscale modelling approach is used to study oxygen and vacancy diffusion in dilute ferritic iron alloys. Due to the extremely low solubility of oxygen the measurement of oxygen diffusion in iron is difficult. Only few experimental data are available. Experimental investigation of vacancy migration is still more complicated. The lack of reliable experimental data is therefore an important motivation for theoretical investigations. Gaining fundamental data on oxygen and vacancy diffusion in dilute iron alloys is essential for many applications. Oxygen plays a crucial role in the corrosion of iron-based alloys. Oxygen and the vacancy are also important in the formation and evolution of Y-Ti-O nanoclusters in oxide dispersion strengthened ferritic Fe-Cr alloys, which are considered as promising candidates for structural materials of future fusion and fission reactors. Furthermore, vacancies are formed during neutron and ion irradiation and their diffusion affects radiation-induced nanostructure formation in ferritic alloys.

In the first part of this thesis work, the diffusion of interstitial oxygen under the influence of substitutional atoms or solutes (Al, Si, P, S, Ti, Cr, Mn, Ni, Y, Mo and W) in bcc Fe is investigated by the combination of Density Functional Theory (DFT) and Atomistic Kinetic Monte Carlo (AKMC) simulations. The substitutional atoms are assumed to be immobile because oxygen diffusion is much faster than that of the solutes. DFT is applied to gain data on binding energies between interstitial oxygen and the substitutional foreign atoms, and to calculate the migration barriers for oxygen in the environment of the solutes. Using the migration barriers obtained by DFT, the diffusion coefficient of oxygen is determined by AKMC simulation. It is found that Si, P, Ni, Mo, and W have negligible influence on the oxygen diffusion coefficient. Al, Cr, Mn, S, Ti, and Y cause a considerable reduction of oxygen mobility. In these cases, the temperature dependence of oxygen diffusivity shows deviations from Arrhenius

behavior. This is explained in detail by the significant temperature dependence of the ratio between residence times in the respective states.

In the second part of the work a method is presented which allows for an efficient calculation of the diffusion coefficient of oxygen and other interstitial atoms in dilute alloys. The method is applied to examples considered in the first part of the work. The calculation procedure is based on the separation of the diffusion path into a contribution related to migration in the interaction region between the mobile interstitial and the substitutional solute and another part related to diffusion in perfect bcc Fe. In this manner AKMC simulation must be performed only for one concentration of the substitutional solute, and the obtained results can be employed to obtain data for other concentrations using analytical expressions containing binding energies between the interstitial and the substitutional solute.

The focus of third part of the work is on the mutual dependence of oxygen and vacancy diffusion in bcc Fe and dilute iron alloys. Here both O and v must be considered as mobile while the substitutional atoms are assumed to be immobile. DFT is applied to determine the binding energy between O and v for different distances, the migration barriers for O in the environment of v, and the corresponding barriers of v in the vicinity of O. In agreement with previous work O and v have a very strong binding at the 1<sup>st</sup> neighbor distance. On the other hand, the calculations show that the Ov pair at the 6<sup>th</sup> neighbor distance is unstable. The newly found simultaneous or coupled jumps of both O and v compensate the lack of jump paths that would occur due to this instability. The DFT results are employed to determine the diffusion coefficient of O and v using the scheme of the AKMC-based calculation method presented in the second part of the thesis work. At first a model system with fixed O and v concentrations is studied. It is found that a small v content of some ppm can already lead to a strong reduction of the O diffusivity. A similar effect is obtained for v diffusion under the influence of O. Furthermore, investigations on the interdependence of O and v diffusion during thermal processing of oxide dispersion strengthened iron alloys are performed, and the influence of the substitutional atoms Y and Ti is studied. A simple thermodynamic model is employed to determine the concentration of O, Y, and Ti monomers as well as the total v concentration, for a typical total content of O, Y, and Ti. These results are used in calculations of the diffusion coefficients of O and v. Not only a strong mutual dependence but also a significant influence of Y on O diffusion is

found. Finally, O and v diffusivities in a system with a total O content close to the thermal solubility are calculated. The monomer O concentration as well as the total v concentration was determined using two different models considering equilibrium of O and v with Ov, or equilibrium of O and v with Ov and O<sub>2</sub>v or Ov<sub>2</sub>. Despite the very small value of thermal solubility of O in bcc Fe, both the O and v diffusion coefficient are very different from that in pure iron. Even for such a low amount of O in the alloy the diffusion coefficients differ strongly from those in perfect bcc Fe.

The results of the present work have important consequences for planning and performing new experiments on O and v diffusion in dilute iron alloys. In particular, a very precise knowledge of the concentrations of O and v, as well as of other foreign atoms and traps such as dislocations is required.

# Contents

Chapter 1 Introduction .....	1
Chapter 2 Calculation Methods .....	5
2.1 Introduction .....	5
2.2 First-principle calculations .....	5
2.2.1 Many-electron Schrödinger equation .....	5
2.2.2 Density Functional Theory (DFT) .....	7
2.3 Theoretical treatment of diffusion processes .....	11
2.3.1 Determination of the jump rate .....	11
2.3.2 Calculation of the migration barrier by the Nudged Elastic Band method (NEB) ...	12
2.3.3 Calculation of the attempt frequency .....	13
2.3.4 Diffusion coefficient in a perfect crystal .....	14
2.3.5 Atomistic Kinetic Monte Carlo (AKMC) simulations on a rigid lattice .....	15
Chapter 3 Influence of substitutional atoms on the diffusion of oxygen in dilute iron alloys...	17
3.1 Introduction .....	17
3.2 DFT calculations .....	17
3.2.1 Calculation method .....	17
3.2.2 Migration barriers of oxygen in pure iron, attempt frequency .....	19
3.2.3 Binding energy of pairs consisting of an oxygen atom and a substitutional solute	20
3.2.4 Oxygen migration barriers in the environment of a substitutional solute .....	25
3.3 AKMC simulations .....	31
3.3.1 Simulation procedure .....	31
3.3.2 Diffusion coefficients of oxygen .....	32
3.4 Summary and conclusions .....	40
Chapter 4 Efficient calculation method for the diffusion coefficient of interstitial solutes in dilute alloys.....	42
4.1 Introduction .....	42
4.2 Calculation method .....	42
4.3 Results and discussion .....	45
4.3.1 The value of $D_{\text{inter}}$ .....	45
4.3.2 Time ratios .....	50
4.3.3 Total diffusion coefficient.....	51
4.4 Conclusions .....	54
Chapter 5 Mutual dependence of oxygen and vacancy diffusion in bcc Fe and dilute iron alloys .....	56
5.1 Introduction .....	56
5.2 DFT Calculations .....	56

5.2.1 Computational method .....	56
5.2.2 Binding energy of oxygen-vacancy pairs at different distances .....	58
5.2.3 Migration barriers .....	60
5.3 AKMC basics and determination of diffusion coefficients in a model system .....	66
5.3.1 The diffusion coefficient of oxygen in the presence of vacancies .....	67
5.3.2 The diffusion coefficient of the vacancy in the presence of oxygen .....	72
5.3.3 The diffusion coefficient of the oxygen-vacancy pair .....	73
5.4 Oxygen and vacancy diffusion in the first stage of thermal processing of ODS Fe-based alloys .....	75
5.5 Oxygen and vacancy diffusion in bcc Fe with an oxygen content close to the value of thermal solubility .....	84
5.6 Summary and conclusions .....	87
Chapter 6: Summary, conclusions and outlook .....	89
References: .....	93
Appendix-I .....	98
Appendix-II .....	103
Appendix-III .....	107
Appendix-IV .....	109
Appendix-V .....	111
Publication list .....	116
Curriculum Vitae .....	118
Acknowledgements .....	119
Erklärung .....	120

## Chapter 1 Introduction

Diffusion of foreign atoms such as dopants, impurities, and alloying elements may occur during fabrication, processing and operation of functional materials, and has a crucial influence on materials properties. It was found that diffusion proceeds via interstitial sites if the size of the migrating atom is smaller than that of the host atoms. Foreign atoms with sizes similar to or larger than those of the host material diffuse via the vacancy or the interstitialcy mechanism [1]. In this case vacancies and self-interstitials must be available. Since at thermal equilibrium the concentration of these point defects is very low, the migration via the vacancy and the interstitialcy mechanism is generally much slower than that via the interstitial sites. Most of previous experimental and theoretical studies of diffusion processes were focused on the migration of a single atomic species in a pure host material. However, the migration of one foreign atom may be also influenced by the presence of other foreign atoms of the same or another type, even if the concentration of foreign atoms of different kinds is still rather low.

Iron-based ferritic alloys are widely used in industrial applications. They always contain several foreign atoms or solutes. Some of them are impurities, others are purposely introduced in order to improve the mechanical properties, the corrosion and radiation resistance as well as the high-temperature stability. Many research activities are focused on the understanding of nanostructure evolution in these materials, under thermal and/or mechanical load and under irradiation. Multiscale modeling can substantially contribute to improve the knowledge on these processes. The general scheme is the following: At first data on migration barriers and binding energies of foreign atoms in bcc Fe are determined. Most advantageous and correct is the determination of these quantities by first-principle Density Functional Theory (DFT). Alternatively, available classical interatomic potentials may be employed in Molecular Statics or Dynamics calculations. In a second step Kinetic Monte Carlo simulations or rate theory are applied using the data determined in the first step as inputs. Atomistic Kinetic Monte Carlo (AKMC) simulation on a rigid lattice is a very suitable method in order to gain insight into many details of nanostructure evolution. Most of these simulations use rather simplified models in order to describe the migration barriers of foreign atoms, cf. e.g. the review paper of Becquart *et al.* [2]. Since these barriers are



the most important ingredients to describe the kinetics of a system, the results of that kind of simulations may be not sufficiently correct. Even in a multicomponent ferritic alloy containing foreign atoms with a rather low concentration the influence of the many different local atomic environments on the migration barrier should be taken into account precisely. This requires a huge effort since a very high number of barriers must be determined by DFT calculations. Recently, Messina *et al.* [3] presented an elegant neural-networks-based AKMC method to overcome these problems.

Oxygen (O) atoms and vacancies (v) play an important role in production and application of bcc-iron-based alloys. An example is Oxide Dispersion Strengthened ferritic Fe-Cr alloy, which is considered as promising candidate for structural materials of future fusion and fission reactors [4]. O and v have a crucial influence on formation and evolution of Y-Ti-O nanoclusters during the production of these materials. High concentrations of vacancies are formed during neutron and ion irradiation and their diffusion affects decisively radiation-induced nanostructure formation in the ferritic alloys. The behavior of O in these materials is also important for the electrochemical process of corrosion.

Measurements of O and v diffusion in bcc iron are difficult. In order to separate this diffusion from other effects experiments were mainly performed under conditions of thermal equilibrium, where O as well as v concentration is very small. However, in this case very small concentrations of foreign atoms or intrinsic defects may have a strong influence on the results. Only few experimental data on O diffusion are available. They were obtained many years ago using the method of internal oxidation of solutes which have a higher affinity to oxygen than iron [5-10]. Frank *et al.* [5] performed a critical review of experimental data published before 1967 and derived a value for the diffusion activation energy. In 1967 Swisher *et al.* [7] determined the O diffusion coefficient in bcc Fe from measurements at temperatures above about 970 K. In 1986 Takada *et al.* [8-10] published diffusion data obtained from experiments at temperatures between 1023 and 1173 K, i.e. mainly for the paramagnetic state of bcc Fe. Experimental investigation of v migration is still more complicated. In 1998 Seeger [11] estimated both the formation and migration energy of the vacancy using data obtained from self-diffusion, positron annihilation, and muon spin-rotation measurements. These data differ to the values determined by DFT methods. More recently, Hashimoto *et al.* [12] published an estimate of the v migration energy which is close to the theoretical results.

The lack of a comprehensive experimental data base on O and v diffusion in bcc Fe and the related alloys is an important motivation for theoretical investigations with the focus on a better understanding of the atomic-level mechanisms. A few theoretical studies on the influence of foreign atoms or vacancies on the diffusion of interstitial atoms in dilute ferritic alloys were performed in the past. Simonovic *et al.* [13] and Liu *et al.* [14] used combined DFT and AKMC calculations in order to treat the effect of different substitutional solutes on the diffusion of carbon. Barouh *et al.* [15] and Shang *et al.* [16] considered the influence of vacancies on the migration barriers of the interstitial solutes carbon, nitrogen and oxygen by means of DFT. Ortiz *et al.* [17] investigated the influence of carbon on He migration and clustering in bcc Fe using DFT and rate theory. The present work is also motivated by these previous studies.

The main objective of this thesis consists in gaining results on the effect of substitutional atoms on oxygen and vacancy migration in dilute iron alloys and on the mutual influence of on oxygen and vacancy diffusion.

The thesis consists of six chapters:

Chapter 1: Introduction

Chapter 2: Calculation methods:

- Fundamentals of Density Functional Theory (DFT) and Atomistic Kinetic Monte Carlo (AKMC) simulations.

Chapter 3: Influence of substitutional atoms on the diffusion of oxygen in dilute iron alloys:

- The influence of immobile Al, Si, P, S, Ti, Cr, Mn, Ni, Y, Mo, and W atoms on the migration of interstitial O is investigated. DFT is applied to determine binding energies and migration barriers, while the diffusion coefficient is calculated by AKMC simulations. For each solute concentration separate AKMC simulations are performed.

Chapter 4: Efficient calculation method for the diffusion coefficient of interstitial solutes in dilute alloys:

- An efficient calculation method is presented and applied to examples treated in Chapter 3. The new method only requires AKMC simulations for one concentration of substitutional atoms. In this manner the computational effort is

reduced considerably. The scheme of the efficient procedure is also applied in Chapter 5.

Chapter 5: Mutual dependence of oxygen and vacancy diffusion in bcc Fe and dilute iron alloys:

- DFT is employed to determine binding energies between O, v as well as Y and Ti substitutional atoms and the corresponding migration barriers of O (v) in the vicinity of the v (O), Y, and Ti. In AKMC simulations both O and v must be considered as mobile while the substitutional solutes are assumed to be immobile. Three different cases are studied: (i) A model system with fixed O and v concentrations, (ii) interdependence of O and v diffusion during thermal processing of oxide dispersion strengthened iron alloys, and (iii) O and v diffusion in a system with a total O content close to the thermal solubility.

Chapter 6: Summary, conclusions and outlook

## Chapter 2 Calculation Methods

### 2.1 Introduction

In this chapter, basics of the two calculations methods employed in this thesis, i.e. Density Functional Theory (DFT) and Atomistic Kinetic Monte Carlo (AKMC) is presented. In section 2.2 first-principle calculations are considered, starting from many-electron Schrödinger equation via the Hartree and the Hartree-Fock approximations towards DFT. In section 2.3 the theoretical treatment of diffusion processes is explained. This includes the calculation of the jump rate using DFT-based data for the migration energy barrier and the attempt frequency as well as the algorithm of AKMC simulations on a rigid lattice.

### 2.2 First-principle calculations [18-22]

#### 2.2.1 Many-electron Schrödinger equation

The Hamiltonian for a system of electrons and nuclei is given by

$$\begin{aligned}\hat{H} &= -\frac{\hbar^2}{2m_e} \sum_i \nabla_i^2 - \sum_{i,I} \frac{Z_I e^2}{|\vec{r}_i - \vec{R}_I|} + \frac{1}{2} \sum_{i \neq j} \frac{e^2}{|\vec{r}_i - \vec{r}_j|} - \sum_I \frac{\hbar^2}{2M_I} \nabla_I^2 + \frac{1}{2} \sum_{I \neq J} \frac{Z_I Z_J e^2}{|\vec{R}_I - \vec{R}_J|} \\ &= T_e + V_{Ne} + V_{ee} + T_N + V_{NN} \ ,\end{aligned}\tag{2.1}$$

where electrons are denoted by lower case subscripts, and nuclei (with charge  $Z_I$  and mass  $M_I$ ) are denoted by upper case subscripts. The terms in Hamiltonian are, in order, the electron kinetic energy, the Coulomb interaction between the electrons and nuclei, the Coulomb interaction between electrons, the nuclei kinetic energy, and the Coulomb interaction between nuclei. The atomic nuclei are much heavier than the electrons (each proton or neutron in a nucleus has more than 1800 times the mass of an electron). This means, electrons respond much more rapidly to changes in their surroundings than nuclei can. So the mathematical problems for the nuclei and electrons can be separated: When describing the motion of electrons, the position of the atomic nuclei is assumed to be fixed. Therefore, the following Hamiltonian can be used for the electrons

$$H = T_e + V_{Ne} + V_{ee} \ ,\tag{2.2}$$

This leads to the following (stationary) Schrödinger equation for  $N$  electrons

$$\left[ -\frac{\hbar^2}{2m_e} \sum_i \nabla_i^2 - \sum_{i,I} \frac{Z_I e^2}{|\vec{r}_i - \vec{R}_I|} + \frac{1}{2} \sum_{i \neq j} \frac{e^2}{|\vec{r}_i - \vec{r}_j|} \right] \psi_e = E_e \psi_e, \quad (2.3)$$

where  $\psi_e$  ( $\psi_e = \psi_e(r_1, r_2, \dots, r_N)$ , with  $r_i = (\vec{r}_i, \sigma)$ ,  $\sigma$  denotes the spin state) is the wave function for all electrons and  $E_e$  is their ground-state energy. The above equation describes a many-electron problem and cannot be generally solved. Therefore, approximations must be employed.

Neglecting all interactions between electrons,  $\psi_e$  can be written as  $\psi_e = \psi_1(\vec{r}_1, \sigma_1) \psi_2(\vec{r}_2, \sigma_2) \cdots \psi_N(\vec{r}_N, \sigma_N)$  ( $\sigma_i$  is the spin of electron  $i$ ) which corresponds to the Hartree approximation. Using the single-electron wave functions  $\psi_1, \psi_2, \dots, \psi_N$ , the density of electrons is determined by  $n(\vec{r}) = \sum_{i,\alpha} \psi_i^*(\vec{r}, \sigma_\alpha) \psi_i(\vec{r}, \sigma_\alpha)$ , and the interaction of a given electron with all the others can be described by the Hartree potential  $V_H(\vec{r}) = e^2 \int \frac{n(\vec{r}')}{|\vec{r} - \vec{r}'|} d^3 r'$ . In this manner the many-electron Schrödinger equation is separated in a system of  $N$  coupled equations for the single-electron wave functions.

The approximation of Fock took into account the fact that electrons are fermions, i.e. that the all-electron wave function has to be antisymmetric with regard to exchange of variables  $(r_i, \sigma_i)$ , which is in agreement with the Pauli exclusion principle. This led to the use of the Slater determinant instead of the Hartree product

$$\psi_e = \frac{1}{\sqrt{N!}} \begin{vmatrix} \psi_1(\vec{r}_1, \sigma_1) & \psi_1(\vec{r}_2, \sigma_2) & \cdots & \psi_1(\vec{r}_N, \sigma_N) \\ \vdots & \vdots & \ddots & \vdots \\ \psi_N(\vec{r}_1, \sigma_1) & \psi_N(\vec{r}_2, \sigma_2) & \cdots & \psi_N(\vec{r}_N, \sigma_N) \end{vmatrix} \quad (2.4)$$

The use of this expression results in  $N$  coupled (Hartree-Fock) equations for the single-electron wave functions  $\psi_1, \psi_2, \dots, \psi_N$  of the Slater determinant. In this case, the electron-electron interaction is not only described by the Hartree potential, but also by the Fock or exchange potential (for the interaction of a given electron with all the others)

$$V_{ex}(\vec{r}) = -\sum_{j \neq i} \int \frac{e^2}{|\vec{r} - \vec{r}'|} \frac{\psi_j^*(\vec{r}', \uparrow) \psi_i(\vec{r}', \uparrow) \psi_j(\vec{r}, \uparrow)}{\psi_i(\vec{r}, \uparrow)} d^3 r' = -e^2 \int \frac{n_{ex}^{i, \uparrow}(\vec{r}, \vec{r}')}{|\vec{r} - \vec{r}'|} d^3 r' \quad (2.5)$$

The consideration of spin variables shows that the exchange potential describes the interaction of electrons with parallel spins, with a non-local “charge density”  $n_{ex}^{i, \uparrow}(\vec{r}, \vec{r}')$  that also depends on state  $i$  of the electron under consideration. The Fock potential is therefore a purely quantum-mechanical quantity.

It must be mentioned that the energy of the ground-state obtained from Hartree-Fock equations is still above the true ground state energy. This is because correlation energy is not included due to the approximation introduced by using the Slater determinant. This error arises because the interaction of one electron with another is treated as the interaction with a smoothed out, averaged electron density. In fact, the position of one electron affects the position of the other electron, because they repel each other. Their positions are correlated, an effect not included in the Hartree-Fock approximation. On the other hand, applications of the Hartree-Fock equations to solid state physics would lead to a huge computational effort. For example, in the case of a nanocluster with 100 Pt atoms a system of 7800 coupled equation must be solved iteratively.

### 2.2.2 Density Functional Theory (DFT)

The subject of Density Functional Theory (DFT) is the (nondegenerate) ground state of an interacting many-electron system under the influence of an external (e.g. lattice) potential. DFT is based on the fundamental work of Hohenberg, Kohn, and Sham [18,21,22]

Their findings can be summarized as follows:

*The ground-state energy is a unique functional of the ground-state electron density. The electron density that minimizes the energy functional is the true ground-state electron density which corresponds to the full solution of the many-electron Schrödinger equation.*

In this manner, the problem of solving the many-electron Schrödinger equation, with the ground-state wave function depending on  $3N$  coordinates is replaced by the

search for the minimum of the energy functional with respect to the electron density  $n(\vec{r})$  which depends only on three spatial coordinates.

The ground state energy as functional of the electron density may be written as

$$E[n(\vec{r})] = T + V[n(\vec{r})] + U[n(\vec{r})] \quad (2.6)$$

where  $T$ ,  $V$ , and  $U$  are the functional of the kinetic energy, of the potential energy due to the external potential, and of the potential energy of the electron-electron interaction, respectively. In the case of a solid with  $V_{en}$  as the Coulomb interaction (attraction) between one electron and the nuclei in a lattice, the expression for  $V$  is given by

$$V[n(\vec{r})] = -\int \frac{Z_l e^2}{|\vec{r} - \vec{R}_l|} n(\vec{r}) d^3 r \quad (2.7)$$

The quantity  $U$  describes the electrostatic interaction (repulsion) between the electrons, as well as their interaction due to the quantum-mechanical exchange and correlation effects

$$U[n(\vec{r})] = \frac{e^2}{2} \int \frac{n(\vec{r})n(\vec{r}')}{|\vec{r} - \vec{r}'|} d^3 r d^3 r' + V_{xc}[n(\vec{r})] \quad (2.8)$$

Furthermore, it is assumed that the kinetic energy  $T$  can be written in the same manner as in the case of a non-interacting electron system

$$T = \sum_{i=1}^N \int \psi_i^*(\vec{r}) \left( -\frac{\hbar^2 \nabla^2}{2m} \right) \psi_i(\vec{r}) d^3 r, \quad (2.9)$$

where  $\psi_i(\vec{r})$  is a (still unknown) single-electron wave function. Using the last expression, one implicitly assumes that the (still unknown) ground-state electron density may be related to an effective single-electron Hamiltonian. This is not an explicitly verified fact. However, such an expression is generally used in DFT, since the consideration of single-particle wave functions simplifies the formalism. On the other hand, certain approximations must be employed for the functional  $V_{xc}[n(\vec{r})]$  so that the ansatz for  $T$  is not the only uncertainty. On the other hand, a proper choice of the functional  $E_{xc}[n(\vec{r})]$  may compensate the error made by this ansatz.

The unique relation between  $n(\vec{r})$  and  $\psi_i(\vec{r})$  ( $n(\vec{r}) = \sum_i \psi_i^*(\vec{r})\psi_i(\vec{r})$ ) enables to perform the minimization of  $E[n(\vec{r})]$  with respect to  $\psi_i(\vec{r})$  which leads to the Kohn-Sham equations

$$\left[ -\frac{\hbar^2}{2m_e} \nabla^2 - \sum_I \frac{Z_I e^2}{|\vec{r} - \vec{R}_I|} + e^2 \int \frac{n(\vec{r}')}{|\vec{r} - \vec{r}'|} d^3r' + \frac{\delta V_{XC}[n(\vec{r})]}{\delta n(\vec{r})} \right] \psi_i(\vec{r}) = \varepsilon_i \psi_i(\vec{r}) \quad (2.10)$$

This corresponds to a single-electron Schrödinger equation for  $\varepsilon_i$  and  $\psi_i$  with an effective potential. Strictly speaking,  $\varepsilon_i$  and  $\psi_i$  are auxiliary quantities to be used to determine the electronic density  $n(\vec{r})$ . On the other hand, in practice these quantities are employed to determine certain ground-state properties as momentum distribution of electrons etc.

The Kohn-Sham equations are solved in an iterative way:

1. Define an initial electron density  $n(\vec{r})$
2. Solve the Kohn-Sham equations using the initial density or the density obtained in the preceding iterative step to find the single-electron wave function  $\psi_i(\vec{r})$
3. Calculate the new electron density  $n(\vec{r}) = \sum_i \psi_i^*(\vec{r}) \psi_i(\vec{r})$  by the wave function determined by step 2.
4. Compare the calculated electron density with that of the preceding iteration step. If the two densities are different, then go to step 2 and continue. Otherwise, the obtained electron density is considered the true ground-state density and this density can be used to calculate the (total) ground state energy. In practice the total energies obtained for two successive iteration steps are compared and the iteration is stopped if the difference falls below a certain threshold (see below).

The accuracy of Kohn-Sham approach is only limited by the approximations in the exchange-correlation (XC) functional. These approximations are mainly based on the theory of a homogeneous electron gas with a positively charged homogenous background introduced for reason of charge compensation. This model system is also called jellium. In the Local Density Approximation (LDA) it is assumed that the functional dependence of  $V_{XC}$  on the (constant) electron density of the jellium may be also used for the nonhomogeneous case treated in DFT, i.e.  $V_{XC} = V_{XC}^{LDA}[n(\vec{r})]$ . The next level of approximation is to include the local gradient of the electron density, which is called Generalized Gradient Approximation (GGA):  $V_{XC} = V_{XC}^{LDA}[n(\vec{r}), \nabla n(\vec{r})]$ . Two of most popular GGA functionals are the Perdew-Wang (PW91) [23] and the Perdew-



Burke-Ernzerhof (PBE) functional [24]. The latter is employed in the present work in the framework of DFT calculations using the Vienna Ab-Initio Simulation Package (VASP) [25-27].

In many applications of DFT it is not necessary to consider all electrons since properties arising from the type of chemical bonding are dominated by the less tightly bound valence electrons. Therefore, the pseudopotential concept was introduced to avoid the use of core-electron wave functions which exhibit many oscillations and may lead to significant computational effort. A pseudopotential replaces the electron density of a set of core electrons by a smoothed density, which is chosen to match various important physical and mathematical properties of the true ion core. There are many kinds of pseudopotentials provided by current DFT codes. Most frequently, ultrasoft pseudopotentials (USPPs) [28] and pseudopotentials determined by the projector augmented wave (PAW) method [29,30] are employed. The latter are used in the present work.

In many DFT codes such as in VASP plane-wave-based functions are used as Kohn-Sham wave functions ( $\psi_i$ , see above) for the valence electrons with

$$\psi_{\vec{k}}(\vec{r}) = e^{i\vec{k}\vec{r}} u_{\vec{k}}(\vec{r}) = e^{i\vec{k}\vec{r}} \sum_{\vec{G}} c_{\vec{k},\vec{G}} e^{i\vec{G}\vec{r}} = \sum_{\vec{G}} c_{\vec{k},\vec{G}} e^{i(\vec{k}+\vec{G})\vec{r}} \quad (2.11)$$

where  $\vec{k}$  is the wave vector. The function  $\psi_{\vec{k}}(\vec{r})$  is chosen in such manner that the Bloch theorem valid for periodic structures is obeyed

$$\psi_{\vec{k}}(\vec{r} + \vec{R}) = e^{i\vec{k}\vec{R}} \psi_{\vec{k}}(\vec{r}) \quad (2.12)$$

where  $\vec{R}$  is a vector that characterizes the translational symmetry (e.g. a lattice vector) in the real space while  $\vec{G}$  is the corresponding quantity in the reciprocal space or lattice. The number of components in the above Fourier expansion can be limited by defining a fixed energy cutoff  $E_{cut}$  and all expansion coefficients  $c_{\vec{k},\vec{G}}$  related to an energy

$\frac{\hbar^2(\vec{k} + \vec{G})^2}{2m_e} > E_{cut}$  are neglected. Such a truncation is possible since the contribution from higher Fourier components or large  $|\vec{k} + \vec{G}|$  is small. In applications test calculations must be performed in order to find the convergence of the total energy versus  $E_{cut}$ .

In DFT calculations on defects, substitutional atoms, etc., such as performed in the present work, supercells are considered as a representative part of the material. Periodic boundary conditions are applied since translational invariance, i.e. homogeneity of the material, is assumed. In this case the vector  $\vec{R}$  is related to the size of the supercell. In the reciprocal space the supercell corresponds to the first Brillouin zone.

Using the above Fourier expansion, the Kohn-Sham equations can be treated within the reciprocal space and the required quantities can be calculated for a finite number of  $\vec{k}$  points in the first Brillouin zone. Symmetry consideration may allow for the consideration of the so-called Irreducible Brillouin Zone (IBZ). DFT simulation packages such as VASP employ special algorithms to generate a suitable  $\vec{k}$ -point grid for the IBZ, e.g. the widely used Monkhorst-Pack method [31]. In applications the optimum number of  $\vec{k}$ -points must be obtained by test calculations that check the convergence of the total energy versus the number of  $\vec{k}$ -points.

## 2.3 Theoretical treatment of diffusion processes

### 2.3.1 Determination of the jump rate

Diffusion processes can be treated as sequences of atomic jumps from one potential energy minimum to another via a transition state. In the Transition State Theory (TST) [32] it is generally assumed that the residence time of an atom in a state that corresponds to an energetic minimum is much longer than the time of transition to another minimum (or equilibrium) state. Therefore, forward and backward jumps are considered uncorrelated. The harmonic TST offers a very good approximation to calculate the jump rate. The main assumptions of the harmonic TST are [33]: i) The transition pathway from one energetic minimum to another is well characterized by a saddle point on the potential energy surface; ii) the vibrational modes are harmonic near the minimum states on the potential energy surface, and (iii) the vibrational modes are also harmonic perpendicular to transition pathway at the saddle point. The harmonic TST yields the following expression for the jump rate [32]:

$$\nu = \nu_0 \exp\left(\frac{-E_m}{k_B T}\right) \quad (2.13)$$

where  $E_m$  is difference between the energy at the saddle point and the energy of minimum from which the jump starts. The quantity  $E_m$  is called jump barrier, migration barrier, or migration energy. The prefactor  $\nu_0$  is the attempt frequency of the jump and may be determined by

$$\nu_0 = \frac{\prod_{i=1}^{3N-3} \nu_i^{\min}}{\prod_{i=1}^{3N-4} \nu_i^{SP}} \quad (2.14)$$

Here a system consisting of  $N$  atoms is considered, where  $\nu_i^{\min}$  and  $\nu_i^{SP}$  denote the vibrational frequencies of the system at the minimum and the saddle point, respectively. Since at the saddle point only vibrational modes perpendicular to the transition pathway exist, the product in the denominator contains one factor less than that in the numerator.

### 2.3.2 Calculation of the migration barrier by the Nudged Elastic Band method (NEB)

In the present work NEB [34,35] is employed in connection with DFT calculations in order to determine the migration barrier and the minimum energy path (MEP), provided that the initial and the final (minimum or equilibrium) state is known. Note that MEP is another term for the transition pathway. In NEB the minimum-energy states before and after a diffusive jump are connected by a number of images using harmonic springs (the elastic band). Each image corresponds to a certain state of the whole system of  $N$  atoms. For each image  $i$ ,  $3N$  dimensional vectors  $\mathbf{R}_i$  and  $\mathbf{F}_i$  characterize the positions of  $N$  atoms and the forces on these atoms. The NEB force on image  $i$  is given by

$$\mathbf{F}_i^{NEB} = \mathbf{F}_i^\perp + \mathbf{F}_i^{SP} = \mathbf{F}_i^\perp + K \left( |\mathbf{R}_{i+1} - \mathbf{R}_i| - |\mathbf{R}_i - \mathbf{R}_{i-1}| \right) \boldsymbol{\tau}_i \quad (2.15)$$

where  $\mathbf{F}_i^{SP}$  is the spring force,  $K$  is the spring constant, and  $\boldsymbol{\tau}_i$  is the normalized local tangent at image  $i$  which may be determined using the

$$\boldsymbol{\tau}_i = \frac{\mathbf{R}_{i+1} - \mathbf{R}_{i-1}}{|\mathbf{R}_{i+1} - \mathbf{R}_{i-1}|} \quad (2.16)$$

and

$$\mathbf{F}_i^\perp = \mathbf{F}_i - (\mathbf{F}_i \boldsymbol{\tau}_i) \boldsymbol{\tau}_i \quad (2.17)$$

is the perpendicular part of the true force  $\mathbf{F}_i$  on image  $i$ . In the equation for  $\mathbf{F}_i^{NEB}$  the spring force allows the band to maintain a spread distribution of images, while the perpendicular part of the true force is directed towards the MEP. For all images an iterative minimization of  $\mathbf{F}_i^{NEB}$  is performed which is achieved by a (restricted) relaxation of both the electronic states and the atomic positions using the DFT calculation procedure. The real MEP with the migration barrier is considered to be reached if all  $\mathbf{F}_i^{NEB}$  approach zero, i.e. if the NEB force on all atoms of the different images becomes lower than a given threshold.

However, there is no guarantee that the image with the highest energy found by NEB calculation is identical with the saddle point. The true transition state can be obtained using the Climbing-Image Nudged Elastic Band method (CINEB). In CINEB the images determined by standard NEB are employed as input data. Then, the procedure described above is applied once more, with the exception that the NEB force on the image with highest energy  $\mathbf{F}_{i_{max}}^{NEB}$  is replaced by

$$\mathbf{F}_{i_{max}}^{NEB} = \mathbf{F}_{i_{max}} - 2\mathbf{F}_{i_{max}} \boldsymbol{\tau}_{i_{max}} \quad (2.18)$$

which corresponds to a modified true force where the component along the tangent is reversed.

In this work the so-called vtsttools [36] provided by the Henkelman group at the University of Texas (Austin) were employed in all application of NEB and CINEB.

### 2.3.3 Calculation of the attempt frequency [37]

According to Eq.(2.14) the attempt frequency  $\nu_0$  depends on the vibrational modes  $\nu_i^{\min}$  and  $\nu_i^{SP}$  of the system of  $N$  atoms. The value of  $\nu_0$  is often in the range of  $10^{12}$ - $10^{13}$  s<sup>-1</sup>, so that a common approximation is to choose a fixed value in this range to save the computational work of computing the vibrational modes. In the present work the attempt frequency is determined via Eq.(2.14) only for nearest-neighbor oxygen and vacancy jumps in perfect bcc Fe. The vibrational or normal modes are calculated using the method implemented in the DFT code VASP which employs the harmonic approximation and the frozen phonon approach. The main tasks consist in the calculation of forces on atoms for a predefined set of displacements from their

equilibrium positions, and the subsequent diagonalization of the so-called dynamical matrix  $\Phi_{\alpha\beta}^{ij}$  that contains the force derivatives

$$\Phi_{\alpha\beta}^{ij} = \frac{\partial F_{\alpha}^i}{\partial u_{\beta}^j} \quad (2.19)$$

where  $i$  and  $j$  denote the different atoms and  $\alpha$  and  $\beta$  denote the Cartesian coordinates  $(x, y, z)$ , i.e.  $u_{\beta}^j$  means the displacement of atom  $j$  in direction  $\beta$ , while  $F_{\alpha}^i$  is the force on atom  $i$  in direction  $\alpha$ .

### 2.3.4 Diffusion coefficient in a perfect crystal

The diffusion coefficient of the interstitial oxygen atom or of the vacancy in a perfect crystal may be obtained from the general formula [38]

$$D = \frac{n_p v l^2}{2d} \quad (2.20)$$

with the jump rate  $v$ , jump length  $l$ , and the dimension of the diffusion  $d$ , as well as the number of possible equivalent jumps  $n_p$  of the diffusing atom (or vacancy) from a given position. In the case of bcc Fe and oxygen diffusion via jumps between nearest neighbor octahedral interstitial sites, the quantities  $n_p$ ,  $d$ , and  $l$  are given by

$$n_p = 4 \quad , \quad d = 3 \quad , \quad l = a/2 \quad (a: \text{lattice constant of bcc Fe}), \quad (2.21)$$

while for the diffusion of the vacancy one obtains

$$n_p = 8 \quad , \quad d = 3 \quad , \quad l = \frac{\sqrt{3}}{2} a \quad (2.22)$$

Using Eq. (2.13) for the jump rate the oxygen and the vacancy diffusion coefficients in bcc Fe are given by

$$D_o = \frac{a^2}{6} v_0^o \exp\left(\frac{-E_m^o}{k_B T}\right) \quad (2.23)$$

and

$$D_v = a^2 v_0^v \exp\left(\frac{-E_m^v}{k_B T}\right) \quad (2.24)$$

### 2.3.5 Atomistic Kinetic Monte Carlo (AKMC) simulations on a rigid lattice

If the jump rate depends on the local atomic environment of the diffusing atom in most cases AKMC simulations must be applied to determine the diffusion coefficient. In this section the algorithm of AKMC simulations is explained for the case considered in Chapters 3 and 4, i.e. oxygen diffusion under the influence of substitutional atoms in bcc Fe. In these chapters AKMC simulations are applied to dilute alloys where the concentration of the substitutional solutes is small. The simulation cell contains simple cubic (sc) lattice sites consisting of the bcc lattice sites and the octahedral interstitial sites of the bcc lattice. 3d periodic boundary conditions are applied. At the beginning of the simulation the position of the substitutional atom or solute is randomly chosen. The substitutional atom is assumed to be immobile and the size of simulation cell corresponds to the concentration for which the AKMC simulation is performed. Oxygen is mobile and may jump from one octahedral interstitial site to a neighboring octahedral interstitial site since at such positions O is most stable. The AKMC step number and the physical time are set to 0 at the beginning of the simulation. The main part of the AKMC code deals with the determination of possible foreign-atom neighbors of the oxygen atom before and after a jump. For this purpose, linked cells and neighbor lists are used which are determined at the very beginning of the simulations. At each AKMC step, O may jump into 4 directions which are geometrical equivalent but may exhibit different jump rates  $\nu_i$  if oxygen is in the environment of a substitutional atom. The jump rates  $\nu_i$  ( $i=1, \dots, 4$ ) are determined by  $\nu_i = \nu_0 \exp(\frac{-E_m^i}{k_B T})$ , with the migration barrier  $E_m^i$  and the (unique) attempt frequency  $\nu_0$ . Furthermore, the cumulative function  $\sum_{j=1}^i \nu_j$  as well as the probability  $p_i = \sum_{j=1}^i \nu_j / \sum_{j=1}^4 \nu_j$  are calculated. A jump event  $k$  is selected using a random number  $r$  (uniformly distributed between 0 and 1):  $p_{k-1} < r < p_k$ . Then the jump is carried out, i.e., the position of the oxygen atom is changed. The AKMC step number is increased by 1 and the physical time is increased by  $\Delta t = -\ln(r) / \sum_{j=1}^4 \nu_j$  with another random number  $r$ . The procedure described above that corresponds to the well-known rejection-free AKMC algorithm [33] is repeated many times and the position of the O atom is recorded as a function of physical time.

In order to obtain good statistics, the migration of the oxygen atom is simulated many times, with different initial positions of the oxygen and the foreign atom.

After AKMC simulation, the diffusion coefficient of oxygen atom is determined in the following manner [39-41]. The recorded trajectory of O is decomposed into  $n_s$  time segments  $\delta t$ , and for each segment the squared displacement  $sd(m) = (\vec{x}(t_m) - \vec{x}(t_{m-1}))^2$  with  $t_m = t_{m-1} + \delta t$  is determined, where  $\vec{x}$  denotes the position of O at given time. Then, the diffusion coefficient is obtained from  $D = \frac{1}{n_s} \sum_{m=1}^{n_s} \frac{sd(m)}{6\delta t}$ .

Within certain limits, the length of the segments determined by  $\delta t$  and their number  $n_s$  can be chosen arbitrarily so that the calculation of the diffusion coefficient can be performed for many different subdivisions of the trajectory, and, finally the results are averaged. However, there is a limitation for the choice of  $\delta t$  and  $n_s$ : On the one hand,  $\delta t$  should be large enough to include all local jump correlations, on the other hand,  $n_s$  should be large enough to provide a statistically meaningful diffusion coefficient.

## **Chapter 3 Influence of substitutional atoms on the diffusion of oxygen in dilute iron alloys**

### **3.1 Introduction**

It is known from literature that in bcc Fe the most stable position of O is the octahedral interstitial site and the tetrahedral interstitial site is the saddle point for first-neighbor jumps [14,16,42-44]. In this chapter it is investigated how the presence of foreign atoms modifies the O migration. In the first part jumps of oxygen in pure bcc Fe, between first-, second-, and third-neighbor octahedral interstitial sites are investigated by DFT. Then, DFT is applied to determine the binding energy between oxygen and a foreign atom, for different neighbor distances, and to calculate the modified migration barriers, i.e. for the oxygen jump between the first and the second neighbor of a foreign atom, etc. Using the migration barriers obtained by DFT the diffusion coefficients of oxygen are determined by AKMC simulations considering a dilute iron alloy on a rigid lattice. Finally, a detailed discussion on the influence of the different foreign atoms on the oxygen diffusivity is performed.

### **3.2 DFT calculations**

#### **3.2.1 Calculation method**

The Vienna ab-initio simulation package VASP [25-27] was applied to perform the DFT calculations. Plane wave basis sets and pseudopotentials generated within the projector-augmented wave (PAW) approach [29,30] were used and the exchange and correlation effects were treated by the Perdew-Burke-Ernzerhof (PBE) parameterization [24] of the generalized gradient approximation (GGA). In all calculations the spin polarized formalism was applied and a plane wave cutoff of 500 eV was used. The Brillouin zone sampling was performed employing the Monkhorst-Pack scheme [31]. The calculations were carried out for cubic bcc-Fe supercells with 128 lattice sites and  $3 \times 3 \times 3$   $k$  points. For the integration in the reciprocal space the Methfessel-Paxton smearing method [45] was applied with a width of 0.2 eV. After introduction of an oxygen atom on an octahedral interstitial site and of another foreign atom on a substitutional site the positions of atoms as well as the volume and shape of the supercell were relaxed so that the total stress/pressure on the supercell became zero. Such calculations were performed for different distances between the oxygen and the foreign atom as illustrated in Fig. 3.1. The notation of the neighbor positions of



oxygen relative to the foreign atom is according to the scheme for a simple cubic lattice (cf. [15]) which consists of the bcc lattice sites and the octahedral interstitial sites of the bcc lattice. Note that within this scheme oxygen cannot reside on third, fourth, seventh, eighth, etc. neighbor positions since these sites are already occupied by iron atoms, and that there are two different ninth neighbor sites (9a and 9b). The accuracy of DFT calculations is determined by two criteria: (i) If the residual force acting on any atom falls below a given threshold the relaxation calculation is stopped. (ii) At each relaxation step the energy minimization is performed until the total energy change falls below another threshold. In the present work threshold values of  $10^{-2}$  eV/Å and  $10^{-5}$  eV are used, in first and the second case, respectively. The binding energy between a foreign atom  $X$  on a substitutional site and the oxygen  $O$  on an octahedral interstitial site, at different distances to the foreign atom (cf. Fig. 3.1), is defined by

$$E_{bind} = E(X+O) + E_0 - E(X) - E(O) \quad (3.1)$$

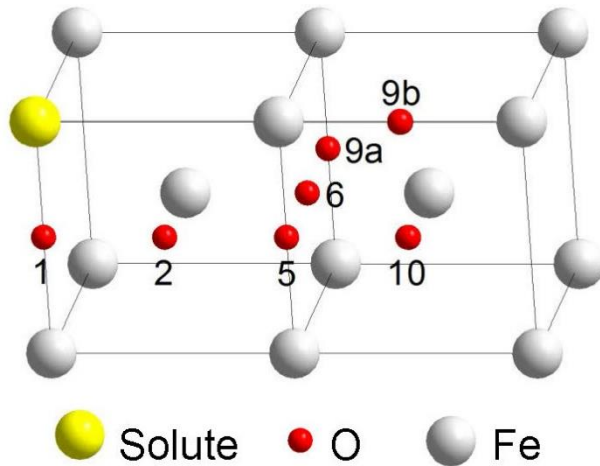


**Figure 3.1** Octahedral interstitial sites for oxygen in the neighborhood of a substitutional atom (or solute). The notation of oxygen positions relative to the foreign atom is according to the scheme for a simple cubic lattice that consists of the bcc lattice sites and the octahedral interstitial sites of the bcc lattice.

$E(X+O)$ ,  $E(X)$ , and  $E(O)$  denote the total energy of (iron)supercells with the defect pair  $X+O$  and the monomers  $X$  and  $O$ , respectively, while  $E_0$  is the total energy of the supercell with perfect bcc Fe. By definition the value of  $E_{bind}$  is negative in the case of attraction between the  $X$  and the  $O$  atoms.

The migration energy barriers for oxygen in perfect bcc Fe and in the environment of a substitutional atom are calculated using the combination of standard NEB and

CINEB methods as described in section 2.3.2. Furthermore, the attempt frequency is determined as outlined in sections 2.3.1 and 2.3.3, i.e. by using the vibrational frequencies of the supercell at the minimum state (before the O jump) and at the saddle point. In order to obtain reasonable data for these frequencies the minimum and saddle point states must be calculated with a very high precision. In this case threshold values of  $10^{-4}$  eV/Å and  $10^{-7}$  eV were used for the residual force on atoms and the total energy change (see above), respectively.

### 3.2.2 Migration barriers of oxygen in pure iron, attempt frequency

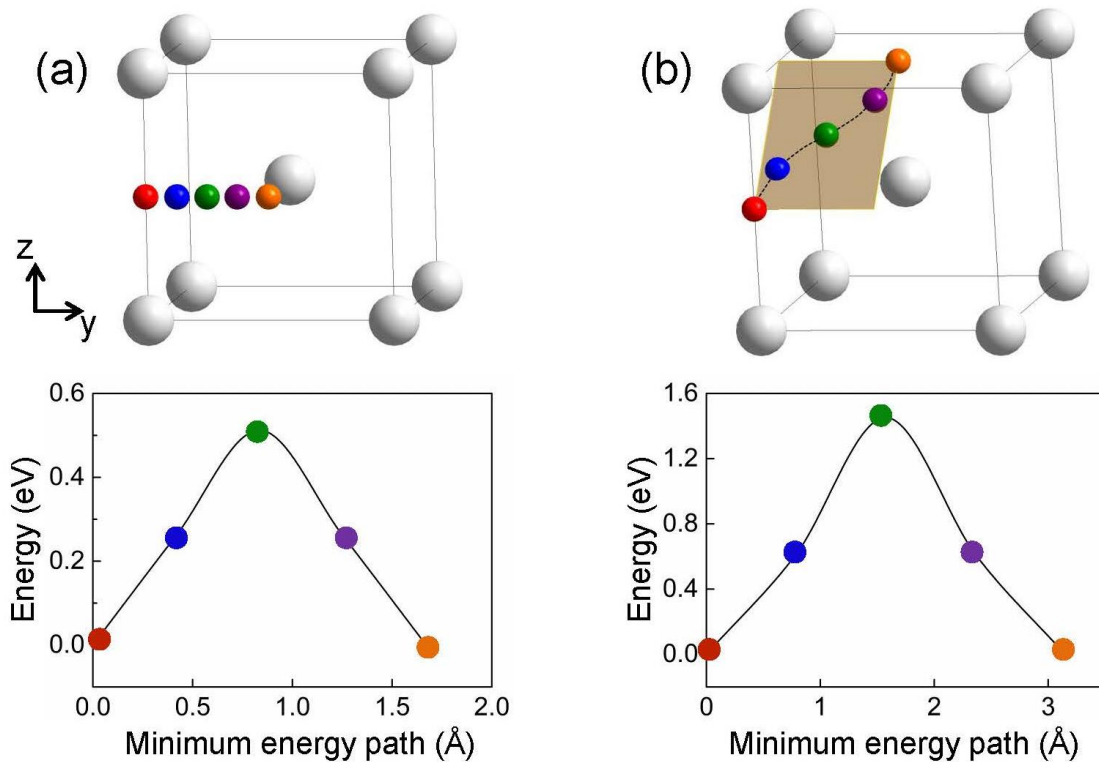


**Figure 3.2** Illustration of the minimum energy paths for the jump of oxygen between first neighbor (a) and third-neighbor (b) octahedral interstitial sites in pure bcc Fe.

The octahedral interstitial site is the most stable site of oxygen in pure bcc Fe [42-44,46-48]. It was shown that the incorporation of O into the lattice leads to a local tetragonal distortion and a corresponding change of the supercell shape is observed if relaxation calculation is performed under zero stress/pressure conditions [48]. Three different migration paths of oxygen in pure bcc Fe were investigated in this work: between (i) first-neighbor, (ii) second-neighbor, and (iii) third-neighbor octahedral sites. The results are shown in Fig. 3.2. The first-neighbor jump consists of a linear migration

path with a barrier of 0.512 eV. This value is consistent with previous DFT calculations of Fu *et al.* [42], Claisse *et al.* [44], Shang *et al.* [16], Barouh *et al.* [15] and Samin *et al.* [49] who obtained 0.6, 0.48, 0.526, 0.56, and 0.451 eV, respectively. The saddle point situated in the middle of the path corresponds to a tetrahedral interstitial site of the bcc lattice, cf. Fig. 3.2(a). Note that the data points correspond to the calculated values which are used to obtain the fit curve. It is worth mentioning that the tetragonal distortions in the initial and the final state differ: While in the initial state the elongation is along the z axis it is along the x axis in the final state. A tetragonal distortion is also observed at the saddle point. However, in this case the dimensions of the supercell in x and z directions are equal and slightly higher than in y direction. It was found by NEB calculations that a second-neighbor jump consists of two successive first-neighbor jumps. This was also reported for carbon migration in bcc Fe [13] which occurs in a similar manner as the oxygen diffusion, i.e. between octahedral interstitial sites. The third-neighbor jump consists of a nonlinear migration path as shown in Fig. 3.2(b). The saddle point, a rhombohedral interstitial site, is in the middle of the minimum energy path, with a barrier height of 1.452 eV. This result is also similar to the findings for carbon [13]. The barrier for the third-neighbor jump is considerably higher than that for a first-neighbor jump. For such a jump the probability of occurring is therefore much smaller than that for three consecutive first-neighbor jumps. Based on above results, in the following only first-neighbor jumps are considered. For a first-neighbor jump the attempt frequency was determined according to the formalism outlined in Eqs. (2.14) in Chapter 2 and a value of 15.76 THz was obtained in the temperature range relevant for diffusion (above 500 K).

### **3.2.3 Binding energy of pairs consisting of an oxygen atom and a substitutional solute**

The binding energies obtained after relaxation of a supercell with a foreign atom on a bcc site and oxygen on an octahedral interstitial site are summarized in Table 3.1. Si, P, Ni, Mo, and W exhibit mainly repulsion and a few, very weak, attractive interactions. In the case of Ni, Mo, and W highest repulsion exists at the first neighbor distance, whereas for Si and P maximum repulsive interaction occurs at the second neighbor distance. Al, Cr, and Mn show the strongest attraction at the first neighbor distance while S, Ti, and Y show the highest attractive interaction with O at the second neighbor distance. On the one hand Table 3.1 demonstrates that the interaction

between O and the solutes has a relatively long range. On the other hand the trend is as expected, i.e. the interaction decreases with distances and approaches zero at the tenth neighbor distance. An exception is the O-Y interaction that is still considerable at this distance. This may be explained by the large size of the Y atom which causes significant displacements and distortions. DFT data from literature are also given in Table 3.1. These values show a very similar trend as the present results.

**Table 3.1.** Binding energy of oxygen-solute pairs at different distances. Negative (positive) values mean attraction (repulsion). DFT data from literature are given in brackets.

$E_{bind}$ (eV)	1nn	2nn	5nn	6nn	9nna	9nnb	10nn
O-Al	-0.243	0.047	-0.051	0.000	-0.04	-0.069	-0.030
O-Si	-0.064	0.453	0.051	-0.003	0.009	-0.081	0.017
O-P	0.051	0.161	0.071	-0.059	0.044	-0.024	0.040
O-S	-0.361	-0.466	-0.066	-0.134	0.051	0.062	0.013
O-Ti	-0.372 (-0.26 [43], -0.23 [44], -0.27 [46])	-0.593 (-0.55 [43], -0.45 [44], -0.55 [46])	-0.052 (0.07 [44])	-0.009 (0.14 [44])	-0.037 (0.12 [44])	0.094	-0.042
O-Cr	-0.257 (-0.25 [43], -0.1 [44])	-0.085 (0.02 [43], 0.06 [44])	0.092 (0.2 [44])	0.025 (0.13 [44])	-0.003 (0.09 [44])	0.120	0.002
O-Mn	-0.246	-0.068	0.108	0.084	0.062	0.067	0.072
O-Ni	0.214	0.175	-0.02	0.015	-0.018	0.017	-0.028
O-Y	0.031	-1.010	-0.336	-0.035	-0.085	0.217	-0.133

	(0.35 [43],0.32 [44], 0.28 [46])	(-1.01 [43],-0.73 [44], -0.85 [46])	(0.04 [44])	(0.07 [44])	(0.11 [44])		
O-Mo	0.397	-0.048	0.057	0.056	-0.036	0.158	-0.037
O-W	0.555	0.075	0.075	0.065	-0.045	0.139	-0.042

However, the numbers are somewhat different which should be mainly due to the fact that the literature data were obtained at constant volume of the supercell, whereas in the present work not only the positions of atoms but also the size and shape of the supercell were relaxed until the total stress/pressure reached zero. Furthermore, in the present work a newer version of VASP pseudopotentials (version 5.4) was used which may lead to some additional differences. Details on the volume change (compared to a supercell with perfect bcc Fe) and the distortion of the supercell by a single oxygen octahedral interstitial and by single substitutional solutes are given in Appendix I. The presence of oxygen leads to a considerable volume increase and to a tetragonal distortion. Most of the substitutional atoms cause an isotropic expansion of the supercell, whereas isotropic contraction is found for Si and P. Furthermore, Appendix I shows the effective volume change and the supercell distortion obtained for the different oxygen-solute pairs. The effective volume change, which is defined by the difference between the volume changes caused by the presence of the pair and the sum of the volume changes due to the presence of a single O atom and a single substitutional atom, can be positive or negative. Tetragonal and orthorhombic distortions of the supercell are observed which is preferentially caused by the presence of the oxygen interstitial and the spatial orientation of the O-solute pair. Tetragonal distortions are found for the 1<sup>st</sup>, 2<sup>nd</sup>, 6<sup>th</sup>, 9<sup>th</sup> neighbor distances since the relaxation occurs only in two spatial dimensions, because the initial geometrical arrangement of the pairs according to Fig. 3.1 is along [100], [110], [211], [221], and [300], respectively. On the other hand, in the case of pairs at 5<sup>th</sup> and 10<sup>th</sup> neighbor distances (oriented along [210] and [310]) orthorhombic distortions are observed due to relaxation in three dimensions.

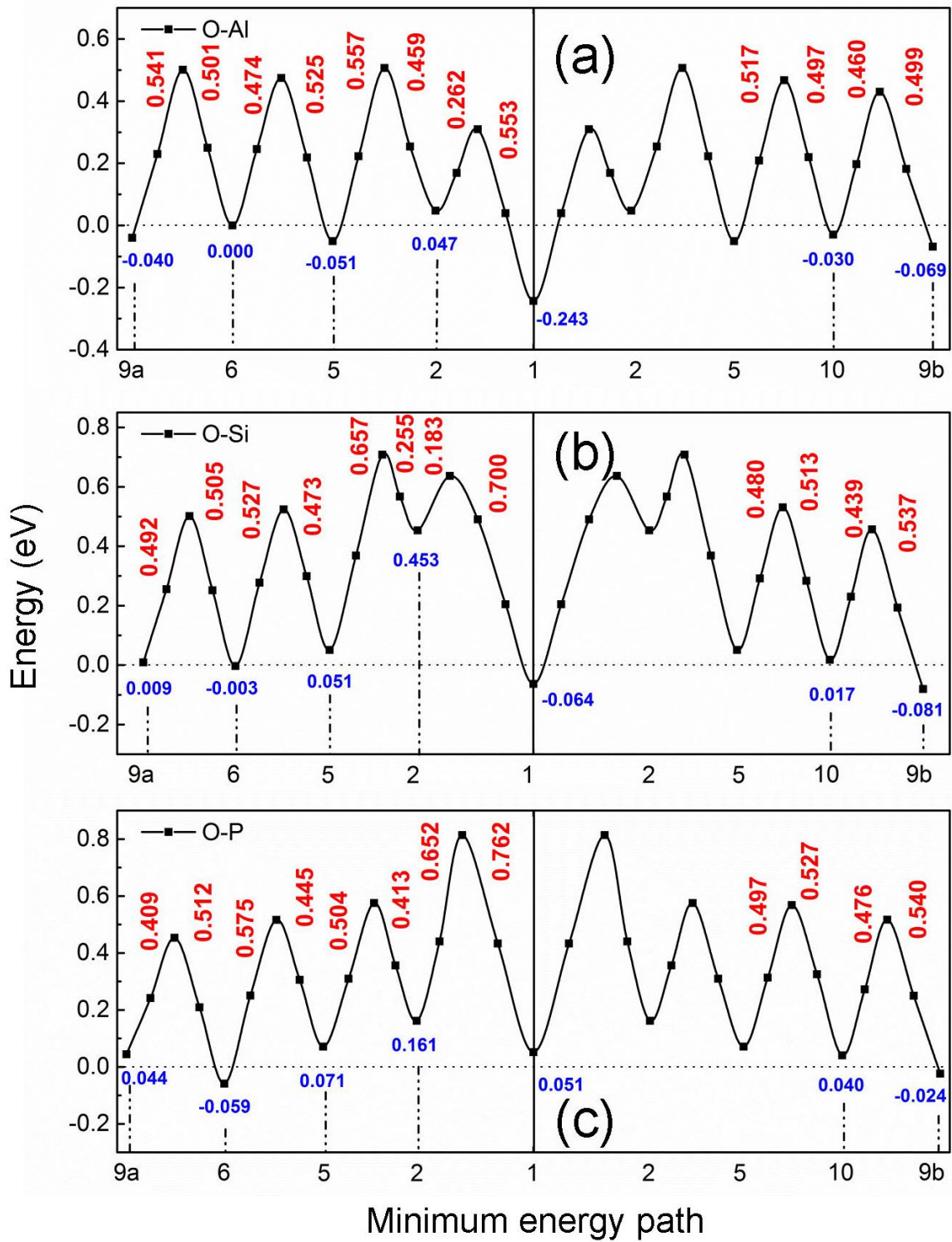
The dependence of the binding energy of the oxygen-solute pair on the kind of the solute was investigated by studying the following characteristic quantities: (i) partial density of electronic states, (ii) magnetic moment, (iii) charge transfer, (iv) volume change of the supercell, and (v) distance between the two atoms belonging to the pair. It was found that the results concerning the charge transfer determined by Bader analysis [50] seem to be most suitable for a qualitative interpretation of the trends found for the binding energy. If the pair is at the first neighbor distance in most cases attractive interaction occurs if the following two criteria are fulfilled simultaneously: Oxygen gains more than about 0.4 “electrons” and the solute loses more than about 0.6 “electrons”. This indicates an ionic-like bond. With the exception of the O-S and the

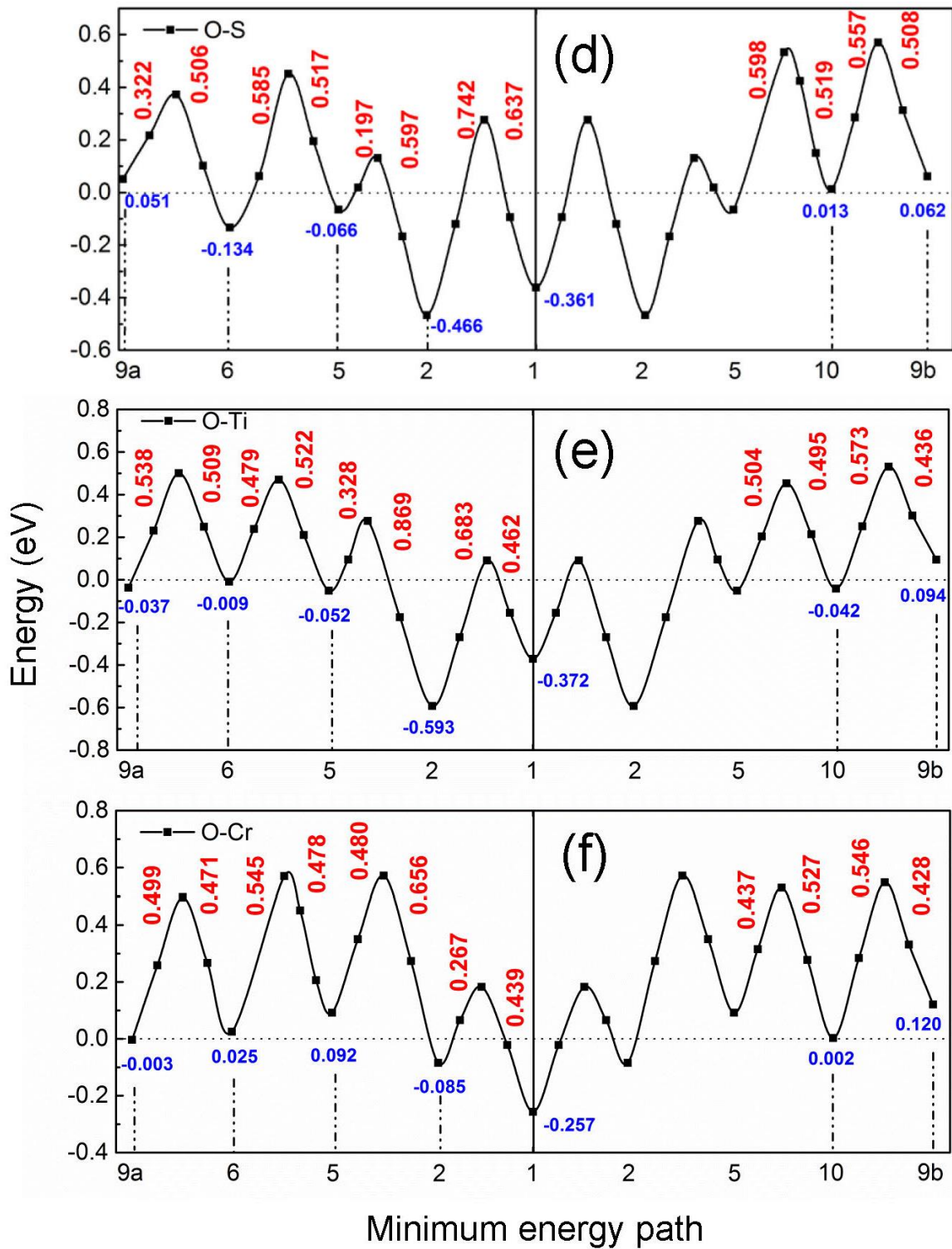
O-Y pair, in the other cases the ionic character of one of the partners is obviously not sufficiently pronounced for an attraction. More details about these investigations can be found in the Appendix II.

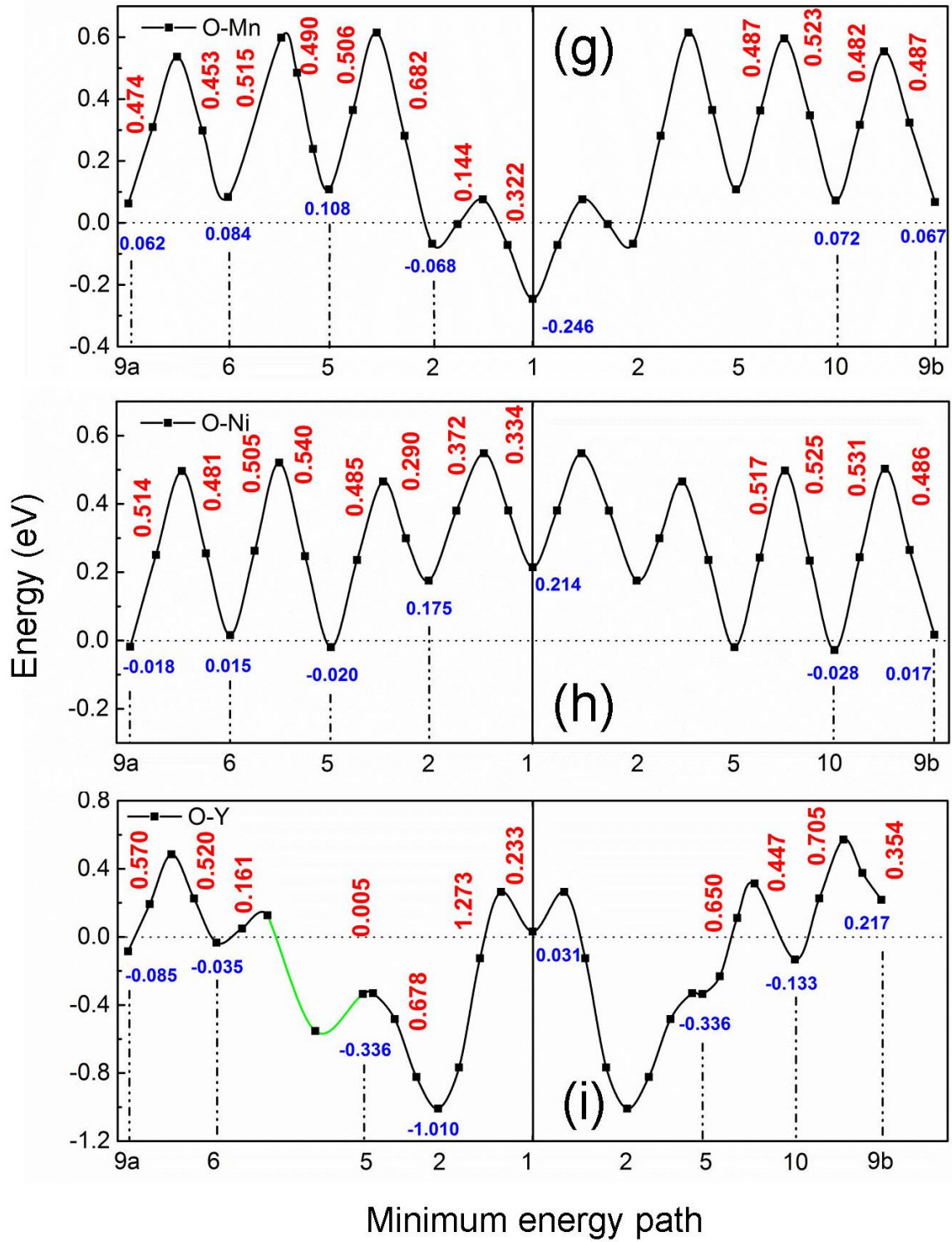
### 3.2.4 Oxygen migration barriers in the environment of a substitutional solute

Fig. 3.3 shows the minimum energy paths for the migration of oxygen between first-neighbor octahedral interstitial sites in the environment of different foreign atoms, up to the tenth neighbor. Due to the atomic configuration shown in Fig. 3.1 only the following first-neighbor jumps are possible: between neighbors 1 and 2, 2 and 5, 5 and 6, 5 and 10, 6 and 9, 9b and 10. The migration barriers are higher or lower than the value of 0.512 eV obtained for pure bcc Fe. At the largest distance from the foreign atom the migration barriers approach this value. However, some differences remain, in particular in the case of Y which should be due to its atomic size. In the figures the data points depict the calculated values that are used to determine the fit curves. In the case of Ni most of the barriers are smaller and only a few are slightly higher than that in pure Fe. P, Mo, and W exhibit this kind of barriers outside the 2<sup>nd</sup> neighbor shell whereas such barriers exist for Si outside the 5<sup>th</sup> neighbor shell. However, in these cases the barriers for jumps into the closer environment of the foreign atom are relatively high (around 0.7 eV). Al, S, Ti, Cr, Mn, and Y show rather high barriers for escape from neighbor shells close to the solute, whereas the barriers for approaching are often relatively low. In the vicinity of S and Ti the escape is impeded by the combined action of the barriers for 2→5 and for 5→6 or 5→10 jumps. A similar situation exists for Al, Mn, and Cr caused by the combination of the barriers for the 1→2 and the 2→5 jump.









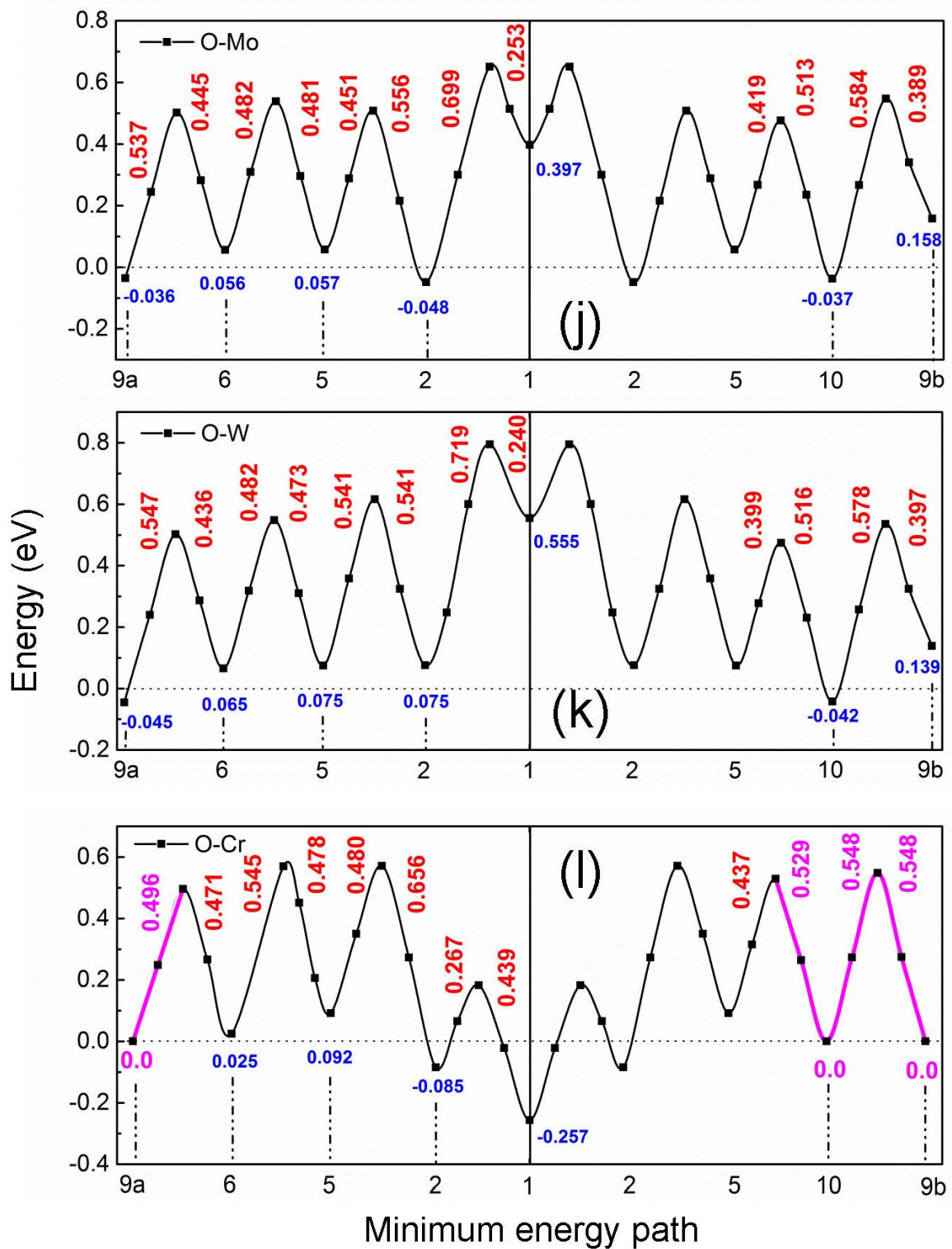


**Figure 3.3** Migration barriers for oxygen in the neighborhood of various substitutional atoms: Al (a), Si (b), P (c), S (d), Ti (e), Cr (f), Mn (g), Ni (h), Y (i), Mo (j), W (k). The red and blue numbers show the barrier height and the binding energy, respectively. In AKMC simulations the barriers must be modified according to the detailed

balance. This is illustrated in the case of Cr (I) where the changes are marked by magenta numbers and lines.

Obviously, an impeded escape is correlated with the existence of deep attractive states. A special situation is found in the environment of Y. The NEB calculation for the transition between neighbor 5 and 6 shows a local minimum related to the first image and a local maximum related to the second image [cf. part of the line in Fig. 3.3 (i) marked by green color]. Complete relaxation of the state corresponding to the local minimum led to the 2<sup>nd</sup> neighbor configuration. Thus one can conclude that a direct transition between neighbors 5 and 6 is not possible. On the other hand it can be assumed that the local maximum found between 5 and 6 is the barrier for a direct transition between neighbors 6 and 2. In the vicinity of Y the escape of the oxygen atom is strongly impeded by the combined action of the barriers for the 2→5 and 5→10 transitions. It should be noticed that calculations showed that O resides in a (meta)stable state at the 5<sup>th</sup> neighbor position, with a shallow minimum which is hardly visible in Fig. 3.3 (i). Note that there is also a very small barrier for the transition 5→2. With the exception of the peculiarities in the case of Y, in general the migration path of O is similar to that in pure bcc Fe, i.e. from a modified octahedral site via a modified tetrahedral site to another modified octahedral site. This is illustrated in Fig. 3.4 for the oxygen jump between the first and second neighbor position of Cr. In many plots shown in Fig. 3.3 the migration barrier corresponds to the middle data point in the graphical representation of the respective jump. Exceptions are the transitions between 1<sup>st</sup> and the 2<sup>nd</sup> neighbors of Si, Y, and W, between the 2<sup>nd</sup> and 5<sup>th</sup> neighbor of Y, between the 5<sup>th</sup> and 10<sup>th</sup> neighbors of S, between the 5<sup>th</sup> and 6<sup>th</sup> neighbors of Cr and Mn, and between neighbors 6 and 9a as well as 5 and 10 of Y. Also in these cases the saddle points correspond to modified tetrahedral interstitial configurations.

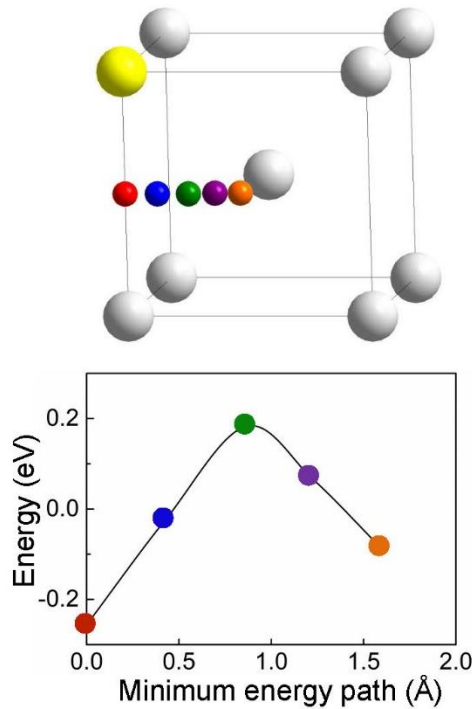


**Figure 3.4** Modified minimum energy path for the jump of oxygen between the first and the second neighbor of Cr.

### 3.3 AKMC simulations

#### 3.3.1 Simulation procedure

The general scheme of the AKMC simulations on a rigid lattice is described in section 2.3.5. Based on the results presented in previous sections it is assumed that the migration of oxygen consists of jumps between first-neighbor octahedral sites of the bcc lattice. The concentration of foreign atoms in the alloy is determined by the size of the simulation cell. Based on the DFT data for  $E_m$  and  $\nu_0$  the jump rates for the 4 possible jumps of the O atom from a given octahedral site to neighboring octahedral sites are determined. It should be noticed that the attempt frequency calculated for oxygen jumps in perfect bcc Fe is also used for those in the environment of substitutional atoms, whereas the values for  $E_m$  are different (see Fig. 3.3.) Jumps from neighbors 9a, 9b, or 10 to larger distances, from larger distances to these sites, or jumps completely outside the ten neighbor shells are described as the jumps in pure Fe. In cases where at neighbor shells 9a, 9b, and 10 the binding energy between oxygen and the substitutional solute does not vanish, it is set to zero and the migration energy barriers  $E_m^{9a,6}$ ,  $E_m^{10,5}$ ,  $E_m^{9b,10}$  and  $E_m^{10,9b}$  are modified according to

$$E_m^{i,j} - E_m^{j,i} = E_{bind}^j - E_{bind}^i, \quad (3.1)$$

This relation describes the rule of detailed balance which must be fulfilled in AKMC simulations, cf. [51]. Note that Eq. (3.1) is always satisfied for transitions inside the tenth neighbor shell. For illustration the modifications of  $E_m^{9a,6}$ ,  $E_m^{10,5}$ ,  $E_m^{9b,10}$  and  $E_m^{10,9b}$  in the environment of Cr are shown in Fig. 3.3(l). As mentioned in section 2.3.5, the oxygen diffusion coefficient is obtained from

$$D = \frac{1}{n_s} \sum_{m=1}^{n_s} \frac{sd(m)}{6 \delta t}. \quad (3.2)$$

where  $sd(m) = (\bar{x}(t_m) - \bar{x}(t_{m-1}))^2$  is the squared displacement of a part of the migration trajectory characterized by the time segment  $\delta t$ , with  $t_m = t_{m-1} + \delta t$ , and  $n_s$  is the total number of time segments. In the present AKMC simulations the maximum and minimum values of  $n_s$  (see section 2.3.5) are 7500 and 10, respectively. Too small (high) values of  $\delta t$  ( $n_s$ ) lead to values of  $D$  which are not reliable, because correlations are not included sufficiently, and too high (small) values of  $\delta t$  ( $n_s$ ) lead to large fluctuations of  $D$  which is due to poor statistics. Therefore, those values of  $D$  are not considered in the final averaging over the results for different subdivisions into time segments. In the present code the averaging is performed only over subdivisions between  $n_s^{\max} / 3$  and  $2n_s^{\max} / 3$ .

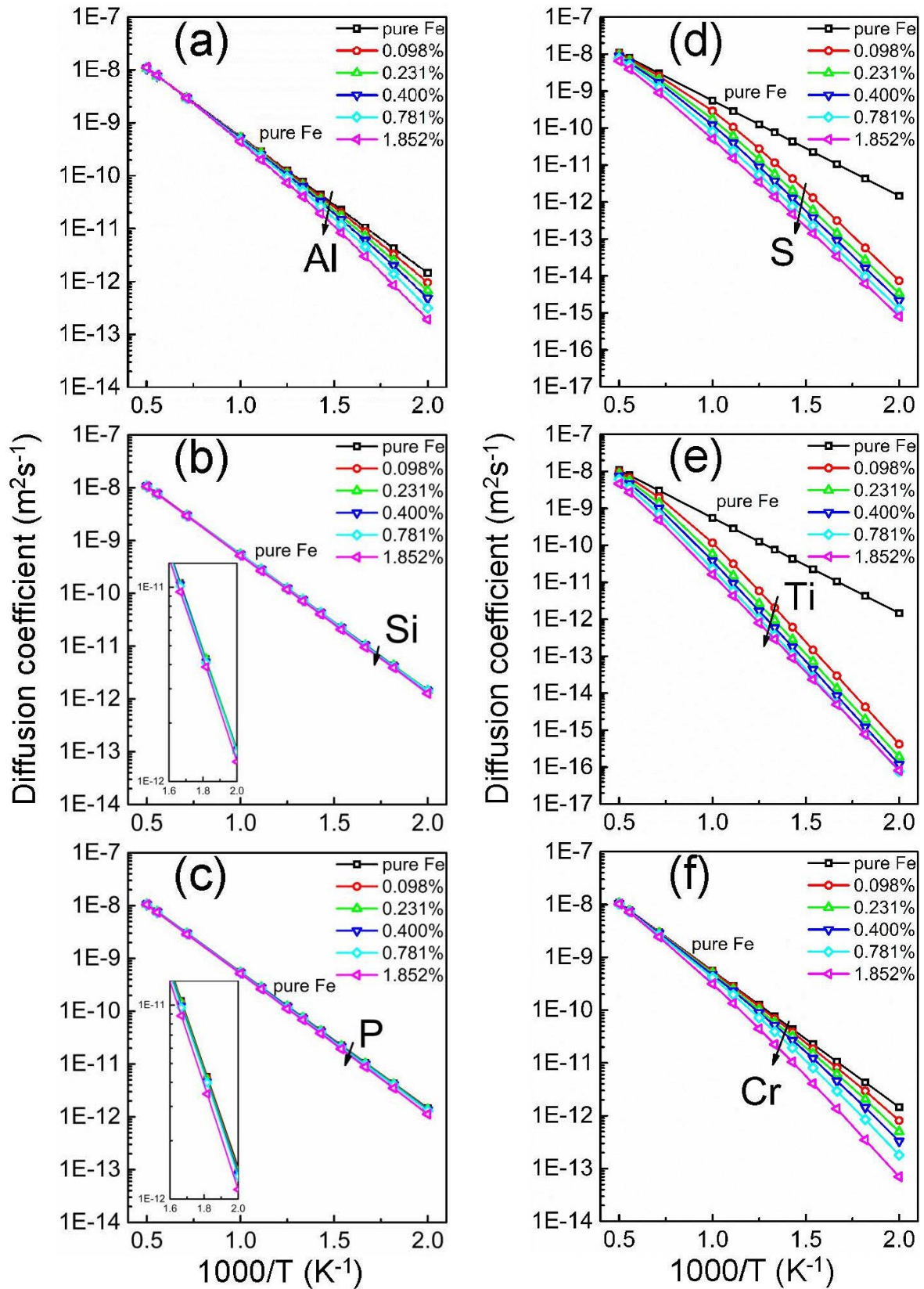
### 3.3.2 Diffusion coefficients of oxygen

AKMC simulations were performed to study oxygen diffusion in alloys with concentrations of substitutional solutes of 0.098, 0.231, 0.400, 0.781, and 1.852 at%. As already mentioned above, an AKMC simulation cell contains only one substitutional foreign atom, therefore the size of the cell ( $8 \times 8 \times 8$ ,  $6 \times 6 \times 6$ ,  $5 \times 5 \times 5$ ,  $4 \times 4 \times 4$ , and  $3 \times 3 \times 3$  bcc unit cells, respectively) is related to the solute concentration. With the exception of the case of highest concentration (1.852 %) dilute alloys are considered. In dilute alloys the migration of the O atom cannot be influenced at the same time, or “simultaneously”, by more than one substitutional solute or its periodic image. After leaving the region of influence of a certain solute atom, in a dilute alloy the diffusing O atom migrates (long enough) through perfect bcc Fe before it enters another region of influence. The region of influence ends at the 10<sup>th</sup> neighbor shell, cf. Fig. 3.3 and the

discussion related to the detailed balance in the previous section. The concentration of 1.852 % is already beyond that of a dilute alloy, details on this case are discussed below. Fig. 3.5 shows the dependence of the diffusion coefficient on temperature in the range between 500 and 2000 K. It has to be taken into account that the presented data are strictly valid only in the ferromagnetic phase, i.e. below the Curie temperature (1043 K). Furthermore, at about 1183 K the  $\alpha$  (bcc) to  $\gamma$  (fcc) transition of iron occurs. The main reason for showing a temperature scale up to 2000 K is to verify the expected convergence of the diffusion coefficient to the value for pure bcc Fe at sufficiently high temperatures. It must be also mentioned that in the present work the temperature dependence of the spontaneous magnetization in the ferromagnetic state is neglected, i.e. it is always assumed that the magnetization of bulk iron corresponds to its ground state value. According to the influence on the diffusion of oxygen the foreign atoms can be categorized into three groups which is similar to the classification discussed concerning the migration barriers. The first group consists of Si, P, Ni, Mo, and W. These solutes have a very small effect on the diffusion coefficient. The reason for this behavior is due to the size and combination of the migration barriers as depicted in Figs. 3.3 (b-c), (h), (j), and (k). The majority of barriers in the vicinity of Ni is somewhat lower than the barrier in pure Fe. Therefore, the diffusion coefficient increases slightly with concentration [cf. inset in Fig. 3.5 (h)]. In the case of P, Mo, and W the barriers for oxygen jumps from the 2<sup>nd</sup> to the 1<sup>st</sup> neighbor are rather high while the other barriers are not very different from that in pure iron. Similar conditions exist in the environment of Si with a high barrier between the 5<sup>th</sup> and the 2<sup>nd</sup> neighbor. Such a combination of migration barriers, with a reduced accessibility of positions close to the solute, may cause the so-called labyrinth mechanism [13,14], which leads to a slight reduction of the diffusion coefficient with increasing solute concentration [cf. insets in Figs. 3.5 (b-c), and (j)]. The second group of solutes with Al, Cr, and Mn exhibit a considerable reduction of oxygen mobility. Taking Cr as an example, 0.098 (1.852) % Cr decrease the diffusion coefficient of by 44.3% (95.2%) at 500K and by 2.6% (43.4%) at 1000K, compared to the values for pure Fe. The reasons for this behavior is the so-called trapping mechanism [13,14] caused by the existence of a pronounced attractive state at the 1<sup>st</sup> neighbor distance and by high escape barriers from this state [cf. Figs. 3.3 (a), (f), and (g)]. Such a trapping mechanism is also responsible for the huge decrease of the diffusion coefficient observed in the case of the third group with S, Ti, and Y. For example, the oxygen diffusivity decreases by 99.97% (99.99%) at 500K and by 78.9%



(97.05%) at 1000K if the alloy contains 0.098% (1.852%) Ti. The foreign atoms S, Ti, and Y exhibit deep attractive state at the 2<sup>nd</sup> neighbor distance and the barriers for escape from these positions are very high [cf. Figs. 3.3 (d-e) and (i)]. However, in all cases considered in this work the oxygen diffusion coefficient is still some orders of magnitude higher than that of the corresponding foreign atom (cf. [1,52,53]). Therefore, the assumption that the substitutional solute can be considered to be immobile in the AKMC simulations is justified.



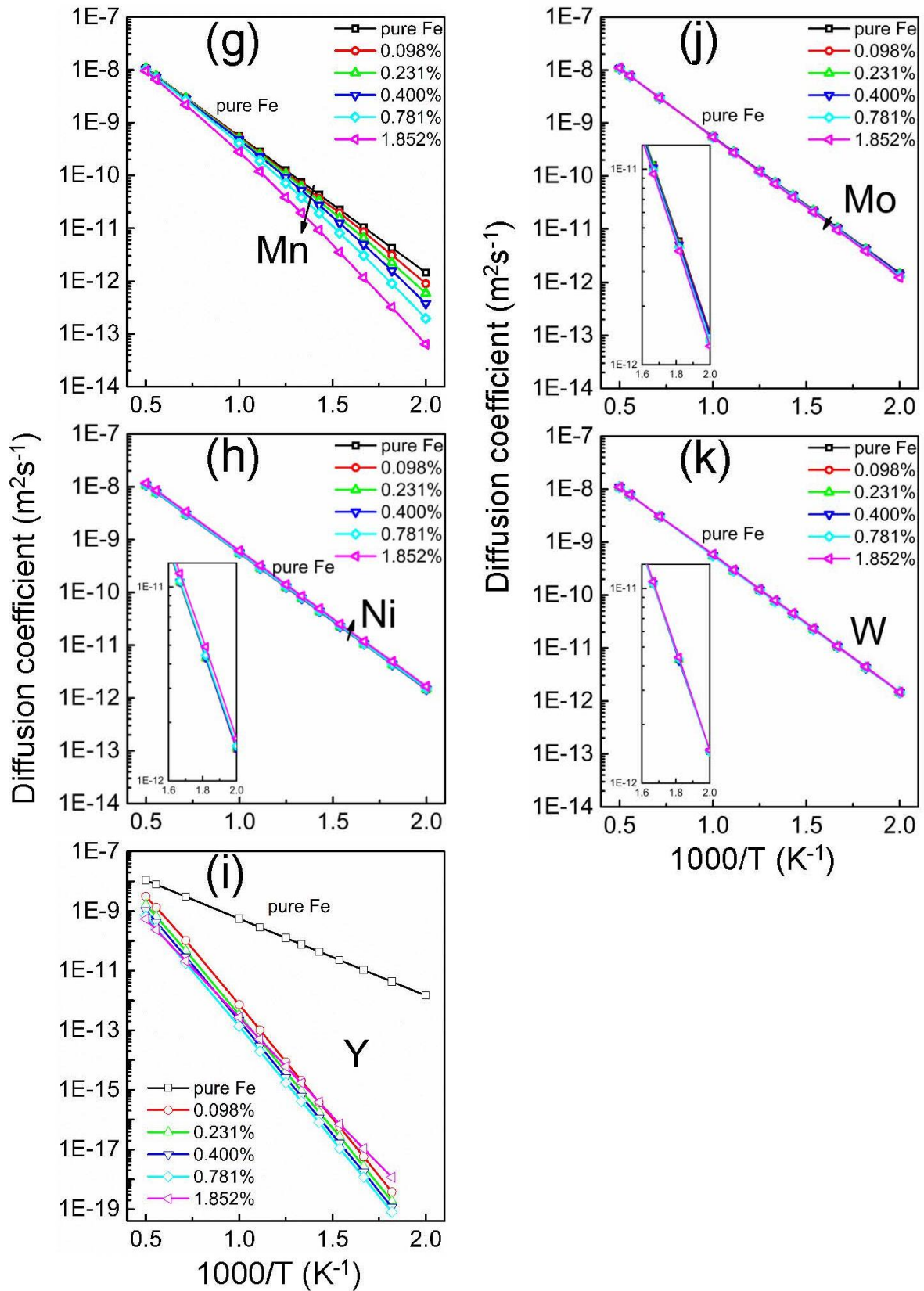


**Figure 3.5** Diffusion coefficient of oxygen in several dilute Fe alloys in dependence on temperature and solute concentration (in at %).

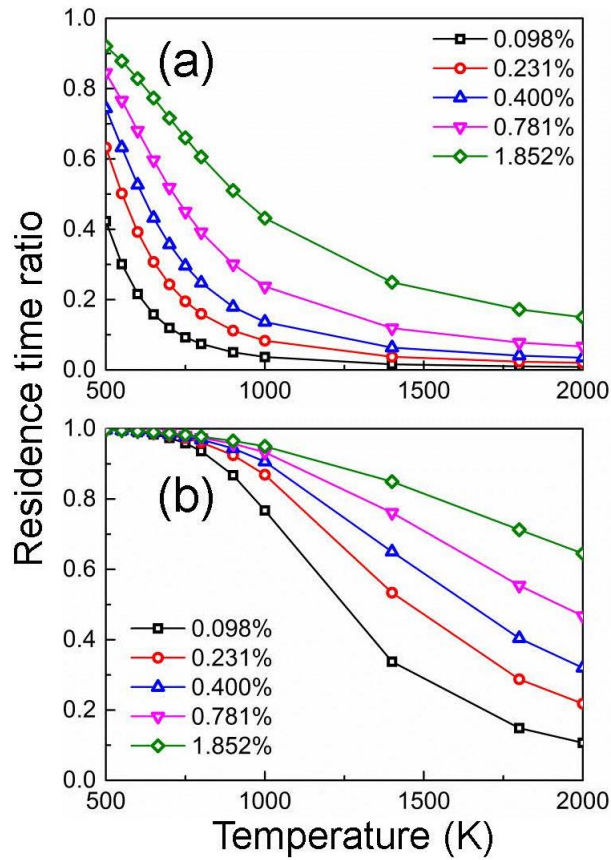


**Figure 3.6** Residence time ratio for oxygen at the first neighbor site of Cr (a) and at the second neighbor site of Ti (b).

It is not surprising that the influence of foreign atoms on the oxygen mobility leads to deviations from the Arrhenius behavior of the diffusion coefficient. This is clearly visible for solutes of the second and third group. The reason is the inhomogeneous distribution of the barriers heights: Specific barriers exist in the vicinity of the substitutional atom, while beyond the 10<sup>th</sup> neighbor shell the migration barriers are equal to that in pure bcc Fe. The pronounced difference between all these barriers leads to a temperature dependence of the ratio between residence times in the various states. For a detailed study the ratio between the residence or occupation time of the oxygen atom at different neighbor distances and the total time of the simulation was determined. Fig. 3.6 illustrates the residence time ratio for oxygen at the first neighbor site of Cr and the second neighbor site of Ti. Both sites are related to the highest absolute values of binding energy (cf. Table 3.1). A strong variation with temperature and concentration is visible in Fig. 3.6. In the case of Cr the occupation time ratio continuously increases with concentration both at low and high temperature while it

decreases with increasing temperature. The latter is due to the fact that with increasing temperature the ratio of the residence time in the deepest state to that in other states decreases because of the higher mobility of the diffusing atom. The reduction of the diffusion coefficient with concentration and the concave shape of the curves in Figs. 3.5 (f) are related to the behavior of the occupation time ratio as shown in Fig. 3.6 (a). The dependencies of the diffusion coefficient due to presence of Al and Mn can be explained similarly to the case of Cr. The occupation time ratio for Ti [Fig. 3.6 (b)] strongly differs to that of Cr. While this quantity also decreases with temperature, with increasing concentration a pronounced trend towards saturation is found at low temperature. This is the reason for the saturation of the reduction of the diffusion coefficient with increasing concentration observed at these temperatures [Fig. 3.5 (e)]. At low temperature the residence time of oxygen at the 2<sup>nd</sup> neighbor site of Ti is much larger than at all other sites, even at the rather low concentration of 0.098%. The explanation of the influence of S and Y on the mobility of oxygen in terms of the residence time ratio is similar to the above discussion for Ti.

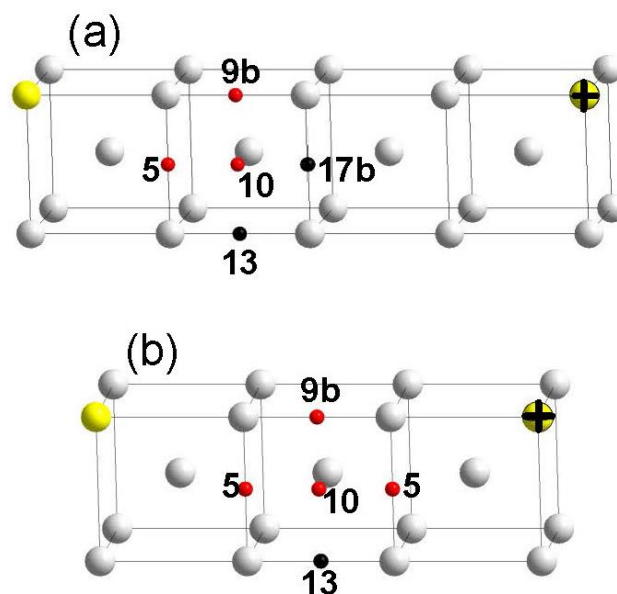


**Figure 3.7** Different environments of the 10<sup>th</sup> neighbour octahedral site in a simulation cell consisting of  $4 \times 4 \times 4$  (a) and  $3 \times 3 \times 3$  (b) bcc unit cells. The figure illustrates the extensions of the simulation cell in one direction. In larger simulation cells the situation is similar to (a).

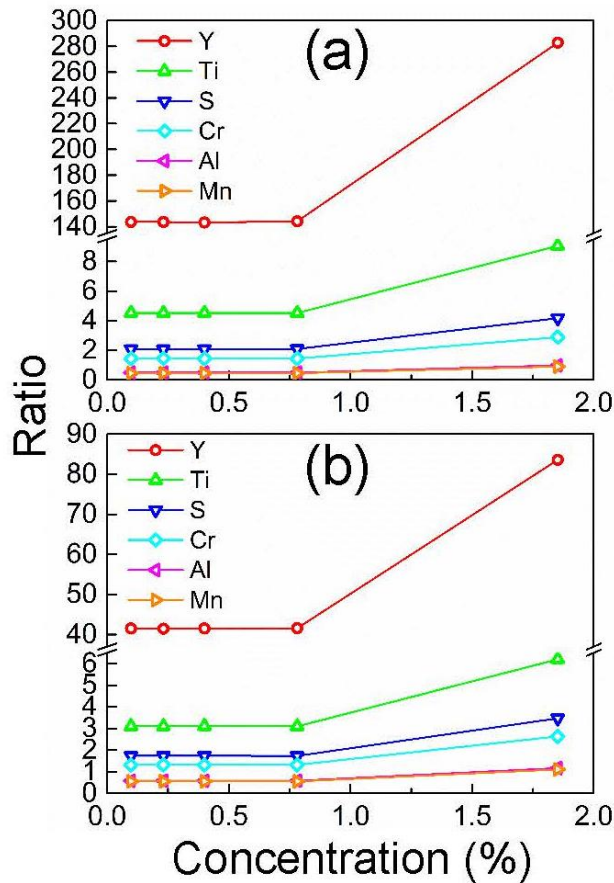


**Figure 3.8** Ratio of the number of oxygen jumps from 10 to 5 to the number of jumps between 10 and 9b as function of the solute concentration at 600K (a) and 800K (b)

As already mentioned above, the case of the highest concentration (1.852 %, one solute in a simulation cell consisting of  $3 \times 3 \times 3$  bcc unit cells) does not correspond to a dilute alloy since there may be a kind of "simultaneous interaction" of the diffusing oxygen atom with the solute and its periodic image. This is illustrated in Fig. 3.7 by comparison with the situation in a AKMC cell containing  $4 \times 4 \times 4$  bcc unit cells. Due to periodic boundary conditions the environment of the 10<sup>th</sup> neighbor site is not equal. In the  $4 \times 4 \times 4$  cell as well as in larger cells this site has one neighbor with a 5<sup>th</sup> neighbor distance to the solute, one neighbor with a 9<sup>th</sup> neighbor distance (9b) and two neighbors with a distance to the foreign atom larger than the 10<sup>th</sup> neighbor distance (denoted by 13, 17b). In the smaller cell the considered site has only one neighbor with a distance to the solute larger than the 10<sup>th</sup> neighbor distance (13) and one neighbor with a 9<sup>th</sup> neighbor distance (9b), but two neighbors with a 5<sup>th</sup> neighbor distance. This leads to a modification of the ratios between the jumps from and to the 10<sup>th</sup> neighbor site while the ratios for the other sites within the 10<sup>th</sup> neighbor shell remain unchanged.

The ratio of the number of jumps between 10 and 5 to the number of jumps between 10 and 9b is depicted in Fig. 3.8, for the solutes of group 2 and 3 and at a temperature of 600 and 800 K. For concentrations up to 0.781% this ratio has a constant value which is determined by the given relation between the corresponding jump barriers. However, due to the situation discussed above, at the concentration of 1.852% the ratio becomes equal to two times the value obtained for the lower concentrations. At this concentration the highest ratios is found for Y and Ti. This leads to the intersection of the curves for the diffusion coefficient in Figs. 3.5 (e) and (i). Such an intersection is not observed for the other solutes considered in Fig. 3.8. Obviously, the ratio of jump numbers at 1.852% is too low in these cases. Note that in Fig. 3.8 the data points are relevant whereas the lines are only shown to guide the eye. The above discussion illustrates a rather artificial example of a non-dilute alloy and shows that in this case a pronounced non-monotonous dependence of the diffusion coefficient on concentration is possible. The general case of a non-dilute alloy is not subject of this work. Here a huge number of additional barriers would have to be determined. These barriers concern all cases of possible “simultaneous interactions” of the oxygen atom with more than one substitutional solute.

### **3.4 Summary and conclusions**

The effect of substitutional foreign atoms on oxygen diffusion in bcc Fe was investigated by a combination of DFT calculations and AKMC simulations. At first DFT was used to investigate three different migration paths of oxygen in pure bcc Fe, i.e. between first-neighbor, second-neighbor, and third-neighbor octahedral interstitial sites. Most relevant is the first-neighbor jump with a linear migration path and the tetrahedral interstitial site as the saddle point. The second-neighbor jump consists of two successive first-neighbor jumps. The third-neighbor jump has a nonlinear migration path and the saddle point corresponds to a rhombohedral interstitial site, but the barrier for such a direct jump is too high to be relevant for O diffusion. In the presence of a substitutional solute the migration path is rather similar to that in pure bcc Fe, i.e. from a modified octahedral site via a modified tetrahedral site to another modified octahedral site as the first-neighbor jump. The interaction of oxygen with Si, P, Ni, Mo, and W is primarily repulsive. The corresponding migration barriers are not very different from that in pure Fe, with the exception of a high barrier close to the substitutional atom. Al, S, Ti, Cr, Mn, and Y exhibit strong attractive interactions with oxygen, associated with

large barriers for escape from neighbor shells close to the solute. The barriers for approaching the substitutional atom are frequently relatively low. In the vicinity of S and Ti the escape is impeded by the combined action of the barriers for  $2 \rightarrow 5$  and for  $5 \rightarrow 6$  or  $5 \rightarrow 10$  jumps, while for Al, Mn, and Cr the combination of the barriers for the  $1 \rightarrow 2$  and the  $2 \rightarrow 5$  jump impedes the escape. Some peculiarities were found in the case of Y: A direct transition between neighbors 5 and 6 is not possible and a direct second-neighbor jump between 6 and 2 was considered. In the vicinity of Y the escape of the oxygen atom is strongly impeded by the combined action of the barriers for the  $2 \rightarrow 5$  and  $5 \rightarrow 10$  transitions.

AKMC simulation were applied to study O diffusion in dilute alloys with concentrations of foreign atoms up to 0.781 at %. Si, P, Ni, Mo, and W have a very small effect on the oxygen diffusion coefficient. Al, Cr, and Mn cause a considerable reduction of oxygen mobility. The reason for this behavior is the so-called trapping mechanism due to the attractive interaction between the substitutional solute and O. Such a mechanism is also responsible for the huge decrease of the diffusion coefficient observed in the case of S, Ti, and Y. In all cases investigated the oxygen diffusion coefficient was still some orders of magnitude higher than that of the corresponding foreign atom. Therefore, the assumption that the substitutional solute can be considered to be immobile throughout the AKMC simulations is justified. The influence of Al, Cr, Mn, S, Ti, and Y leads to deviations from the Arrhenius behavior of the oxygen diffusion coefficient. This is due to the significant temperature dependence of the ratio between residence times in the respective states. At the concentration of 1.852 % a “simultaneous interaction” of the diffusing oxygen atom with the solute and its periodic image may occur. In this rather artificial example of a non-dilute alloy a non-monotonous dependence of the diffusion coefficient on concentration may be observed.

The results of present investigations show a strong dependence of the oxygen diffusion coefficient on the kind of the substitutional atom. This changes the picture of oxygen diffusion in dilute ferritic iron alloys importantly. Future experimental work is required to study these dependencies in detail and to consider other trapping mechanisms which might compete with those considered in the present paper. In this context theoretical studies on the modification of oxygen diffusion by other traps than substitutional solutes may be useful.



## Chapter 4 Efficient calculation method for the diffusion coefficient of interstitial solutes in dilute alloys

### 4.1 Introduction

In Chapter 3 separate AKMC simulations for different sizes of the simulation cell were performed in order to determine the dependence of the oxygen diffusion coefficient on the concentration of substitutional atoms. In this chapter an efficient method is presented which allows for the calculation of the diffusion coefficient for different concentrations based on results of AKMC simulations for only one size of the simulation cell. This leads to a tremendous decrease of computational efforts.

### 4.2 Calculation method

The calculation of the diffusion coefficient can be separated into a contribution related to the migration in the region of interaction between oxygen and the substitutional solute and a part related to diffusion in pure bcc Fe. At given temperature and concentration of substitutional atoms the diffusion coefficient of oxygen (or of another interstitial solute) can be written as

$$D = \frac{t_{\text{free}}}{t_{\text{total}}} D_{\text{free}} + \frac{t_{\text{inter}}}{t_{\text{total}}} D_{\text{inter}} \quad (4.1a)$$

with

$$t_{\text{total}} = t_{\text{free}} + t_{\text{inter}} \quad (4.1b)$$

where  $D_{\text{free}}$  is the diffusion coefficient of oxygen in pure bcc Fe, i.e. outside the region of influence by the substitutional solute, and  $D_{\text{inter}}$  is the diffusion coefficient of oxygen inside the interaction region. The quantities  $t_{\text{free}}$  and  $t_{\text{inter}}$  correspond to the sum of the time periods for diffusion outside or inside the region of influence, respectively, and  $t_{\text{total}}$  is the total diffusion time. The value of  $D_{\text{free}}$  is given by the known analytical formula (see section 2.3.4)

$$D_{\text{free}} = \frac{a^2}{6} v_0^{\text{free}} \exp\left(\frac{-E_m^{\text{free}}}{k_B T}\right) \quad (4.2)$$

with the lattice constant  $a$ , as well as the migration barrier  $E_m^{free}$  and the attempt frequency  $\nu_0^{free}$  in pure bcc Fe, i.e.  $a = 2.832 \text{ \AA}$ ,  $E_m^{free} = 0.512 \text{ eV}$ , and  $\nu_0^{free} = 15.76 \text{ THz}$  (see section 3.2.2) The values of  $t_{free}$ ,  $t_{inter}$ , and  $t_{total}$  may be obtained from AKMC simulations as performed for the different solute concentrations or cell sizes in Chapter 3. However, the time ratios in Eq. (4.1a) can be also expressed by analytical relations containing terms with probabilities for a certain interaction of oxygen with the substitutional solute.

$$\frac{t_{inter}}{t_{total}} = \frac{\sum_i N_i \exp\left(-\frac{E_{bind}^i}{k_B T}\right) c_S}{1 - \sum_i N_i c_S + \sum_i N_i \exp\left(-\frac{E_{bind}^i}{k_B T}\right) c_S} \quad i = 1, 2, 5, 6, 9a, 9b, 10 \quad (4.3a)$$

$$\frac{t_{free}}{t_{total}} = \frac{1 - \sum_i N_i c_S}{1 - \sum_i N_i c_S + \sum_i N_i \exp\left(-\frac{E_{bind}^i}{k_B T}\right) c_S} \quad (4.3b)$$

$$(N_1 = 2, N_2 = 4, N_5 = 8, N_6 = 8, N_{9a} = 8, N_{9b} = 2, N_{10} = 8)$$

These relations are based on the Gibbs distributions of the probability to find the system with the oxygen atom and the substitutional solute in any particular state (see Ref. [54]). The quantity  $E_{bind}^i$  denotes the binding energy of the pair at the  $i$ th neighbor distance,  $c_S$  is the concentration of the substitutional solute, and  $N_i$  is the possible number of substitutional solute sites in the  $i$ th neighborhood of oxygen. In the case of a dilute alloy (see Chapter 3) it can be assumed that  $D_{inter}$  is nearly independent of the concentration of the substitutional solute (or the size of the AKMC simulation cell), since  $D_{inter}$  is only determined by migration paths inside the region of influence by the substitutional solute. In this case AKMC simulation need to be used only once, i.e. for a certain concentration of the substitutional foreign atom, and the total diffusion coefficient  $D$  can be then determined for the other concentrations using Eqs. (4.1-4.3). It is quite clear that such a method is much more efficient than performing separate AKMC simulations for different concentrations or cell sizes as done in Chapter 3.

The calculation method outlined above is applied to O diffusion under the influence of Ti, Cr, and Si substitutional atoms. The DFT data for binding energies and migration barriers determined in Chapter 3 are used. For better comparison the three characteristic examples are depicted once more in Fig. 4.1 (see also Fig. 3.3): (i) In the environment of Ti strong attractive states exist for oxygen at the 1<sup>st</sup> and 2<sup>nd</sup> neighbor distance and in this region the barriers are relatively high compared to that in perfect bcc Fe (0.512 eV). (ii) In the corresponding interaction region of Cr the attraction is weaker and the barriers are somewhat lower. (iii) Very weak attraction and repulsion dominates in the region near a Si atom and the migration barriers are rather different. According to the rule of detailed balance (see section 3.3.1) some barriers are modified since the binding energy at the neighbors 9a, 10, and at sites outside the 10<sup>th</sup> neighbor shell are set zero. Furthermore, the binding energy at neighbor 9b was also set to zero and the detailed balance was applied to change the respective barrier.

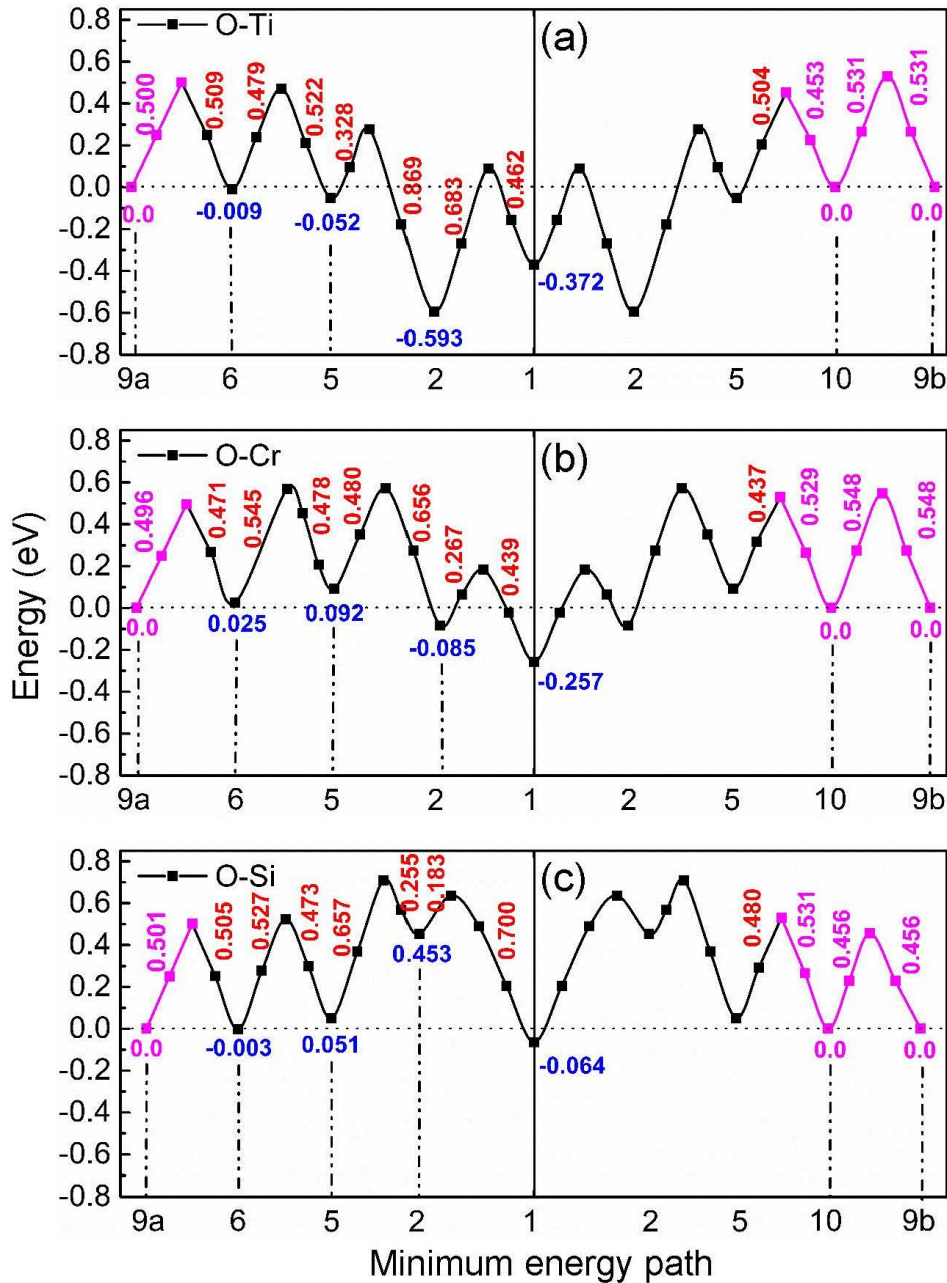


**Figure 4.1** Migration barriers for oxygen in the environment of Ti (a), Cr (b), and Si (c). The red and blue numbers show the barrier height and the binding energy, respectively. The magenta lines and numbers show modifications of the original DFT data according to the rule of detailed balance (see text).

### 4.3 Results and discussion

#### 4.3.1 The value of $D_{inter}$

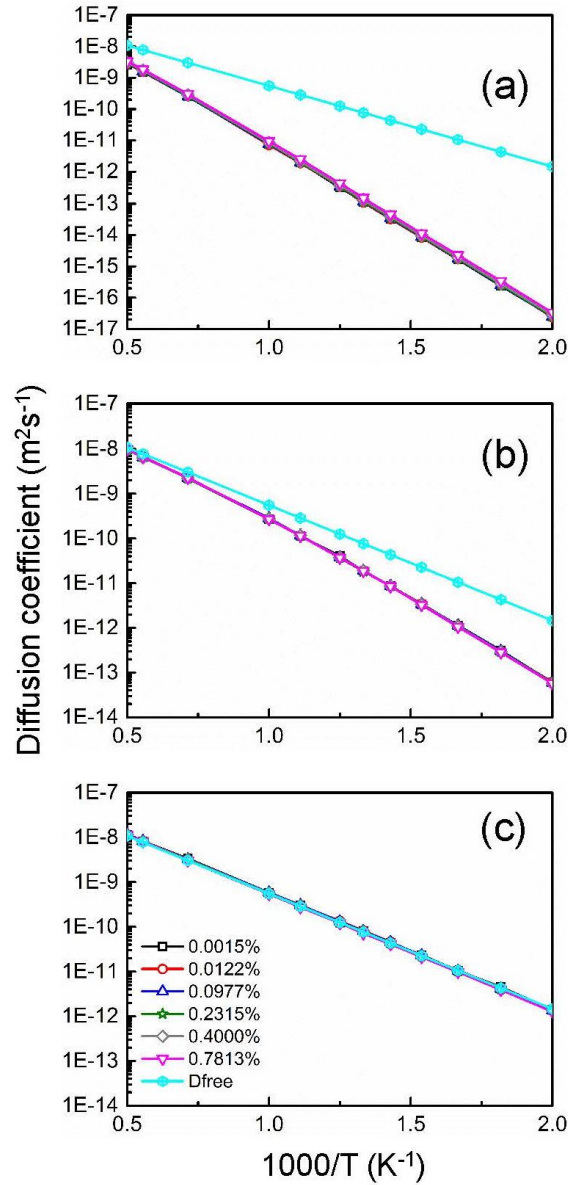


**Figure 4.2.** Diffusion coefficients of oxygen inside ( $D_{\text{inter}}$ ) and outside ( $D_{\text{free}}$ ) the interaction region with Ti (a), Cr (b), and Si (c), for different concentrations  $c_S$  (in at%) of these substitutional solutes. Note that the data for  $D_{\text{inter}}$  for different  $c_S$  are nearly equal.

Fig. 4.2 depicts data of  $D_{\text{inter}}$  determined by AKMC simulations for different cell sizes (concentrations of the substitutional foreign atoms): 32x32x32 bcc unit cells (0.0015%), 16x16x16 unit cells (0.0122%), 8x8x8 unit cells (0.0977%), 6x6x6 unit cells (0.2315%), 5x5x5 unit cells (0.4000%), and 4x4x4 unit cells (0.7813%), together with the oxygen diffusion coefficient  $D_{\text{free}}$  in pure bcc Fe. Ti, Cr, and Si substitutional solutes were considered and their influence on the diffusing oxygen is taken into account up to the

10<sup>th</sup> neighbor shell, see Fig. 4.1. The value of  $D_{\text{inter}}$  is indeed nearly independent of concentration as assumed in section 4.2. The more attractive the interaction of oxygen with a substitutional solute is, the larger is the difference between  $D_{\text{inter}}$  and  $D_{\text{free}}$ , i.e. the lower is the value of  $D_{\text{inter}}$ . The Arrhenius plots show almost straight lines for  $D_{\text{inter}}$  since this quantity is related to migration paths where the diffusing oxygen atom passes repeatedly the interaction region. However, the motion of oxygen on these paths does not correspond to a migration in a lattice with an exactly periodic sequence of barriers. Therefore, slight deviations from a straight line in the Arrhenius plot are found [see Fig. 4.2 (b)].

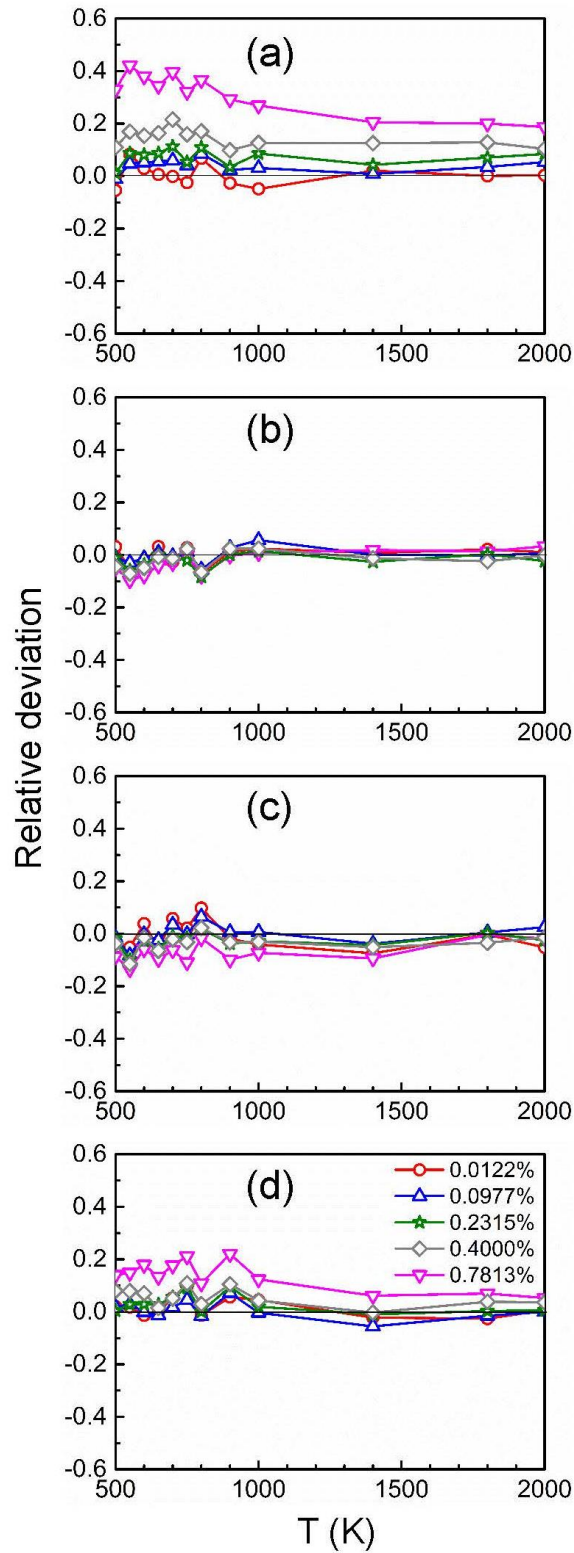


**Figure 4.3** Relative deviation  $[D_{\text{inter}}(c_S) - D_{\text{inter}}(c_S^0)] / D_{\text{inter}}(c_S^0)$  for different values of  $c_S$  in the case of Ti (a), Cr (b), and Si (c) in dependence on temperature ( $c_S^0 = 0.0015\%$ ). If the interaction region between oxygen and Ti is reduced to the 5<sup>th</sup> neighbour shell the deviations become smaller (d).

Figs. 4.3 (a-c) show the relative deviation of  $D_{\text{inter}}$  at concentrations  $c_S$  of 0.0122%, 0.0977%, 0.2315%, 0.4000%, and 0.7813% from that at  $c_S^0=0.0015\%$ , i.e. the quantity  $[D_{\text{inter}}(c_S) - D_{\text{inter}}(c_S^0)] / D_{\text{inter}}(c_S^0)$ . In general the relative deviations are small which is in accord with the finding from Fig. 4.2 where a logarithmic scale was used on the ordinate. However, the difference found for the two highest concentrations (0.7813 and 0.4000 %) of the substitutional solute Ti cannot be explained by statistical fluctuations of the AKMC results. Obviously, in these cases the size of the AKMC simulation cell is too small to achieve a sufficient “randomization” of the trajectories of the migrating oxygen between successive passes through interaction regions. In other words, the entrance and exit points for migration to and from different interaction regions (or for migration in pure Fe) are slightly correlated which is not the case for low concentration. Here the term “different interaction regions” is related to successive passing of an interaction region with a sufficiently long migration in pure Fe in between. The above mentioned correlation leads to apparently longer diffusion paths in the interaction region since entrance point at the subsequent interaction region is preferentially on the side facing to the exit point from the preceding interaction region. This issue was considered in more detail by performing AKMC simulations for a case where the interaction region of oxygen with the substitutional foreign atom is reduced to the 5<sup>th</sup> neighbor shell. For this purpose, outside the 5<sup>th</sup> neighbor shell the binding energies were set to zero and the corresponding barriers were set equal to that in pure bcc Fe as well as the rule of detailed balance was applied in the transition region. Fig. 4.3 (d) clearly shows that for 0.4000 and 0.7813% Ti the relative deviation is smaller than in Fig. 4.3 (a). Obviously, there is more space now for the “randomization” of the trajectories in pure Fe. The results presented in Fig. 4.3 show that in cases of strong attraction between O and the substitutional solute a minor dependence of  $D_{\text{inter}}$  on concentration occurs at higher concentration values, whereas this is not observed for weak attraction or repulsion. This minor dependence is stronger at low temperature.



### 4.3.2 Time ratios

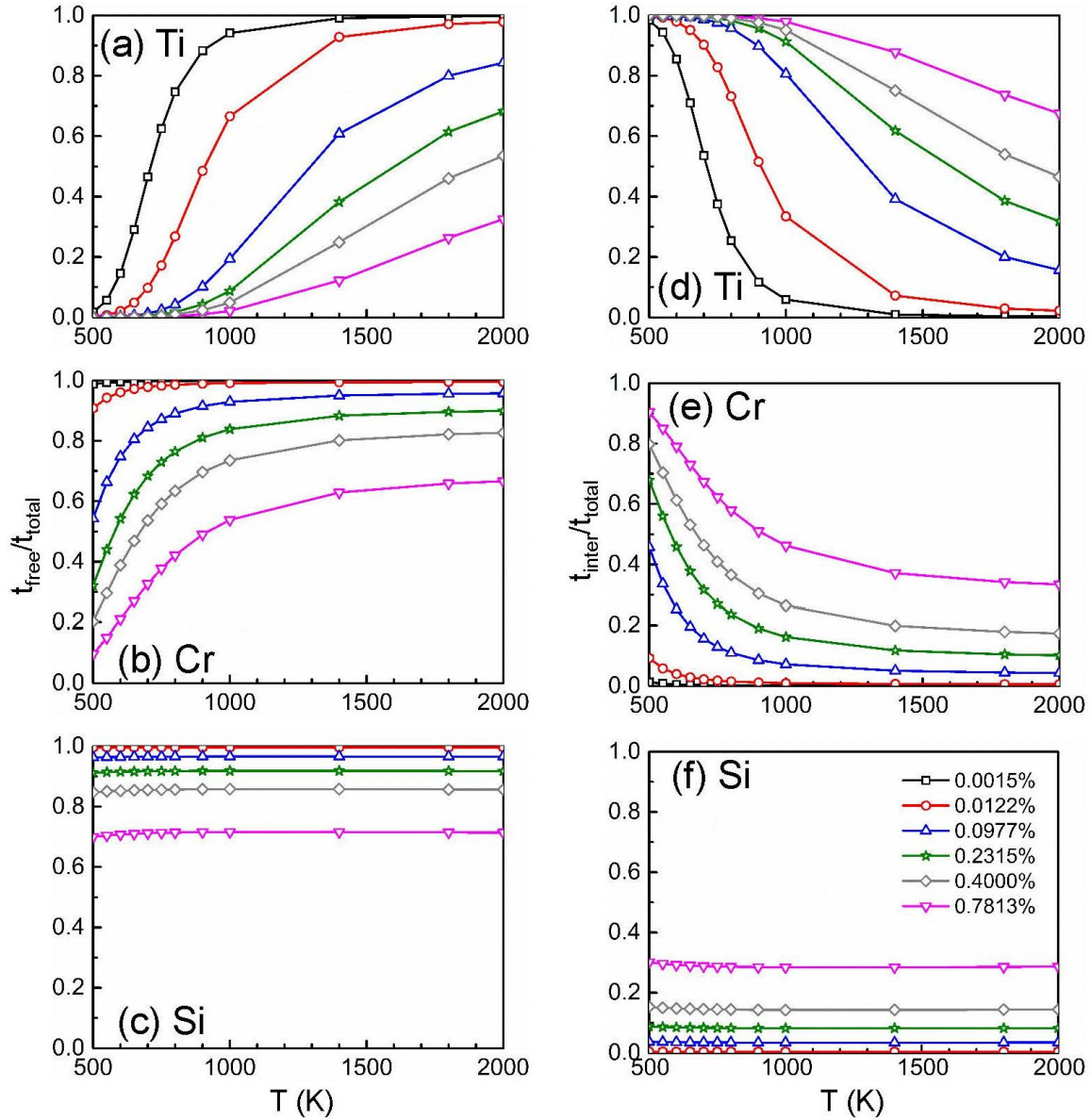


**Figure 4.4.** The time ratios  $t_{\text{free}}/t_{\text{total}}$  (left) and  $t_{\text{inter}}/t_{\text{total}}$  (right) in dependence on temperature and concentration.

The time ratios  $t_{\text{free}}/t_{\text{total}}$  and  $t_{\text{inter}}/t_{\text{total}}$  according to Eq. (4.3) are shown in Fig. 4.4. Due to the attraction between oxygen and Ti and between oxygen and Cr at the first- and second-neighbor distances, in these states the residence time of the diffusing atom is relatively high at low temperatures (see also section 3.3.2). This leads to high values for  $t_{\text{inter}}/t_{\text{total}}$  and low values for  $t_{\text{free}}/t_{\text{total}}$ . The opposite behavior is found at high temperatures. The higher the concentration of the substitutional solute the lower (higher) are the values of  $t_{\text{free}}/t_{\text{total}}$  ( $t_{\text{inter}}/t_{\text{total}}$ ) at a given temperature. On the other hand,

the interaction between oxygen and Si is repulsive and weakly attractive. Therefore,  $t_{\text{inter}} / t_{\text{total}}$  ( $t_{\text{free}} / t_{\text{total}}$ ) is low (high) within the whole temperature range.

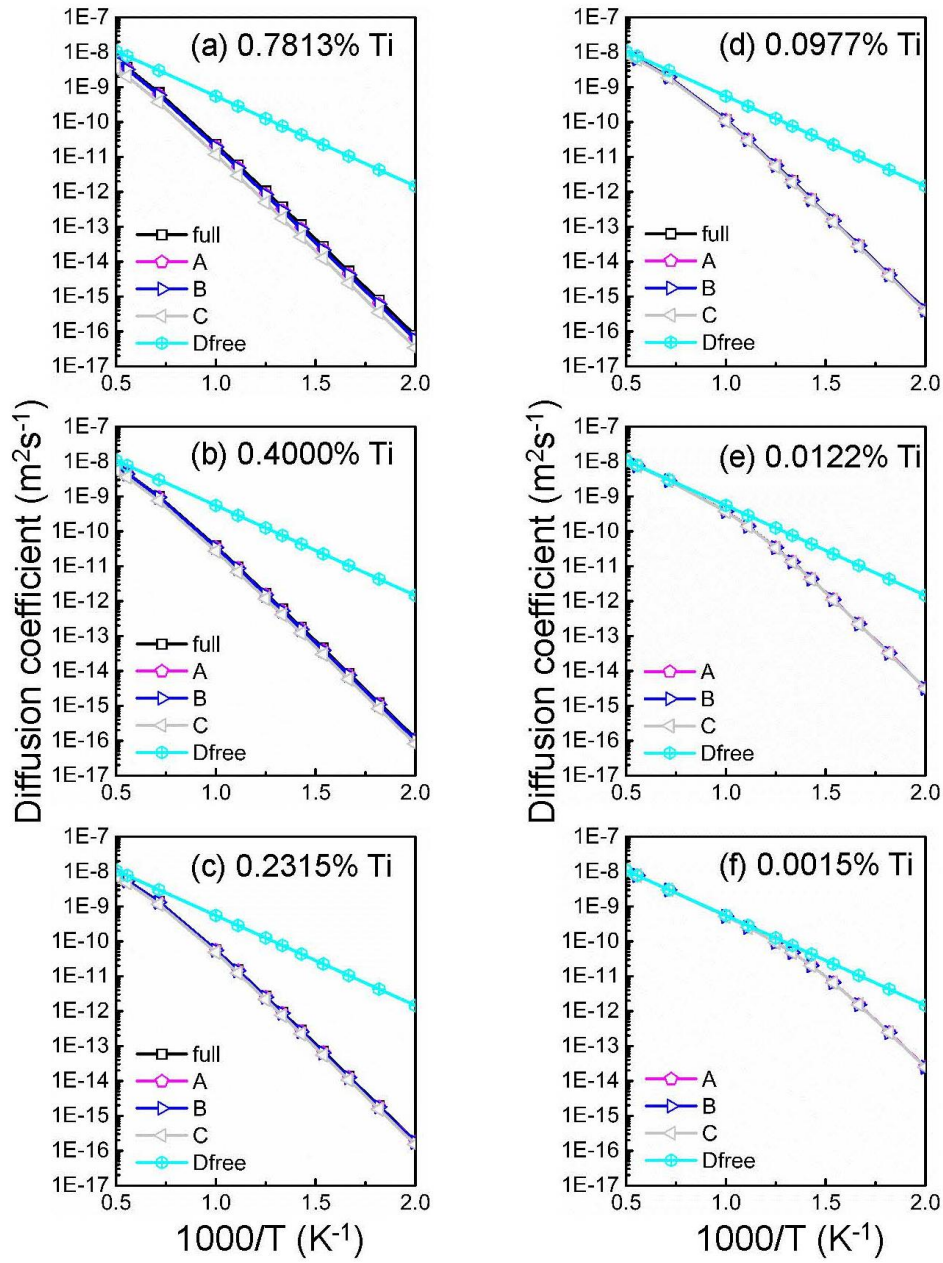
A verification that the ratios  $t_{\text{free}} / t_{\text{total}}$  and  $t_{\text{inter}} / t_{\text{total}}$  determined by Eq. (4.3) are equivalent to those calculated by separate AKMC simulations for different concentrations of the substitutional solutes is also important. It was found that the relative deviation of the AKMC data from those determined by Eq. (4.3) is below about 2% in the temperature range between 500 and 2000 K, for all concentrations of Ti, Cr, and Si considered. These results justify the use of Eq. (4.3), in combination with Eqs. (4.1) and (4.2), to determine the total oxygen diffusion coefficient at given concentration and temperature.

### 4.3.3 Total diffusion coefficient

Data for the total diffusion coefficient  $D$  of oxygen in the different dilute alloys are depicted in Fig. 4.5. They were calculated using four different methods: (i) by full AKMC simulations as in Chapter 3, (ii) by Eqs. (4.1) and (4.2), i.e. with  $D_{\text{inter}}$ ,  $t_{\text{free}} / t_{\text{total}}$  and  $t_{\text{inter}} / t_{\text{total}}$  from AKMC simulations, (iii) by Eqs. (4.1)-(4.3), i.e. with a concentration-independent value of  $D_{\text{inter}}$  from AKMC simulations (taken from Fig. 4.2 for the concentration of 0.0977%), and (iv) using the equation

$$D = \frac{t_{\text{free}}}{t_{\text{total}}} D_{\text{free}} \quad (4.4)$$

with  $t_{\text{free}} / t_{\text{total}}$  from (4.3a).



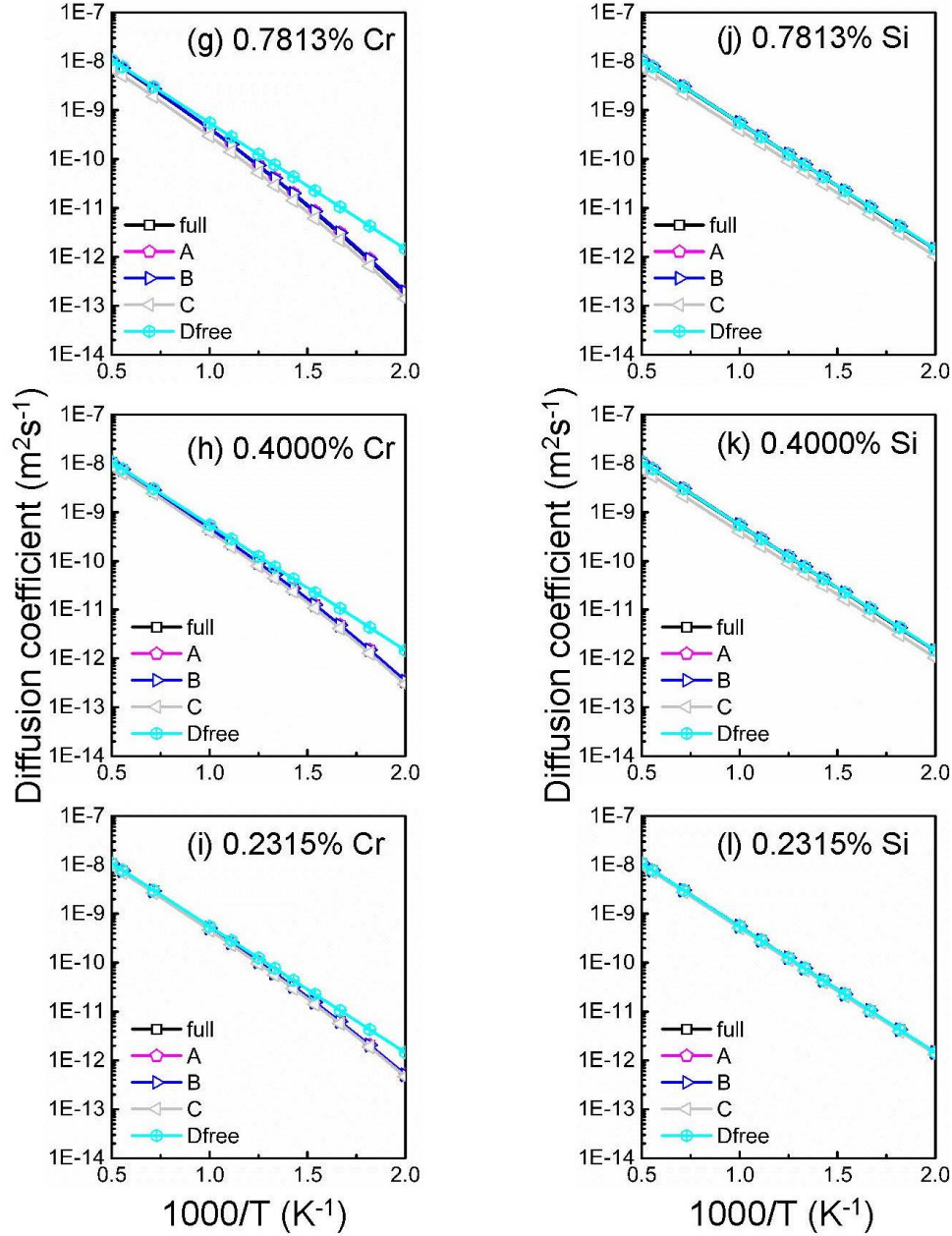


**Figure 4.5.** Total diffusion coefficient  $D$  of oxygen in dependence on temperature and solute concentration obtained by different calculation methods. Curves marked by ‘full’ show results from full AKMC simulations (see section 3.3.2). ‘A’ denotes the data determined by Eqs. (4.1) and (4.2) with the time ratios and  $D_{\text{inter}}$  from AKMC simulations for the respective concentrations  $c_s$ . Data determined by (4.1)-(4.3) with  $D_{\text{inter}}$  from AKMC simulations are marked by ‘B’, while results from (4.4) with  $t_{\text{free}}/t_{\text{total}}$  from (4.3) are denoted by ‘C’. The diffusion coefficient of oxygen in pure bcc Fe ( $D_{\text{free}}$ ) is plotted as reference. For Cr or Si below 0.2315%

the difference between  $D$  and  $D_{\text{free}}$  is very small. Therefore these data are not shown.

In Eq. (4.4) merely DFT binding energy data and the migration barrier of oxygen in pure bcc Fe are required. Fig. 4.5 clearly shows that the data obtained by methods (i-iii) are more or less equal for the concentrations of substitutional solutes considered. It must be also stressed that the slight concentration dependence of  $D_{\text{inter}}$  found at higher fractions of Ti is not visible in the Arrhenius plot for  $D$  (Fig. 4.5). In many cases, especially for low concentrations, even the data obtained by all the four methods agree very well. Under this condition  $D$  can be easily obtained by Eq. (4.4) for which the knowledge of the binding energies  $E_{\text{bind}}^i$  and  $D_{\text{free}}$  is sufficient. This kind of calculation does not require any AKMC simulations. In the example of the substitutional solute Ti the data for  $D$  in the Arrhenius plot show deviations from a straight line for concentrations below about 0.2315%. In this case the second term of Eq. (4.1a) is generally smaller than the first one so that temperature dependence is only determined by  $t_{\text{free}}/t_{\text{total}}$  times  $D_{\text{free}}$ , i.e. by Eq. (4.4). If the interaction with oxygen is repulsive and weakly attractive as in the case of Si,  $D_{\text{inter}}$  is nearly equal to  $D_{\text{free}}$  (see Fig. 4.2) and for higher concentrations both  $t_{\text{inter}}/t_{\text{total}}$  and  $t_{\text{free}}/t_{\text{total}}$  must be taken into account (see Fig. 4.4). Therefore, in Figs. 4.5 the results obtained by Eq. (4.4) slightly differ from the others at concentrations of 0.7813 and 0.4000%. At lower concentrations  $D$  becomes more or less equal to  $D_{\text{free}}$ .

#### 4.4 Conclusions

In conclusion, effective procedures to determine the diffusion coefficient of interstitial oxygen in dilute ferritic iron alloys have been presented and the limits of their applicability are discussed. In comparison with investigations on interstitial oxygen diffusion in Chapter 3, AKMC simulation must be performed only for one concentration of the substitutional solute which leads to a considerably shorter computing time. For sufficiently low concentrations of substitutional atoms (below 0.2315 at. %), it is even possible to determine the oxygen diffusion coefficient using an analytical expression where only diffusion coefficient of oxygen in pure bcc Fe and binding energies of oxygen and substitutional solutes at different neighbor distances are needed, i.e. no further AKMC calculation is required. The calculation methods described in this chapter

can be used for other interstitial diffusers in dilute iron alloys and also to interstitial diffusion in other host materials with small concentrations of substitutional solutes.

The method described above may be also called cluster expansion approach of diffusion. A similar but more general approach which is based on the self-consistent mean field approach was recently developed by other authors [55-57]. In Appendix III it is shown that that approach and the method presented in this chapter lead to nearly identical results.

## **Chapter 5 Mutual dependence of oxygen and vacancy diffusion in bcc Fe and dilute iron alloys**

### **5.1 Introduction**

The focus of the present chapter is on the mutual dependence of oxygen and vacancy diffusion in bcc Fe and dilute iron alloys. DFT calculations are used to determine the binding energy between oxygen and the vacancy for different distances, and to obtain the migration barriers for oxygen in the environment of a vacancy and for the vacancy in the environment of an oxygen atom. Using the data determined by DFT as inputs for the efficient calculation method described in Chapter 4, the simultaneous migration of O and v is considered. At first the diffusion coefficients of oxygen in a model system with fixed vacancy concentrations, the diffusion coefficients of the vacancy for fixed oxygen concentrations, and the diffusivity of the Ov pair are determined. In reality the vacancy and oxygen concentrations in dilute Fe-based alloys are determined by the thermal equilibrium with other foreign atoms and intrinsic defects or are affected by external conditions. Vacancy concentrations significantly above the equilibrium value in pure bcc Fe may occur due to irradiation, strong plastic deformation, mechanical alloying, etc. An example of the latter case is the production of Oxide Dispersion Strengthened (ODS) Fe-based alloys using powder technology. In this chapter the oxygen and vacancy diffusion in the first stage of thermal processing of the ODS alloys is investigated using the DFT data for binding and migration energies. Since the initial powder contains not only relatively high concentrations of oxygen and vacancies but also Y and Ti, the influence of these most relevant substitutional solutes is also considered. In contrast to O and v the substitutional atoms Y and Ti can be assumed to be immobile. In the last part of this chapter O and v diffusion is studied for pure bcc Fe with an oxygen content close to the thermal solubility. The calculated diffusion coefficient of oxygen is compared with the few available experimental data.

### **5.2 DFT Calculations**

#### **5.2.1 Computational method**

The calculations were performed within the framework of DFT as implemented in the Vienna ab initio simulation package (VASP) [25-27]. The same settings as in section 3.2.1 were employed: (i) Pseudopotentials generated by the projector-augmented wave [29,30] approach were used. (ii) Exchange and correlation effects

are described by the generalized gradient approximation with the Perdew-Burke-Ernzerhof parametrization [24]. (iii) A supercell consisting of  $4 \times 4 \times 4$  bcc unit cells was considered and a  $3 \times 3 \times 3$   $k$  point grid was employed for the Brillouin-zone sampling within the Monkhorst-Pack scheme [31]. (iv) For the integration in the reciprocal space the Methfessel-Paxton smearing method [45] was applied with a width of 0.2 eV. (v) All calculations were carried out within the framework of the spin-polarized formalism and with a plane-wave cutoff energy of 500 eV. (vi) After introduction of foreign atoms or of a vacancy into the supercell, the position of atoms as well as the volume and shape of the supercell were relaxed so that the total stress/pressure of the supercell tends to zero. (vii) The convergence criteria were set to  $10^{-2}$  eV/Å and  $10^{-5}$  eV for the residual force per atom and the change of total energy in one iteration step, respectively.

As shown in previous investigations [42-44,46-48], oxygen prefers the octahedral interstitial sites in bcc Fe, and the most stable site for vacancy is the bcc lattice site.

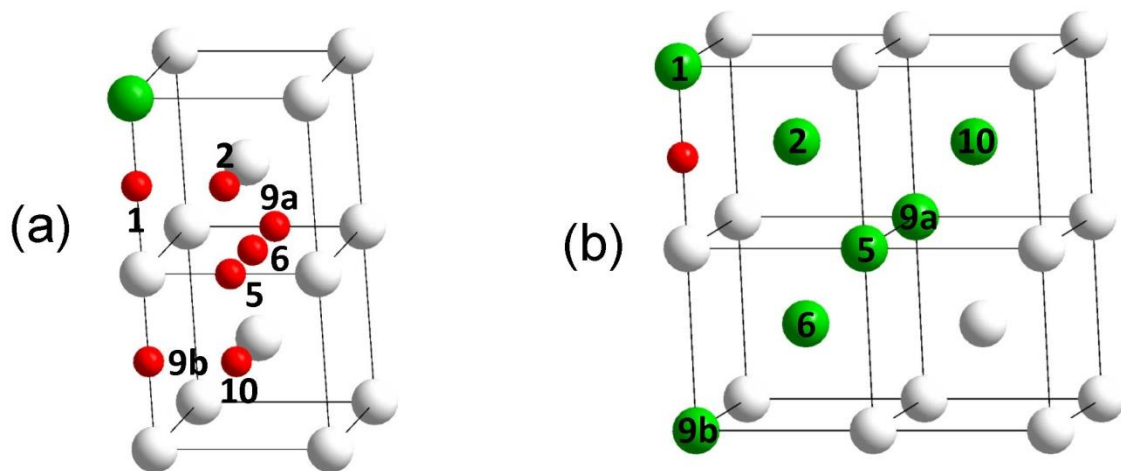


**Figure 5.1** (a) Examples for octahedral interstitial sites of oxygen (red) in the neighborhood of a vacancy (green). Neighbors inside the interaction region considered in DFT calculations are marked by black numbers. The gray spheres represent Fe atoms. (b) Examples for bcc sites of the vacancy (green) in the neighborhood of an oxygen atom (red). The meaning of the black numbers is the same as in (a).

Fig. 5.1 (a) [Fig. 5.1 (b)] illustrate the neighboring octahedral interstitial (substitutional) sites of a vacancy (oxygen) up to the 10<sup>th</sup> neighbor position. The notation and



numbering of the neighbor positions is according to the scheme for the underlying simple cubic lattice (see Chapter 3 and [15,58]) which consists of bcc lattice sites and all octahedral interstitial sites of the bcc lattice. Within this scheme oxygen cannot reside on third-neighbor, fourth-neighbor, seventh-neighbor, eighth-neighbor, etc., positions of the vacancy since these sites are already occupied by iron atoms. Furthermore, there are two different ninth-neighbor sites (9a and 9b).

The binding energy of an oxygen-vacancy (Ov) pair at a certain distance is determined by

$$E_{bind} = E(Ov) + E_0 - E(v) - E(O), \quad (5.1)$$

with  $E_0$  as the total energy of the perfect bcc Fe supercell.  $E(Ov)$ ,  $E(v)$ , and  $E(O)$  denote the total energy of the supercell with the Ov pair, with a single vacancy, and a single oxygen atom, respectively. Negative values of the binding energy mean that the interaction is attractive.

The minimum energy paths and the respective migration barriers for oxygen and the vacancy were calculated using the standard nudged elastic band (NEB) method and, subsequently, the climbing-image NEB method, see section 2.3.2. For comparison, also the solid-state NEB [59] was employed in some cases. The results do not differ significantly from those obtained by the combination of standard NEB and climbing-image NEB. For all these calculations the vtsttools [60] provided by the Henkelman group at the University of Texas (Austin) were used.

### 5.2.2 Binding energy of oxygen-vacancy pairs at different distances

The binding energies of the Ov pair up to the 10<sup>th</sup> neighbor distance are summarized in Table 5.1. The most attractive state is found for the first neighbor distance, and the attraction is still appreciable at the second neighbor distance. With increasing distance, the interaction becomes weaker. Most of the binding energy data determined in the present work are consistent with previous DFT results [15,16,43,44,47].

**Table 5.1** Binding energy of the Ov pair at different distances between O and v (see Fig. 5.1). In this work the pair at the 6<sup>th</sup> neighbor distance was found to be not stable, i.e. the vacancy relaxes to the first neighbor distance with respect to O. The value with asterisk (-0.34 eV) corresponds to the binding energy at a transition state which was found during the relaxation calculations (see text). DFT data from literature are also given.

Neighbour position	1	2	5	6	9a	9b	10
$E_{bind}$ (eV)	-1.596	-0.697					
	-1.52 [15]	-0.58 [15]	-0.126	-0.34*			
	-1.53 [16]	-0.65 [16]	-0.05 [15]	-0.35 [15]	0.019	0.138	
	-1.45 [42]	-0.60 [42]	-0.08 [16]	-0.37 [44]	0.01 [47]	0.22 [47]	0.015
	-1.65 [43]	-0.75 [43]	-0.14 [44]				
	-1.69 [44]	-0.73 [44]					

A peculiarity was found for O and v at the 6<sup>th</sup> neighbor distance. This state is not stable, i.e. during relaxation calculation the vacancy moves to the first neighbor distance with respect to O. This result could be also reproduced with supercells containing  $3\times 3\times 3$  and  $5\times 5\times 5$  bcc unit cells and in a calculation with a higher precision (convergence criteria  $10^{-4}$  eV/Å and  $10^{-9}$  eV for force and energy change, respectively) for a supercell with  $4\times 4\times 4$  unit cells. For a supercell with  $4\times 4\times 4$  bcc unit cells also relaxation calculations at constant volume were performed, and the result was very similar to that obtained by the other calculations. The relaxation process was studied in more detail, and it was found that before completely relaxing to the 1<sup>st</sup> neighbor distance a transition state of the Ov pair can be identified. For this non-stable state, a “quasi-binding energy” of about -0.34 eV could be estimated. This value is very similar to that obtained in previous DFT calculations (-0.37 eV [44], -0.35 eV [15]) for the binding energy of the Ov pair at the 6<sup>th</sup> neighbor distance. In contrast to the result of this work these authors consider the Ov pair at the 6<sup>th</sup> neighbor distance as a (meta)stable. On the other hand, Barouh *et al.* [15] found that the migration barrier for the vacancy jump from the 6<sup>th</sup> to the 1<sup>st</sup> neighbor distance is 0, which is in accord with the result of the present work, showing that the Ov pair at the 6<sup>th</sup> neighbor distance is not really stable.

From previous DFT calculations it is known that the incorporation of an oxygen atom on an octahedral interstitial site of the bcc Fe lattice leads to considerable tetragonal distortion whereas the distortion due to the first-neighbor Ov pair is much smaller (see [48]). In the present work tetragonal distortions are also found for 1<sup>st</sup>, 2<sup>nd</sup>, and 9<sup>th</sup> neighbor Ov pairs. The instability of the 6<sup>th</sup> neighbor pair could be explained by the fact that such an atomic configuration causes very strong distortions, leading to an immediate relaxation towards the 1<sup>st</sup> neighbor pair.

### **5.2.3 Migration barriers**

#### **5.2.3.1 Oxygen and vacancy migration in pure bcc Fe**

Oxygen diffusion in perfect bcc Fe was already treated in section 3.2.2. Vacancy migration from one bcc site to the nearest neighbor bcc site corresponds to a jump of a Fe atom in the opposite direction. NEB calculations showed that the minimum energy path is a straight line with a migration barrier of 0.695 eV. This value is in good agreement with previous DFT results (0.68 eV [48], 0.64 eV [61], 0.65 eV [62], 0.67 eV

[63], 0.68 eV [64], 0.66 eV [65], 0.67 eV [66]). The saddle point of the nearest neighbor vacancy jump corresponds to the atomic configuration with the jumping Fe atom in the middle between the original and the final site of the vacancy. It should be noticed that the jump distance of the vacancy corresponds to a third neighbor distance in the underlying simple cubic lattice. Using the calculation method described in Chapter 2, an attempt frequency of 15.33 THz was obtained for the vacancy jump in pure bcc Fe. This value is comparable with the result (11.6 THz) of recent DFT calculations [52]. Investigations of vacancy jumps over second and third neighbor distances of the bcc lattice showed that in pure bcc Fe these long-distance jumps consist of successive nearest neighbor jumps between bcc lattice sites. It is worth mentioning that different Fe atoms take part in these successive nearest neighbor jumps of the vacancy.

Since the migration barriers of O (0.512 eV) and v (0.695 eV) are in the same order of magnitude, the mobility of both species must be considered in order to determine the diffusion coefficient of oxygen in bcc Fe in the presence of a vacancy and to calculate the diffusion coefficient of the vacancy in the presence of oxygen. This is different to investigations in Chapter 3 on the influence of substitutional foreign atoms on the migration of oxygen, with O as the only mobile species.

### 5.2.3.2 Vacancy influence on oxygen migration barriers, and oxygen influence on vacancy migration barriers

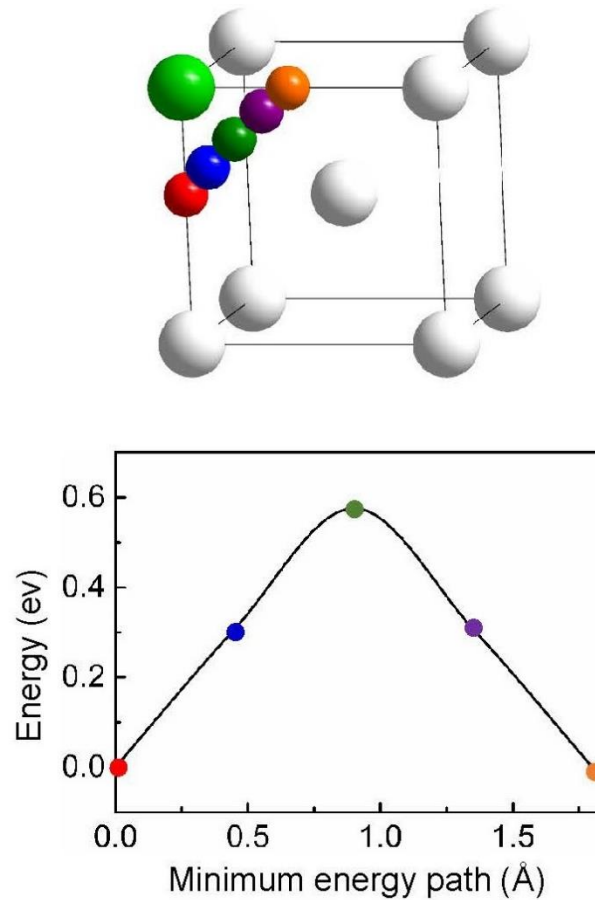


**Figure 5.2** Minimum energy path of the cage jump of oxygen. The large green sphere represents the vacancy.

**(a) Cage jumps of oxygen.** Since the presence of a vacancy is related to additional free volume, the oxygen atom can jump from one nearest neighbor site with respect to the vacancy to another. The corresponding jump length is the second neighbor distance between octahedral interstitial sites. This process is called cage jump [15] and is illustrated in Fig. 5.2. A barrier height of 0.576 eV was obtained from NEB calculations. Barouh *et al.* [15] got a lower value (0.40 eV) which might be explained by the fact that they used the DFT code SIESTA and the drag method to determine migration barriers. The value of 0.576 eV is slightly higher than that for the first neighbor jump of oxygen in pure Fe (0.512 eV, see Chapter 3), but considerably lower compared to barriers for oxygen or for the vacancy which must be overcome to escape the state of the nearest neighbor Ov pair (see below). Therefore, the cage jump is the most probable jump once oxygen and vacancy are trapped at this strong

attractive state. However, as already pointed out by Barouh *et al.* [15] the cage jump of oxygen around the first-neighbor vacancy does not really contribute to net diffusion of oxygen, the vacancy, and the oxygen-vacancy pair.

**(b) Nearest neighbor O and v jumps as well as simultaneous jumps of O and v.** In order to calculate the possible migration barriers by the NEB method two cases were considered: (i) oxygen jumps if the vacancy position is fixed, and (ii) vacancy jumps if the oxygen position is fixed. The connectivity plot depicted in Fig. 5.3 (a) illustrates all potential jumps of O and v within the interaction region, i.e. up to the 10<sup>th</sup> neighbor distance. The dotted and dashed lines mark jumps that are not possible in reality, due to the instability of the Ov pair at the 6<sup>th</sup> neighbor distance (see above) and because of the problem with the vacancy jump between states 2 and 5 (see below), respectively.

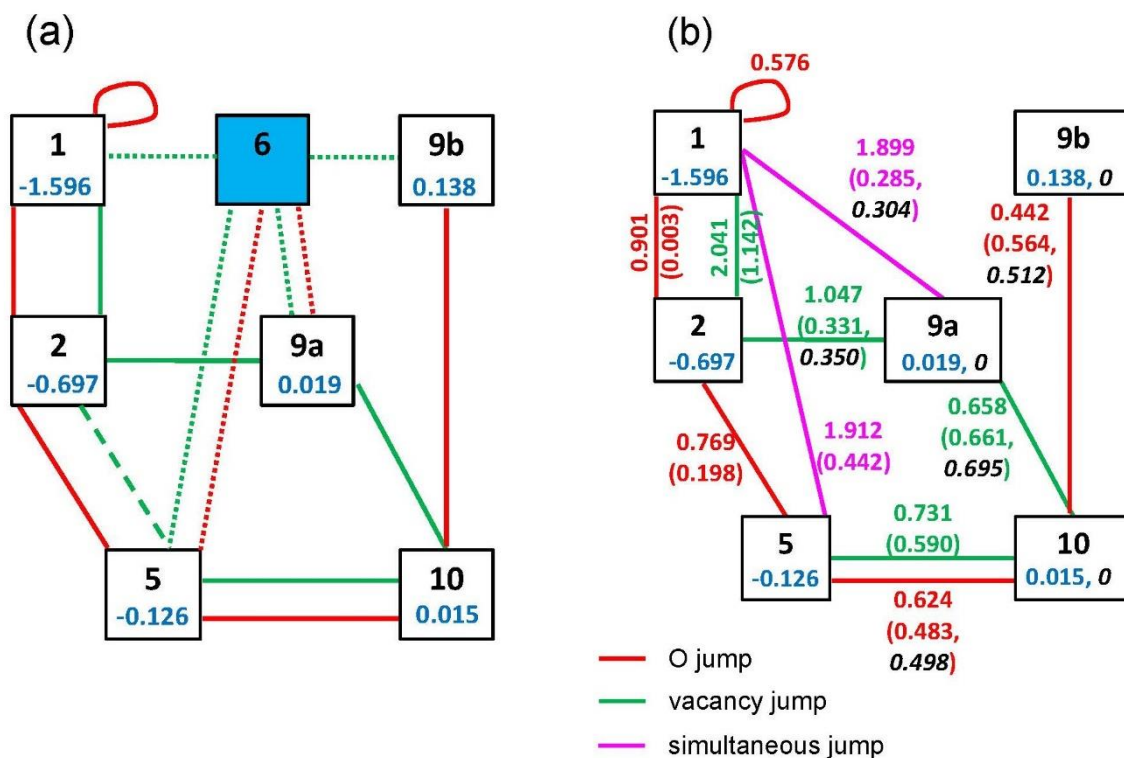


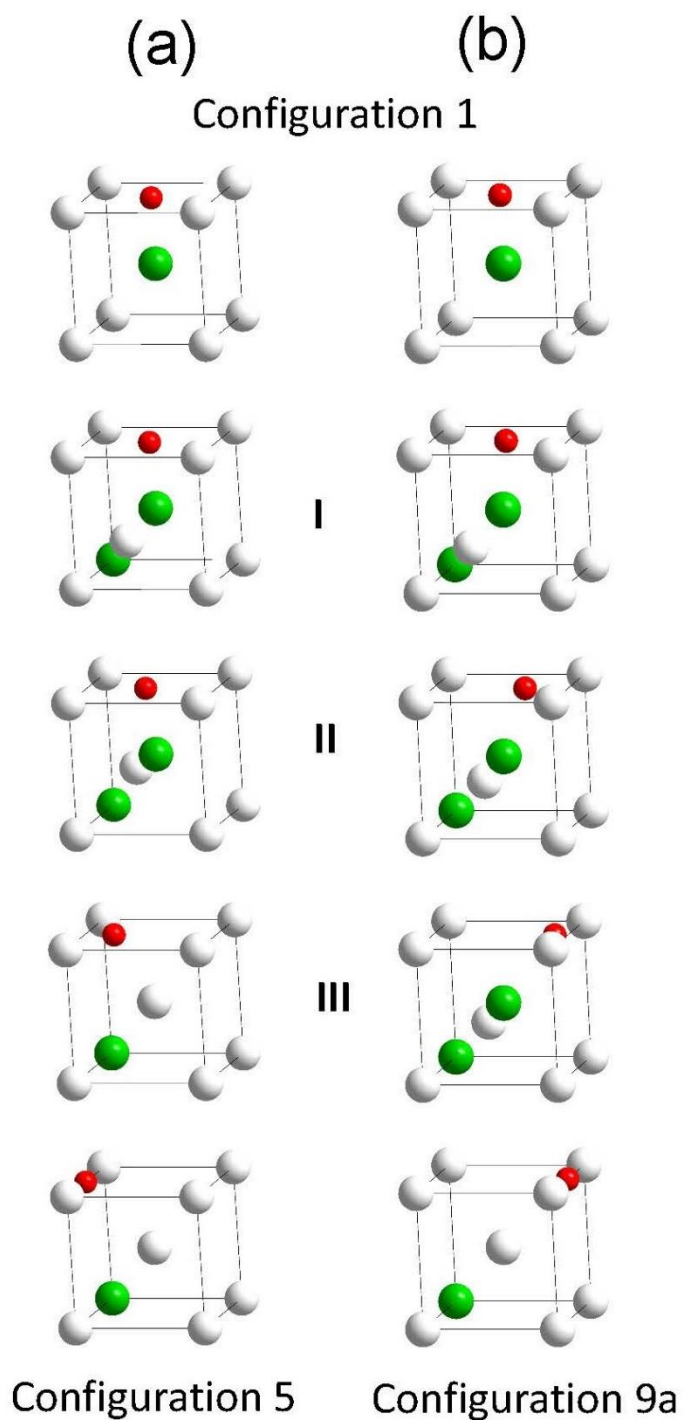
**Figure 5.3** Graphical representation of possible jumps of oxygen and the vacancy between different neighbor positions (connectivity plots). Potential jumps (O: red, v: green) including the 6<sup>th</sup> neighbor position are depicted in (a). However, the instability of the Ov pair at the 6<sup>th</sup> neighbor distance makes jumps marked by dotted lines impossible. For other reasons (see text) the direct vacancy jump marked by the

dashed line is not possible. Figure (b) illustrates the really relevant neighbor positions and jumps. Jump barriers for forward and backward jumps are given in eV, e.g. for oxygen jump from 2 to 5 the barrier is 0.769 eV, while it is 0.198 eV for the jump from 5 to 2. In both figures the binding energy of the Ov pair at given distance is marked by blue color. The black italics numbers in figure (b) show the binding energies and migration barriers modified due to the rule of detailed balance (see text).

Fig. 5.3 (b) shows the barriers for oxygen jumps between nearest neighbor octahedral sites, in the neighborhood of the vacancy (1-2, 2-5, 5-10, and 9b-10), as well as the barrier for the cage jump. The values for the O jumps from 1 to 2 and 2 to 1 as well as from 2 to 5 and 5 to 2 are consistent with results of Barouh *et al.* [15]. The data for vacancy jumps between nearest neighbor bcc lattice sites, in the neighborhood of oxygen (1-2, 2-9a, 5-10, 9a-10), are also given in Fig. 5.3 (b). As already mentioned, in the present work migration barriers were determined up to the 10<sup>th</sup> neighbor distance. It is assumed that at larger distances the interaction between O and v is negligible so that in this region the migration energies of both species correspond to that in pure bcc Fe.

If the Ov pair at the 6<sup>th</sup> neighbor distance were stable, both O and v could jump between the 5<sup>th</sup> and the 6<sup>th</sup> neighbor as well as between the neighbors 9a and 6, see Fig. 5.3 (a). These two cases are worth investigating in more detail. Due to the instability of the Ov pair at the 6<sup>th</sup> neighbor distance the attempt of an oxygen jump from 5 towards 6 causes a simultaneous (or coupled) vacancy jump so that finally both species are at the 1<sup>st</sup> neighbor distance. NEB calculations yield a barrier of 0.442 eV for such a simultaneous jump of both O and v. Fig. 5.4 shows the initial, intermediate, and final atomic configurations for this case. The opposite jump has a much higher barrier (1.912 eV). Also the attempt of an oxygen jump from 9a towards 6 leads to a simultaneous v jump which results in a final configuration with both species at the 1<sup>st</sup> neighbor distance. The barrier of this simultaneous jump is 0.285 eV, and the initial, intermediate and final atomic configurations are also depicted in Fig. 5.4. The barrier for the opposite jump is 1.899 eV. It is interesting that in the cases illustrated in Fig. 5.4 the relatively high barriers for the jumps between 1 and 5 as well as between 1 and 9a are comparable with the barrier for the jump of the vacancy from 1<sup>st</sup> to 2<sup>nd</sup> neighbor of O [Fig. 5.3 (b)], and these barriers are somewhat higher than the combination of successive jumps of O from 1 to 2 and from 2 to 5 (1.667 eV). The two simultaneous

jumps of Fig. 5.4 are marked by magenta color in the connectivity plot depicted in Fig. 5.3 (b).





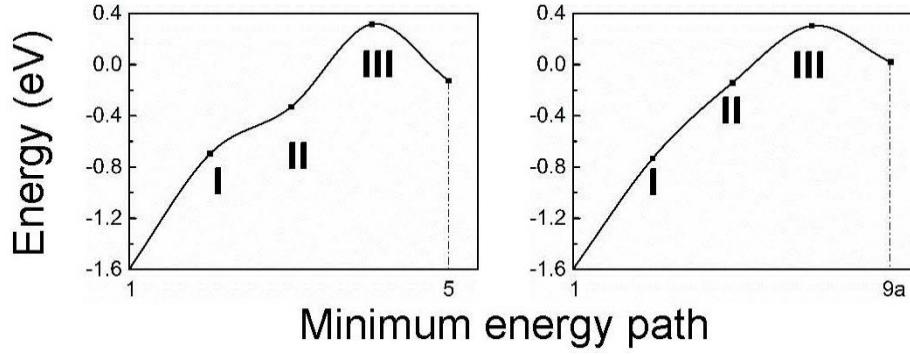


**Figure 5.4** Atomic configurations illustrating the simultaneous (or coupled) jumps between the 1st and the 5th neighbor position (a) and between the neighbor positions 1 and 9a (b). The scale on the ordinate concerns the binding energy of the Ov pair (see Table 5.1).

A barrier for the direct vacancy jump between the 2<sup>nd</sup> and the 5<sup>th</sup> neighbor of O could be not determined by the NEB method due to lacking convergence. Therefore, these jumps are not considered in the present work. It might be possible that Barouh *et al.* [15] faced a similar problem, since they did not show results for those jumps. Obviously, the difficulty to determine the above mentioned barriers is caused by the negligible barrier (0.003 eV) for the O jump between the 2<sup>nd</sup> and the 1<sup>st</sup> neighbor of v: If v attempts to jump from the 2<sup>nd</sup> to the 5<sup>th</sup> neighbor of O, at first the oxygen atom may migrate to the 1<sup>st</sup> neighbor octahedral interstitial site of v. Then, the first simultaneous jump mechanism as described above may occur, i.e. O and v are initially at the 1<sup>st</sup> neighbor distance, and finally at the 5<sup>th</sup> neighbor distance. These assumptions are supported by the fact that the (not fully convergent) NEB calculations for the direct vacancy jump between the 2<sup>nd</sup> and the 5<sup>th</sup> neighbor of oxygen yield a local minimum with an atomic configuration and a binding energy which correspond to O at the 1<sup>st</sup> neighbor site of the v.

### 5.3 AKMC basics and determination of diffusion coefficients in a model system

In order to use the NEB data for migration barriers in AKMC simulations in a consistent manner, the rule of detailed balance must be obeyed

$$E_m^{i,j} - E_m^{j,i} = E_{bind}^j - E_{bind}^i \quad (5.2)$$

(see Chapter 3) for all the O and v jumps shown in the connectivity plot of Fig. 5.3 (b).  $E_{bind}^k$  and  $E_m^{k,l}$  are the binding energy between O and v at the  $k$  th neighbor distance and the migration barrier for the jump between the  $k$  th and  $l$  th neighbor distance, respectively. In present AKMC simulations the binding energy of the Ov pair at and beyond the 9<sup>th</sup> neighbor distance was set to zero and in these regions the migration energy of O and v was set to the corresponding values in pure bcc Fe. Therefore, some of the NEB barriers at the rim of the interaction region had to be modified using Eq. (5.2). The modified data are also shown in Fig. 5.3 (b).

In AKMC simulations a rigid lattice consisting of bcc lattice sites and octahedral interstitial sites is used. Therefore, the simultaneous (or coupled) jumps must be described in an approximate manner. In the case shown in Fig. 5.4 (a), in the forward direction v jumps from the 1<sup>st</sup> to the 6<sup>th</sup> neighbor position (barrier 1.912 eV), afterwards O is simply shifted to the 5<sup>th</sup> neighbor position of v. In the opposite direction O jumps from the 5<sup>th</sup> to the 6<sup>th</sup> neighbor position of v (barrier 0.442 eV), then v is shifted to the 1<sup>st</sup> neighbor position of O. The jump depicted in Fig. 5.4 (b) is also modeled in two steps. In one direction v jumps to the 6<sup>th</sup> neighbor distance (barrier 1.899 eV) followed by the shift of O to the neighbor position 9a. In the other direction, O jumps to the 6<sup>th</sup> neighbor distance (barrier 0.304 eV, correction due to detailed balance), followed by a shift of v to the 1<sup>st</sup> neighbor distance of O.

The AKMC simulations used here are based on the residence time algorithm as described in section 2.3.5. However, not only oxygen but also the vacancy must be considered as mobile. In Chapter 4, an efficient method was presented to determine the diffusion coefficient of oxygen in bcc Fe under the influence of a low concentration of foreign atoms at substitutional site. Such a procedure is also used here. In the following two subsections a model system with fixed vacancy or oxygen concentrations is considered in order to demonstrate the effect of vacancies on O diffusion and the influence of oxygen on v diffusion. In the following more realistic examples are studied.

### 5.3.1 The diffusion coefficient of oxygen in the presence of vacancies

For a given temperature and a given (sufficiently low) concentration of vacancies the diffusion coefficient of O can be determined according to section 4.2

$$D = \frac{t_{free}}{t_{total}} D_{free} + \frac{t_{inter}}{t_{total}} D_{inter} \quad (5.3a)$$

with

$$t_{total} = t_{free} + t_{inter} \quad (5.3b)$$

The first and second term is related to the diffusion of oxygen in perfect bcc Fe and within the region of interaction between oxygen and a vacancy, respectively.  $D_{free}$  denotes the diffusivity of oxygen in pure Fe, and  $D_{inter}$  denotes the diffusivity of oxygen in the interaction region.  $D_{free}$  can be obtained by the analytical expression (see section 2.3.4)

$$D_{free} = \frac{a^2}{6} \nu_0^{free} \exp\left(\frac{-E_m^{free}}{k_B T}\right), \quad (5.4)$$

with the attempt frequency  $\nu_0^{free} = 15.76$  THz and the migration barrier  $E_m^{free} = 0.512$  eV, while  $a = 2.832$  Å is the lattice constant in bcc Fe (see also section 4.2). The diffusion coefficient  $D_{inter}$  must be determined by AKMC simulations taking into account that O as well as v are mobile. In the dilute limit, which is considered throughout the present work for the concentrations of species that influence O (or v) diffusion,  $D_{inter}$  is nearly independent of the concentration of these species, i.e. nearly independent of the size of the AKMC simulations cell, see Chapter 4. Therefore,  $D_{inter}$  can be determined by AKMC calculations for only one specific v concentration. In the interaction region the jumps are simulated using the attempt frequencies  $\nu_0^{free}$  for O (or v) and barriers according to Fig. 5.3 (b). The quantities  $t_{free}$  and  $t_{inter}$  denote the sum of the time periods for diffusion outside and inside the interaction region, respectively, and  $t_{total}$  is the total diffusion time.

The time ratios in Eq. (5.3a) are given by the analytical expressions (see Chapter 4),

$$\frac{t_{free}}{t_{total}} = \frac{1 - \sum_i N_i C_v}{1 - \sum_i N_i C_v + \sum_i N_i \exp\left(-\frac{E_{bind}^i(Ov)}{k_B T}\right) C_v} \quad i = 1, 2, 5 \quad (5.5a)$$

$$\frac{t_{\text{inter}}}{t_{\text{total}}} = \frac{\sum_i N_i \exp\left(-\frac{E_{\text{bind}}^i(\text{Ov})}{k_B T}\right) C_v}{1 - \sum_i N_i C_v + \sum_i N_i \exp\left(-\frac{E_{\text{bind}}^i(\text{Ov})}{k_B T}\right) C_v} \quad (5.5b)$$

$$(N_1 = 2, N_2 = 4, N_3 = 8),$$

with the vacancy concentration  $C_v$ , and the binding energy  $E_{\text{bind}}^i(\text{Ov})$  of the Ov pair at the  $i$ th neighbor distance (see Table 5.1, neighbor denotation according to Fig. 5.1), and  $N_i$  is the number of possible vacancy sites at the  $i$ th neighbor distance from O. Here neighbors beyond  $i=5$  are not taken into account because of the low binding energy. Note that in the dilute limit  $\sum_i N_i C_v$  is small compared to

$$\sum_i N_i \exp\left(-\frac{E_{\text{bind}}^i(\text{Ov})}{k_B T}\right) C_v.$$

As already discussed in Chapter 4, the use of relations such as Eqs. (5.3)-(5.5) to calculate the diffusion coefficient  $D$  for different vacancy concentrations is much more efficient than performing separate AKMC calculations for each concentration using simulation cells with different sizes. This method requires only one AKMC simulation to determine  $D_{\text{inter}}$  and in the remaining calculations one can employ analytical expressions for  $D_{\text{free}}$  and the time ratios. In the present case  $D_{\text{inter}}$  was obtained by AKMC simulations for a vacancy concentration of 0.0977 at%, i.e. using a simulation box consisting of 8x8x8 bcc unit cells with one mobile O atom and one mobile vacancy. In the Arrhenius plot  $D_{\text{inter}}(T)$  is almost straight line, from which the effective activation energy of about 2.0 eV was derived. The time ratios  $t_{\text{free}}/t_{\text{total}}$  and  $t_{\text{inter}}/t_{\text{total}}$  are depicted in Fig. 5.5, for vacancy concentrations of 0.0015, 0.0122, 0.0977, 0.2315, 0.4000, and 0.7813%. With increasing temperature,  $t_{\text{inter}}/t_{\text{total}}$  decreases while  $t_{\text{free}}/t_{\text{total}}$  increases. Due to the strong attraction, in particular at the 1<sup>st</sup> neighbor distance, the quantity  $t_{\text{free}}/t_{\text{total}}$  rapidly decreases if the vacancy concentration increases. For concentrations above 0.0977%  $t_{\text{free}}/t_{\text{total}}$  is nearly zero and  $t_{\text{inter}}/t_{\text{total}}$  is nearly 1, even at elevated temperatures. At low temperature  $t_{\text{free}}/t_{\text{total}}$  converges to zero and  $t_{\text{inter}}/t_{\text{total}}$  approaches 1.

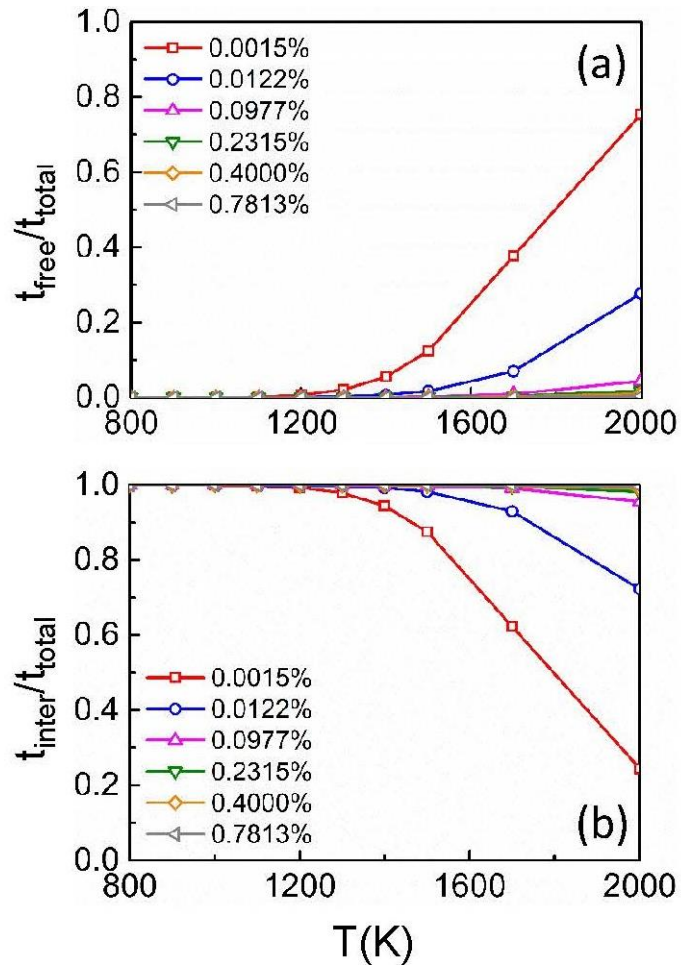


**Figure 5.5** The time ratios  $t_{free}/t_{total}$  (a) and  $t_{inter}/t_{total}$  (b) for oxygen, in dependence on temperature and vacancy concentration.

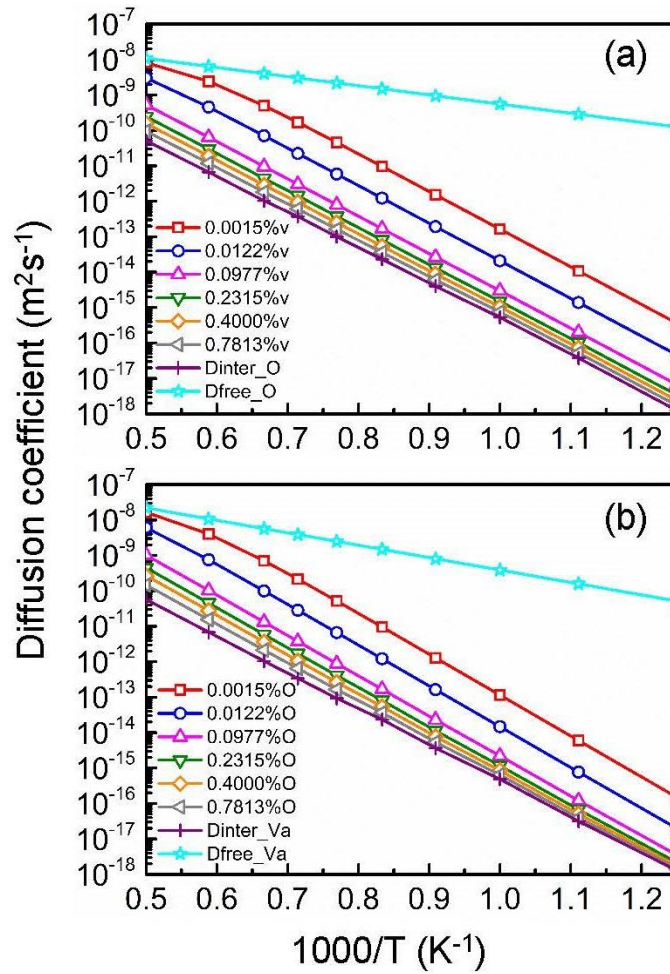


**Figure 5.6** The total diffusion coefficient of oxygen for given concentrations of vacancies (a), and the total diffusion coefficient of the vacancy for different oxygen concentrations (b). The corresponding data of  $D_{\text{free}}$  (cyan) and  $D_{\text{inter}}$  (violet) are also shown.

Fig. 5.6 (a) illustrates the total diffusion coefficient of oxygen in bcc Fe in dependence on the vacancy concentration. The data of  $D$  are between the values of the diffusion coefficient of oxygen in pure Fe ( $D_{\text{free}}$ ) and that inside the region influenced by the vacancy ( $D_{\text{inter}}$ ). The presence of vacancies significantly decreases the mobility of oxygen. For example, at 800 K and a concentration of 0.0015 at% the diffusion coefficient is five to six orders of magnitude lower than that in pure bcc Fe. With increasing vacancy concentration the reduction of  $D$  becomes slower and the value approaches that of  $D_{\text{inter}}$ . This is mainly due to the quick decrease of  $t_{\text{free}}/t_{\text{total}}$  with increasing  $v$  concentration. Note that in this work temperatures below 800 K were not

considered, since in these cases AKMC simulations require extremely long computing times.

The total diffusion coefficient  $D$  can be also determined by

$$D = \frac{t_{free}}{t_{total}} D_{free} \quad (5.6)$$

if the interaction part  $\frac{t_{inter}}{t_{total}} D_{inter}$  is negligibly small compared to  $\frac{t_{free}}{t_{total}} D_{free}$  [see Eq. (5.3a)].

It is found that at concentrations of 0.0015, 0.0122 and 0.0977 at% the total diffusion coefficient can be well reproduced by Eq. (5.6). At higher vacancy concentrations results obtained by (5.6) deviate from those determined by Eq. (5.3a). This is due to the fact that in these cases both terms of Eq. (5.3a) must be taken into account, their absolute values are very small but comparable.

### 5.3.2 The diffusion coefficient of the vacancy in the presence of oxygen

The method used in the last section to evaluate the diffusion coefficient of oxygen is also applied to study vacancy diffusion. The data for the diffusion coefficient of  $v$  in the interaction region with O ( $D_{inter}$ ) were determined by AKMC simulations in a similar manner as  $D_{inter}$  for oxygen. Within the statistical accuracy of the AKMC data  $D_{inter}$  for  $v$  is nearly equal to  $D_{inter}$  for O, with an effective activation energy of about 2.0 eV. The time ratios  $t_{free}/t_{total}$  and  $t_{inter}/t_{total}$  used in the determination of the vacancy diffusion coefficient are calculated in a similar manner as in the case of the oxygen diffusion coefficient. The value of  $D_{free}$  for the vacancy is given by

$$D_{free} = a^2 \nu_0^{free} \exp\left(\frac{-E_m^{free}}{k_B T}\right), \quad (5.7)$$

with  $E_m^{free} = 0.695$  eV and  $\nu_0^{free} = 15.33$  THz (see sections 2.3.4 and 5.2.3.1). Considering both  $v$  and O jumps, AKMC simulations are performed in order to determine the diffusion coefficient of  $v$  in the interaction region with O. The total diffusion coefficient of the vacancy is illustrated in Fig. 5.6 (b) for oxygen concentrations of 0.0015, 0.0122, 0.0977, 0.2315, 0.4000, and 0.7813 at %. The slope of these curves is slightly steeper than that of the curves for O [Fig. 5.6 (a)] because of the somewhat

steeper slope of  $D_{free}$  for the vacancy. The influence of O on the v diffusion coefficient is comparable with the influence of v on O diffusion: At 800 K and an oxygen concentration of 0.0015% the diffusion coefficient is about five to six orders of magnitude lower than that in pure bcc Fe.

All the data presented in this chapter are strictly valid for ferromagnetic iron, i.e., below the Curie temperature of 1043 K. The temperature dependence of the spontaneous magnetization is not taken into account in the calculation of the basic DFT data (binding and migration energy), i.e., for bcc iron always the ground state value of magnetization is assumed. Furthermore, above about 1183 K the fcc phase is most stable, and not bcc Fe. On the other hand, in this work temperatures up to 2000 K are considered in order to verify that the total diffusion coefficient of oxygen and of the vacancy (see Fig. 5.6) approaches the corresponding values for pure bcc Fe at sufficiently high temperature, and in order to study the hypothetical high-temperature behavior of other quantities.

### 5.3.3 The diffusion coefficient of the oxygen-vacancy pair

In AKMC simulations the position of the Ov pair is defined as the middle point between oxygen and vacancy. The calculation of the diffusion coefficient of the Ov pair is very similar to the determination of  $D_{inter}$  for O and v. Fig. 5.7 depicts the result. The activation energy for Ov migration is about 1.95 eV, i.e. only slightly smaller than the activation energies found for  $D_{inter}$  of O and v (see above). This value may be the result of a simultaneous jump from 1<sup>st</sup> to 5<sup>th</sup> neighbor position, followed by an oxygen jump from the 5<sup>th</sup> to the 2<sup>nd</sup> neighbor position [see Fig. 5.3 (b)]. Finally, O jumps to 1<sup>st</sup> neighbor position of v with a negligible barrier of 0.003 eV. During this process the Ov pair has moved by a distance of a 1<sup>st</sup> neighbor distance in bcc Fe (or a 3<sup>rd</sup> neighbor distance in the underlying simple cubic lattice). The most probable minimum energy path for the migration of the Ov pair is illustrated in detail in Fig. 5.8. The scale in Fig. 5.8 concerns the binding energy of the Ov pair. The difference between the lowest value (about -1.6 eV, see also Table 5.1) and the highest value gives about 1.95 eV, i.e. the activation energy extracted from Fig. 5.7. for Ov pair migration. The present results are also in good agreement with the global migration energy of 1.90 eV determined by Barouh *et al.* [10] for the Ov pair. The dissociation energy of the Ov pair calculated by the sum of the absolute value of the 1<sup>st</sup> neighbor binding energy and the



oxygen migration energy in pure bcc Fe is about 2.11 eV which is 0.16 eV higher than the activation energy of pair migration. This estimation shows that pair migration is more probable than dissociation.

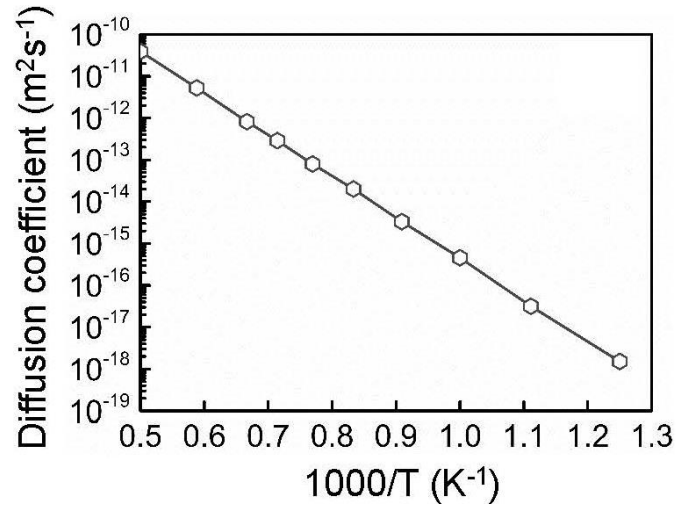


**Figure 5.7** Diffusion coefficient of the Ov pair (inside the interaction region), determined by AKMC simulations, with one mobile oxygen and one mobile vacancy.

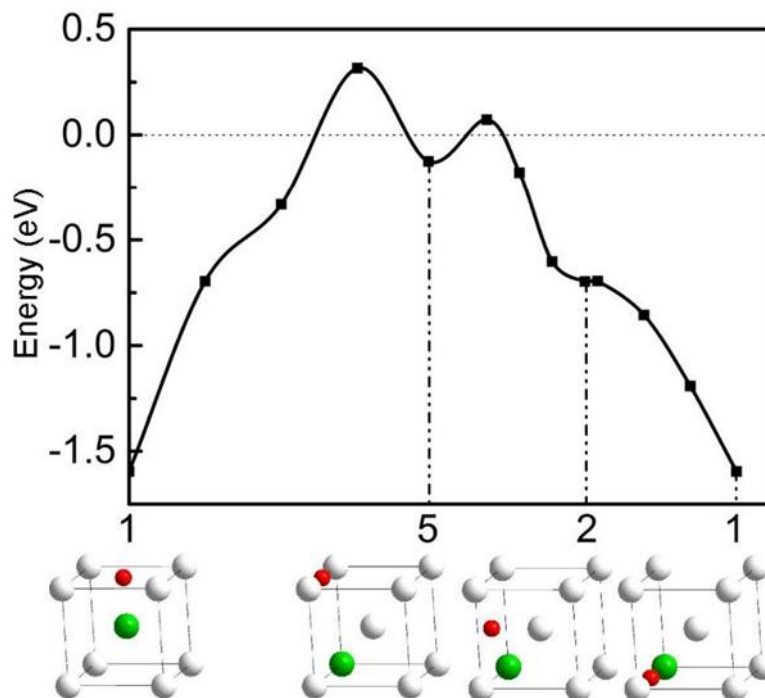


**Figure 5.8** Minimum energy path for the migration of the Ov pair. The scale on the ordinate concerns the binding energy of the Ov pair (see Table 5.1).

## 5.4 Oxygen and vacancy diffusion in the first stage of thermal processing of ODS Fe-based alloys

In the calculation of the data shown in Figs. 5.5, 5.6, and 5.7 constant vacancy and oxygen concentrations are assumed which are still rather low, but much higher than in pure bcc Fe at the thermal equilibrium [5,8-10,67]. A supersaturation of vacancies can occur under extreme conditions, e.g. under irradiation, plastic deformation, and mechanical alloying. The latter method is employed in the production of Oxide Dispersion Strengthened (ODS) Fe-based alloys using powder technology. These materials are considered as promising candidates for structural materials of future fusion and fission reactors [4]. The mechanical alloying or milling process produces a lot of empty volume which may be considered as an additional source of vacancies. Furthermore, it is generally supposed that milling of a mixture containing a Fe-based alloy as well as Ti, and  $Y_2O_3$  leads to a nearly complete dissolution of yttria ( $Y_2O_3$ ) [68,69]. Typical total O, Y, and Ti concentrations ( $C_O^{\text{total}}$ ,  $C_Y^{\text{total}}$ ,  $C_{Ti}^{\text{total}}$ ) are 0.18, 0.12, and 1.05 at%, respectively (MA957 alloy see [68-70]). These data are used in the following considerations. Note, that  $C_O^{\text{total}}$  is much higher than the thermal solubility of oxygen in bcc Fe. The strong attraction between oxygen and the vacancy, between O and Y, and between Y and the vacancy (see below) is assumed to be decisive for the high oxygen and Y incorporation ability of the ODS Fe-based alloys. The thermal processing of the ODS alloy is a complex and time consuming process which includes hot isostatic pressing or hot extrusion, and additional annealing (see e.g. [71-75]). In the following the thermal treatment is described in a very simple manner by assuming equilibrium between O, Y, Ti, and vacancy monomers on the one hand and Ov, vY, vTi, OY, and OTi pairs on the other hand. This may correspond to the first phase of the thermal processing, i.e. to the beginning of the formation of the characteristic ODS clusters which contain O, v, Y and Ti. Any mechanical effects such as pressure and deformation are neglected in these considerations.

If only the most stable pairs:

- Ov at 1<sup>st</sup> neighbor distance ( $E_{\text{bind}} = -1.596$  eV), and at 2<sup>nd</sup> neighbor distance (-0.697 eV),
- OY at 2<sup>nd</sup> neighbor distance (-1.01 eV, see Table 3.1), and at 5<sup>th</sup> neighbor distance (-0.336 eV, see Table 3.1),

- OTi at 1<sup>st</sup> neighbor distance (-0.372 eV (see chapter 3)), and at 2<sup>nd</sup> neighbor distance (-0.593 eV, see Table 3.1 ),
- vY at 3<sup>rd</sup> neighbor distance (-1.26 eV [53]), and
- vTi at 3<sup>rd</sup> neighbor distance (-0.25 eV [52])

are taken into account, the following four equations must be solved to determine the concentrations of O, Y, and Ti monomers,  $C_O$ ,  $C_Y$ , and  $C_{Ti}$ , respectively, and the total vacancy concentration  $C_v^{total}$ . These relations correspond to Lomer's equation [76] and are similar to expressions recently published by Schuler *et al.* [67].

Equation for the total vacancy concentration  $C_v^{total}$ :

$$C_v^{total} = C_v \{1 - A_v + B_v\} \quad (5.8a)$$

with

$$A_v = 6C_O + 8(C_Y + C_{Ti}) \quad (5.8b)$$

$$B_v = 2 \exp\left(-\frac{E_{bind}^1(Ov)}{k_B T}\right) C_O + 4 \exp\left(-\frac{E_{bind}^2(Ov)}{k_B T}\right) C_O + \quad (5.8c)$$

$$8 \exp\left(-\frac{E_{bind}^3(vY)}{k_B T}\right) C_Y + 8 \exp\left(-\frac{E_{bind}^3(vTi)}{k_B T}\right) C_{Ti}$$

Equation for the total oxygen concentration  $C_O^{total}$ :

$$C_O^{total} = C_O \{1 - A_O + B_O\} \quad (5.9a)$$

with

$$A_O = 6C_v + 12C_Y + 6C_{Ti} \quad (5.9b)$$

$$B_O = 2 \exp\left(-\frac{E_{bind}^1(Ov)}{k_B T}\right) C_v + 4 \exp\left(-\frac{E_{bind}^2(Ov)}{k_B T}\right) C_v + 4 \exp\left(-\frac{E_{bind}^2(OY)}{k_B T}\right) C_Y \quad (5.9c)$$

$$+ 8 \exp\left(-\frac{E_{bind}^5(OY)}{k_B T}\right) C_Y + 2 \exp\left(-\frac{E_{bind}^1(OTi)}{k_B T}\right) C_{Ti} + 4 \exp\left(-\frac{E_{bind}^2(OTi)}{k_B T}\right) C_{Ti}$$

Equation for the total Y concentration  $C_Y^{total}$ :

$$C_Y^{\text{total}} = C_Y \{1 - A_Y + B_Y\} \quad (5.10a)$$

with

$$A_Y = 12C_O + 8C_v \quad (5.10b)$$

$$B_Y = 4 \exp\left(-\frac{E_{bind}^2(OY)}{k_B T}\right) C_O + 8 \exp\left(-\frac{E_{bind}^5(OY)}{k_B T}\right) C_O + 8 \exp\left(-\frac{E_{bind}^3(vY)}{k_B T}\right) C_v \quad (5.10c)$$

Equation for the total Ti concentration  $C_{Ti}^{\text{total}}$ :

$$C_{Ti}^{\text{total}} = C_{Ti} \{1 - A_{Ti} + B_{Ti}\} \quad (5.11a)$$

with

$$A_{Ti} = 6C_O + 8C_v \quad (5.11b)$$

$$B_{Ti} = 2 \exp\left(-\frac{E_{bind}^1(OTi)}{k_B T}\right) C_O + 4 \exp\left(-\frac{E_{bind}^2(OTi)}{k_B T}\right) C_O + 8 \exp\left(-\frac{E_{bind}^3(vTi)}{k_B T}\right) C_v \quad (5.11c)$$

$E_{bind}^3(vY)$  and  $E_{bind}^3(vTi)$  denote binding energies at the 1<sup>st</sup> neighbor distance of the bcc lattice which corresponds to the 3<sup>rd</sup> neighbor distance in the underlying simple cubic lattice. Note that in bcc Fe the interaction between Y and Ti is repulsive and is therefore not considered in Eqs. (5.8)-(5.11) [77]. In these equations, the quantity  $B$  times the corresponding monomer concentration characterizes the concentration of the considered species (O, v, Y, Ti) within pairs. The quantity  $1 - A$  times the corresponding monomer concentration characterizes the concentration of the species which are not in pairs.

It must be mentioned that the thermodynamic approach given in Eqs. (5.8)-(5.11) can be considered as a cluster expansion truncated after the pair term. A more general method which allows the consideration of larger cluster was developed recently by other authors [47,67,78].

In the thermal equilibrium the concentration of single vacancies (monomers) is given by

$$C_v = \exp\left(\frac{-E_F^f}{k_B T}\right) \quad (5.12)$$

if only the vacancy formation energy at the (ferromagnetic) ground state  $E_F^f$  is taken into account. This is consistent with Eqs. (5.8-5.11) where ground state binding energies are used. At elevated temperature the ground state quantities should be replaced by free formation and binding energies. In the present work only the phonon and magnetic contributions to the free formation energy of the vacancy  $F^f$  are considered. According to Schuler *et al.* [67]  $F^f$  is determined by

$$F^f(T) = E_P^f + (E_F^f - E_P^f)M_0(T)^2 - T\left[S_P^f + (S_F^f - S_P^f)M_0(T)^2\right] \quad (5.13)$$

where  $E_F^f$ ,  $S_F^f$  and  $E_P^f$ ,  $S_P^f$  are the formation energy and entropy in ferromagnetic and paramagnetic bcc Fe, respectively, with  $E_F^f = 2.12$  eV,  $E_P^f = 1.98$  eV,  $S_F^f \approx 5k_B$  and  $S_P^f \approx 4k_B$  [67]. The quantity  $M_0(T)$  denotes the reduced magnetization which varies between 1 (ferromagnetic ground state) and 0 (full paramagnetic state). For  $M_0(T)$  the experimental data of Crangle *et al.* [79] are used. Using  $F^f$  the monomer vacancy concentration can be calculated by

$$C_v = \exp\left(\frac{-F^f}{k_B T}\right) \quad (5.14)$$

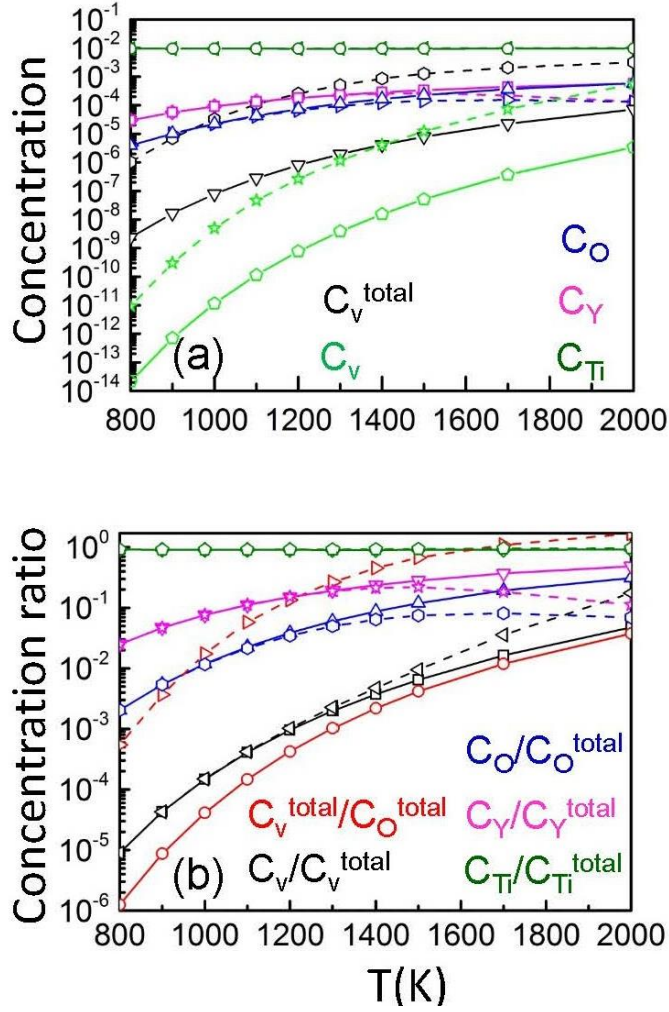


**Figure 5.9** Temperature dependence of monomer concentrations  $C_v$ ,  $C_O$ ,  $C_Y$ ,  $C_{Ti}$ , and of the total vacancy concentration (a) as well as the concentration ratios vs. temperature (b). The data were obtained by the solution of Eqs. (5.8)-(5.11), for the following total concentrations of solutes: 0.18 at% (O), 0.12 at% (Y), and 1.05 at% (Ti). The solid and dashed lines were determined using from Eqs. (5.12) and (5.14), respectively. The scale on the ordinate of figure (a) shows not at% but the dimensionless concentration (normalized to 1).

The solutions of Eqs. (5.8)-(5.11) with  $C_v$  from (5.12) or (5.14) are shown in Fig. 5.9. The temperature dependence of the monomer concentrations and of  $C_v^{total}$  is illustrated in Fig. 5.9 (a). The difference between the data for  $C_v^{total}$  obtained using  $C_v$  from (5.12) or (5.14) is significant. In Fig. 5.9 (b) the ratios  $C_v/C_v^{total}$ ,  $C_v^{total}/C_O^{total}$ ,  $C_O/C_O^{total}$ ,  $C_Y/C_Y^{total}$ , and  $C_{Ti}/C_{Ti}^{total}$  are depicted. This figure clearly shows that most of

the vacancies and most of the O and Y atoms are bound in the corresponding pairs. At very high temperature the values of  $C_v / C_v^{\text{total}}$ ,  $C_O / C_O^{\text{total}}$  and  $C_Y / C_Y^{\text{total}}$  obtained using  $C_v$  from Eq. (5.14) deviate from those calculated using  $C_v$  from Eq. (5.12), [difference between dashed and solid line in Fig. 5.9 (b)]. However, these temperatures are not of practical relevance for the thermal processing of ODS alloys. At lower temperature the three ratios show an increase. Furthermore,  $C_{\text{Ti}} / C_{\text{Ti}}^{\text{total}}$  is close to one, which means that most of the Ti atoms are not bound in pairs. This is due to fact that  $C_{\text{Ti}}^{\text{total}}$  is higher than  $C_O^{\text{total}}$ ,  $C_Y^{\text{total}}$ , and  $C_v^{\text{total}}$ , and that the attraction between Ti and the other species is relatively weak. The ratios  $C_v^{\text{total}} / C_O^{\text{total}}$  calculated using  $C_v$  from Eqs. (5.12) or (5.14) are very different since  $C_v$  determined by Eq. (5.14) is significantly higher. However, in both cases the ratio is much less than one. This does not agree with the assumption made by several authors [80-82] that in the production of ODS alloys the total vacancy concentration can reach the same order of magnitude as the total concentration of oxygen. On the other hand, it must be emphasized that the data of Fig. 5.9 were determined under the assumption of the equilibrium between monomers and pairs. Including larger clusters containing O, vacancies, Y, and Ti (see e.g. [83]) may change the ratio  $C_v^{\text{total}} / C_O^{\text{total}}$  and the other results. In this case equations similar to (5.8c)-(5.11c) would contain additional terms with concentrations of the clusters and binding energies of the monomers to the cluster. Furthermore, it must be noticed that above considerations assume a compact Fe-based material containing a given amount of foreign atoms, and the total vacancy concentration is established by the thermal equilibrium. In reality at the beginning of the thermal treatment of ODS alloys the material is not compact but more similar to a powder. Therefore, there are certainly additional sources of vacancies so that their concentration should be higher than in a compact material. Thus the data depicted in Fig. 5.9 (b) should be regarded as a lower limit for  $C_v^{\text{total}} / C_O^{\text{total}}$ .

In the following the diffusion coefficient of oxygen is calculated for the dilute iron alloy using (i) the monomer concentrations  $C_v$ ,  $C_Y$ , and  $C_{\text{Ti}}$  shown in Fig. 5.9 (a), or (ii) the total concentrations  $C_v^{\text{total}}$ ,  $C_Y^{\text{total}}$ , and  $C_{\text{Ti}}^{\text{total}}$  given in the above text or depicted in Fig. 5.9 (a) ( $C_v^{\text{total}}$ ). The reason why total concentrations are considered is discussed

below. The oxygen diffusion coefficient is determined using expressions similar to Eqs. (5.3) and (5.5), but considering interactions not only with v but also with Y and Ti

$$D = \frac{t_{free}}{t_{total}} D_{free} + \frac{t_{inter,v}}{t_{total}} D_{inter,v} + \frac{t_{inter,Y}}{t_{total}} D_{inter,Y} + \frac{t_{inter,Ti}}{t_{total}} D_{inter,Ti} \quad (5.15a)$$

$$t_{total} = t_{free} + t_{inter,v} + t_{inter,Y} + t_{inter,Ti} \quad (5.15b)$$

and

$$\frac{t_{free}}{t_{total}} = \frac{1 - R_1}{R} \quad (5.16a)$$

$$\frac{t_{inter,v}}{t_{total}} = \frac{\sum_i N_i \exp\left(-\frac{E_{bind}^i(Ov)}{k_B T}\right) C_v^*}{R} \quad (5.16b)$$

$$\frac{t_{inter,Y}}{t_{total}} = \frac{\sum_j N_j \exp\left(-\frac{E_{bind}^j(OY)}{k_B T}\right) C_Y^*}{R} \quad (5.16c)$$

$$\frac{t_{inter,Ti}}{t_{total}} = \frac{\sum_k N_k \exp\left(-\frac{E_{bind}^k(OTi)}{k_B T}\right) C_{Ti}^*}{R} \quad (5.16d)$$

$$R_1 = \sum_i N_i C_v^* + \sum_j N_j C_Y^* + \sum_k N_k C_{Ti}^* \quad (5.16e)$$

$$R_2 = \sum_i N_i \exp\left(-\frac{E_{bind}^i(Ov)}{k_B T}\right) C_v^* + \sum_j N_j \exp\left(-\frac{E_{bind}^j(OY)}{k_B T}\right) C_Y^* + \sum_k N_k \exp\left(-\frac{E_{bind}^k(OTi)}{k_B T}\right) C_{Ti}^* \quad (5.16f)$$

$$R = 1 - R_1 + R_2 \quad (5.16g)$$

The data for  $D_{inter,Y}$  and  $D_{inter,Ti}$  are calculated by AKMC simulations similarly to the determination of  $D_{inter,v}$ . As in the determination of concentrations by Eqs. (5.8)-(5.14), only the most attractive O-v, O-Y, and O-Ti interactions are taken into account in Eqs. (5.16). The star superscript indicates that monomer *or* total concentrations are used in two separate types of calculations as already mentioned above. At first the diffusion coefficient is determined using the monomer concentrations  $C_v$ ,  $C_Y$ , and  $C_{Ti}$ . In reality



the diffusion of oxygen may be not only influenced by the v, Y, and Ti monomers but also by pairs or larger cluster which may contain v, Y, or Ti. In very simple approximation the total concentrations  $C_v^{\text{total}}$ ,  $C_Y^{\text{total}}$ , and  $C_{\text{Ti}}^{\text{total}}$  may be used instead of the monomer concentrations. This is not quite correct since neither the binding energy of an oxygen atom with pairs or larger clusters nor the migration barriers of oxygen in their environment is equal to those in the case of monomers. On the other hand, the calculation of the corresponding binding energies and migration barriers by DFT is an extensive task since many different cluster configurations must be considered. In order to get an idea about the influence of the clusters calculations are therefore performed using  $C_v^{\text{total}}$ ,  $C_Y^{\text{total}}$ , and  $C_{\text{Ti}}^{\text{total}}$ .

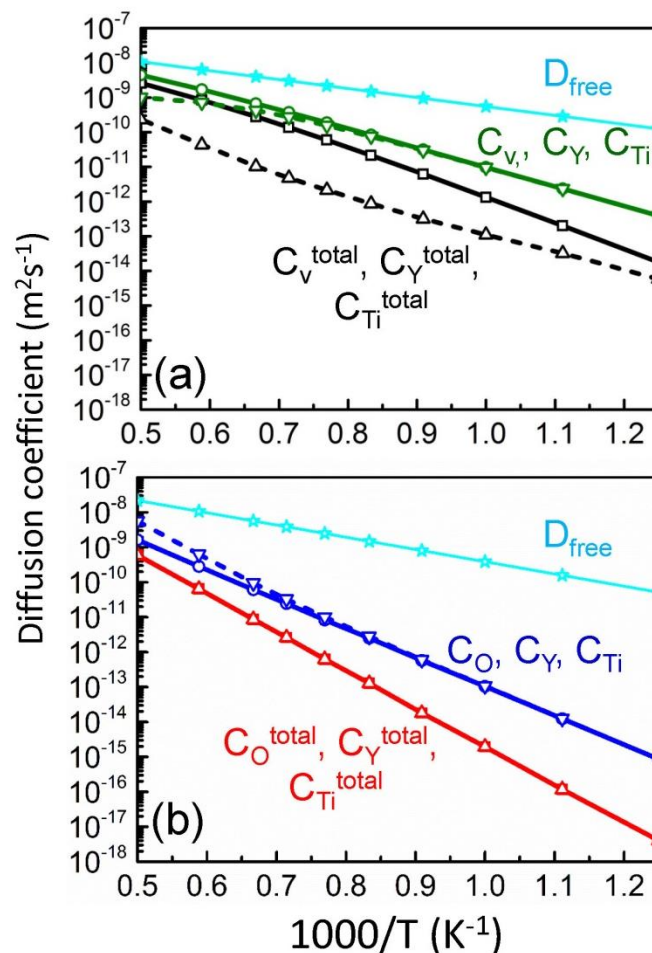


**Figure 5.10** Total diffusion coefficients of O (a) and v (b) determined for the monomer or the total concentrations shown in Fig. 5.9 (a) and given in the text. The concentrations used in the calculations are written close to the corresponding curves

for the diffusion coefficient using the same color. These curves were either obtained using  $C_v$  from Eq. (5.12) (solid lines) or  $C_v$  from Eq. (5.14) (dashed lines).

Fig. 5.10 (a) depicts the results for the O diffusion. If only the monomer concentrations  $C_v$ ,  $C_Y$ , and  $C_{Ti}$  are taken into account the diffusion coefficient is already significantly lower than that in pure Fe. The use of either Eq. (5.12) or Eq. (5.14) for  $C_v$  affects the result only at very high temperatures which are not of practical relevance. Below the bcc-to-fcc transition temperature of 1183 K the effective diffusion activation energy is about 1.1 eV. On the other hand, the use of total concentrations  $C_v^{total}$ ,  $C_Y^{total}$ , and  $C_{Ti}^{total}$  in Eqs. (5.16) leads to an O diffusion coefficient which is still lower than that obtained by considering the monomer concentrations. A large difference is obtained between the results determined using  $C_v$  from Eq. (5.12) or Eq. (5.14). The latter case leads to the lowest oxygen diffusion coefficient. This can be explained by the fact that  $C_v^{total}$  is significantly higher than  $C_v$  [see Fig. 5.9 (a)]. With  $C_v$  from Eq. (5.12) or Eq. (5.14) the diffusion activation energy is about 1.5 or 1.0 eV, respectively, in the temperature range of bcc Fe. The influence of the substitutional foreign atoms on the O diffusion coefficient becomes obvious by comparing with data shown in Fig. 3.5 (Chapter 3), and in Fig. 5.6 (a), and by considering the concentrations shown in Fig. 5.9 (a): For example, at low temperature the black dashed curve in Fig. 5.10 (a) should be determined by the total concentration of Y (0.12 at%) and/or Ti (1.05 at%) since the total v concentration is extremely low. Comparison with diagrams shown in Figs. 3.5 (e) and (i) of Chapter 3 clearly shows that the Y content dominates the value of the O diffusion coefficient at temperatures around 800 K. On the other hand, at temperatures near 2000 K the v content is in the order of some tenth of percent [black dashed line in Fig. 5.9 (a)] and therefore determines the value of the O diffusion coefficient, as one can see by comparing with Fig. 5.6 (a). A similar discussion could be performed concerning the other curves depicted in Fig. 5.10 (a).

Vacancy diffusion in the alloy containing O, Y, and Ti was treated using a method similar to that employed in the calculation of the oxygen diffusion coefficient. The results are shown in Fig. 5.10 (b). The following cases were considered: (i) Only the monomer concentrations  $C_O$ ,  $C_Y$ , and  $C_{Ti}$  [see Fig. 5.9 (a)] were taken into account. (ii) The (constant) total concentrations  $C_O^{total}$ ,  $C_Y^{total}$ , and  $C_{Ti}^{total}$  (data given above) were

used. Since the monomer concentrations of O, Y, and Ti determined either using Eqs. (5.12) or (5.14) for  $C_v$  are nearly equal, see Fig. 5.9 (a), the resulting values for  $v$  diffusion are also not very different. The corresponding diffusion activation energy is about 1.6 eV (below 1183 K). On the other hand, in the calculation of the  $v$  diffusivity for the constant total concentrations of O, Y, and Ti the quantity  $C_v$  need not to be used at all. In the latter case, at 800 K the  $v$  diffusion coefficient is about seven orders of magnitude lower than that in perfect bcc Fe, and the activation energy is about 2.13 eV. The comparison of the red line in Fig. 5.10 (b) with the green curve in Fig. 5.6 (b) reveals that the given total O concentration dominates the  $v$  diffusion coefficient over the whole temperature range. Thus the influence of Y and Ti is negligible which is due to the weaker binding between  $v$  and Y as well as  $v$  and Ti compared to that between  $v$  and O. Similarly, the blue curves in Fig. 5.10 (b) should be mainly determined by the monomer O concentration.

### **5.5 Oxygen and vacancy diffusion in bcc Fe with an oxygen content close to the value of thermal solubility**

The few experimental data on oxygen solubility in bcc Fe were published many years ago [5,7,10] and were derived from measurements and calculations performed in connection with internal oxidation experiments. In the temperature range between 800 and 1043 K the data obtained from the formula of Takada *et al.* [10] differ to those of Frank *et al.* [5] by up to one order of magnitude. The value of Swisher *et al.* [7] lies between these data sets (see Appendix IV). In the present work the solubility data of Takada *et al.* [10] are used. Furthermore, Murali *et al.* [48] calculated by DFT the free formation energy of oxygen by considering equilibrium between Fe and FeO. In the ferromagnetic temperature range the oxygen concentration obtained from these theoretical solubility data is somewhat higher than that of Takada *et al.* [10] (see Appendix IV).

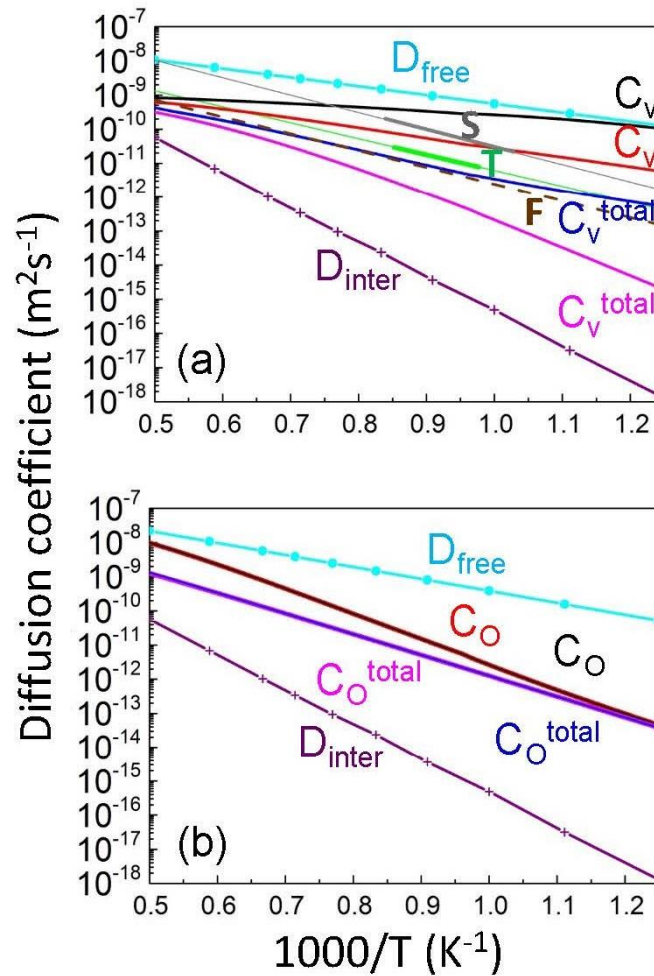


**Figure 5.11** Total diffusion coefficients of O (a) and v (b) for the case that the oxygen concentration is equal to the thermal solubility. The black and blue curves were determined using monomer and total concentrations, respectively, for O and v. These concentrations were calculated by the method according to sections 5.3 and 5.4. The red and magenta curves were obtained by a modified procedure where not only the O-v interaction but also the O-Ov (or v-Ov) interactions are taken into account (see Appendix V). The red and magenta curves were calculated for monomer and total v or O concentrations, respectively. Note that in (b) the blue and the magenta curves as well as the black and red curves are nearly identical. The oxygen diffusion data determined by internal oxidation experiments are marked by S [7], T [8-10], and F [5]. In the case of S and T the thick lines show the temperature range in which the measurements were performed. Note that the data of Swisher *et al.* [7] are based on permeability measurements for  $\delta$  iron [6] and are therefore only approximately valid for bcc Fe. The brown dashed line was obtained using the

activation energy given by Frank *et al.* [5] and the pre-exponential factor from Eq. (5.4).

At first the formalism of sections 5.3 or 5.4 is employed. The oxygen solubility is set equal to  $C_O^{\text{total}}$ , and  $C_v$  is calculated by Eq. (5.14). In this manner the monomer O concentration  $C_O$ , the total vacancy concentration  $C_v^{\text{total}}$  and other quantities are determined (see also Appendix V). Since both the oxygen and the vacancy concentration are rather low, Eq. (5.6) can be employed to determine the oxygen diffusion coefficient. A similar relation is used for the vacancy diffusivity. The results obtained by this method are depicted in Fig. 5.11. If the monomer vacancy concentration  $C_v$  is used in an expression similar to Eq. (5.16a), the oxygen diffusion coefficient is lower than that for pure bcc Fe but shows a relatively weak temperature dependence [Fig. 5.11 (a)]. This is due to the fact that the value of the free formation energy of the vacancy according to Eq. (5.13) is not very different to the absolute value of the binding energy of the Ov pair. This may lead to a slight increase of the time ratio  $t_{\text{free}} / t_{\text{total}}$  with decreasing temperature while  $D_{\text{free}}$  decrease. This peculiarity does not happen if the total vacancy concentration  $C_v^{\text{total}}$  is used instead of  $C_v$ . In this case the oxygen diffusion coefficient is somewhat more similar to the measured data although significant differences remain. The motivation for using the total instead of monomer concentrations was discussed in previous section 5.4. On the other hand, Fig. 5.11 (a) clearly shows the discrepancy between the experimental data of Swisher *et al.* [7] and Takada *et al.* [8-10]. This underlines the need for new experimental diffusion data directly obtained from an oxygen concentration profile in a sufficiently pure and defect-free bcc Fe. Using the pre-exponential factor from Eq. (5.4) and the diffusion activation energy of Frank *et al.* [5] (0.98 eV) another “quasi- experimental” data set was obtained [see Fig. 5.11 (a)].

Schuler *et al.* [67] demonstrated that in the case of bcc Fe with an oxygen content equal to the thermal solubility, not only the Ov pair but also O<sub>2</sub>v are important in the determination of the total vacancy concentration. Following Ref. [67], in the present work the formalism of sections 5.3 or 5.4 was extended so that and not only Ov, but also O<sub>2</sub>v and Ov<sub>2</sub> are considered (Appendix V), with binding energies  $E_{\text{bind}}^{\text{O}_2\text{v}} = -3.349$  eV and  $E_{\text{bind}}^{\text{Ov}_2} = -2.502$  eV. That means it is assumed that during O migration not only the

Ov pair but also the O<sub>2</sub>v cluster may be formed temporarily. Similar to the case without O<sub>2</sub>v, calculations were performed assuming  $C_v$  or  $C_v^{\text{total}}$  for the vacancy concentration. In both cases the diffusion activation energy which determines the slope of the curves [red and magenta curves in Fig. 5.11 (a)] is higher than for the respective curves obtained without considering O<sub>2</sub>v. Fig. 5.11 (b) shows the vacancy diffusion coefficient under the influence of oxygen. Assuming the monomer concentration  $C_o$  in a relation similar to Eq. (5.16a) leads to a somewhat higher diffusion activation energy than using  $C_o^{\text{total}}$ . In both cases the vacancy diffusion coefficient is much lower than that in pure bcc Fe. Taking into account that during v migration not only Ov but also Ov<sub>2</sub> may be formed temporarily does not change the results since in thermal equilibrium the concentration of Ov<sub>2</sub> is very small (see Appendix V). The results presented in this section demonstrate that the presence of a very small amount of oxygen, in the order of the thermal solubility, have a significant influence on both O and v diffusion.

## 5.6 Summary and conclusions

The mutual dependence of O and v diffusion in bcc Fe and dilute iron alloys was investigated using a combined computational method. DFT calculations of the binding energy between O and v at different distances and of the migration barriers of O and v in the regions of their interaction revealed significant special features. The finding of an extremely strong binding of the Ov pair at the first neighbor distance and of the very high barrier to be overcome for leaving this state are consistent with previous work. On the other hand, it was shown that the Ov pair at the 6<sup>th</sup> neighbor distance is unstable. This would lower the number of possible migration paths for O and v in the interaction region. However, this reduction is compensated by the newly found simultaneous or coupled jumps of O and v. Furthermore, the investigations showed that a direct v jump from the 2<sup>nd</sup> to the 5<sup>th</sup> neighbor distance to O is not possible. Ultimately, these peculiarities are due to the very strong attractive interaction of the Ov pair at the 1<sup>st</sup> neighbor state. The DFT results were used as inputs for AKMC-based calculations of the diffusion coefficients of O and v. The consideration of a model system with fixed v or O concentrations already demonstrated the strong influence of vacancies on O diffusion and of oxygen on v diffusion, leading to a significant decrease of the corresponding diffusion coefficients, even if the concentrations are only in the order of some ppm. As a more realistic case, the diffusion of O and v during the first stage of

thermal processing of ODS alloys was investigated. This system contains ODS-typical total concentrations of O, Y, and Ti. In a simple model thermal equilibrium between O, v, Y, and Ti monomers on the one hand and Ov, OY, OTi, vY, and vTi pairs on the other hand was assumed. Then the O, Y, and Ti monomer concentrations as well as the total v concentration were determined. The O diffusion coefficients obtained for monomer or total concentrations show a significant dependence on the vacancy and the Y content, whereas the v diffusivity is only influenced by the presence of oxygen. Furthermore, a system with an O content close to the thermal solubility in iron was studied. The monomer O concentration as well as the total v concentration was determined using two different models considering equilibrium of O and v with Ov, or equilibrium of O and v with Ov and O<sub>2</sub>v or Ov<sub>2</sub>. Despite the very small value of thermal solubility of O in bcc Fe, both the O and v diffusion coefficient are very different from that in pure iron. These findings also show that not only the total v concentration or the effective v formation energy is strongly affected by the very small O content, as found by Schuler *et al.* [67], but also the diffusion coefficients of v and O and the corresponding effective diffusion activation energies.

## Chapter 6: Summary, conclusions and outlook

In this dissertation, diffusion of oxygen (O) and the vacancy (v) in dilute bcc-iron-based alloys was studied by a combination of Density Functional Theory (DFT) and Atomistic Kinetic Monte Carlo (AKMC) simulations. In particular, the effect of substitutional atoms on oxygen diffusion, the mutual influence of vacancy and oxygen diffusion as well as the influence of substitutional atoms on vacancy diffusion was investigated.

### Migration mechanisms of O and v in perfect bcc Fe

- The most relevant jump of O is that between two first-neighbor octahedral interstitial sites, with a linear migration path, and the tetrahedral interstitial site as the saddle point. A second-neighbor jump consists of two successive first-neighbor jumps. The third-neighbor O jump has a nonlinear migration path and the saddle point corresponds to a rhombohedral interstitial site, but the barrier for such a direct jump is too high to be relevant for O diffusion.
- The vacancy jumps from one bcc site to the neighboring site on a straight path. At the saddle point the migrating Fe atom is at the middle between the neighboring bcc sites. Vacancy migration over longer distances always consist of successive first-neighbor jumps.

### Migration of oxygen in environment of substitutional atoms (Al, Si, P, S, Ti, Cr, Mn, Ni, Y, Mo, and W)

- The migration mechanism is rather similar to that in pure bcc Fe, i.e. the most relevant O jump occurs from a modified octahedral site via a modified tetrahedral site to another modified octahedral site. The migration barriers in the environment of Si, P, Ni, Mo and W are not very different to that in pure Fe, with the exception of a high barrier close to the substitutional atom. The interaction of these solutes with oxygen is mainly repulsive. Al, S, Ti, Cr, Mn and Y have strong attractive interaction with oxygen, associated with large barriers for escape from neighbor shells close to the solutes, while the migration barriers for approaching these solutes are relatively low.
- The oxygen diffusion coefficient was determined for dilute alloys with concentrations of substitutional atoms up to 0.781 at%. The influence of Si, P, Ni, Mo, and W on O diffusion is very small. Al, S, Ti, Cr, Mn and Y cause



considerable reduction of the oxygen mobility. The reason for this behavior is the so-called trapping mechanism due to the attractive interaction between the substitutional solute and O. The influence of Al, Cr, Mn, S, Ti, and Y leads to deviations from the Arrhenius behavior of the oxygen diffusion coefficient. This can be explained by the significant temperature dependence of the occupation time for the different states. In all cases investigated the oxygen diffusion coefficient was still some orders of magnitude higher than that of the corresponding substitutional solute. Therefore, the initial assumption that the substitutional solute can be considered to be immobile in the calculation of the O diffusion coefficient is justified.

### **Efficient AKMC-based calculation method for the diffusion coefficient of interstitial atoms in dilute alloys**

- The calculation procedure is based on the separation of the diffusion path into a contribution related to migration in the interaction region between the mobile interstitial and the substitutional solute and another part related to diffusion in perfect bcc Fe. In this manner AKMC simulation must be performed only for one concentration of the substitutional solute, and the obtained results can be employed to determine data for other concentrations using analytical expressions containing binding energies between the interstitial and the substitutional solute. This leads to a tremendous decrease of computational efforts. For sufficiently low concentrations of solutes, it is even possible to use an analytical expression where only the diffusion coefficient of the interstitial atom in perfect bcc Fe and binding energies are needed. In this work the developed efficient method is not only applied to investigate the effect of substitutional atoms on O diffusion, but a corresponding scheme is also used to determine the vacancy diffusion coefficient under the influence of oxygen and substitutional atoms (see below).

### **Mutual influence of O and v**

- The Ov pair has an extremely strong binding at the 1<sup>st</sup> neighbor distance and is unstable at the 6<sup>th</sup> neighbor distance. These peculiarities affect possible migration paths for O and v in the interaction region and might lead to the reduction of the number of conventional migration paths consisting of separate O and v jumps between neighboring octahedral and bcc lattice sites, respectively.

The newly found simultaneous or coupled jumps of both O and v compensate the absence of separate O and v jumps from and to the 6<sup>th</sup> neighbor site.

### **Influence of vacancy on oxygen diffusion and of oxygen on vacancy diffusion in a model system with fixed O and v concentration**

- Using the efficient AKMC-based method outlined above, a significant decrease of the diffusion coefficient of oxygen is observed due to the presence of v, even if the v concentration is in the order of some ppm. A similar effect is obtained for v diffusion under the influence of oxygen.

### **Diffusion of oxygen and vacancy in the first stage of thermal processing of Oxygen Dispersion Strengthened (ODS) steels**

- An alloy containing ODS-typical total concentrations of O, v, Y and Ti was described in a simple manner assuming thermal equilibrium between O, Y, Ti and vacancy monomers on the one hand, and Ov, vY, vTi, OY, and OTi pairs on the other hand. Then the O, Y, and Ti monomer concentrations as well as the total v concentration were determined and the AKMC-based method was employed to determine O and v diffusion coefficients. The oxygen diffusion coefficient shows a significant dependence on v and Y, while the diffusivity of vacancy is only influenced by oxygen.

### **Oxygen and vacancy diffusion in bcc Fe with oxygen concentration close to the value of thermal solubility**

- The monomer O concentration and the total v concentration were determined using two different thermodynamic models. In the first case, thermal equilibrium of O and v monomers with Ov was taken into account, and in the second case equilibrium of O and v with Ov, O<sub>2</sub>v, and Ov<sub>2</sub> was considered. The total O concentration was set equal to the thermal solubility. Despite the very small value of thermal solubility of O in bcc Fe, both the O and v diffusion coefficient are very different from that in pure iron. These findings also show that not only the total v concentration or the effective v formation energy is strongly affected by the very small O content, as found by Schuler *et al.* [67], but also the diffusion coefficients of v and O, and the corresponding effective diffusion activation energies.

The results of the present work have important consequences for planning and performing experiments on O and v diffusion in dilute iron alloys. In particular, a very precise knowledge of the concentrations of O and v, as well as of other foreign atoms and traps such as dislocations is required. It is also recommended to use bcc Fe single crystals in order to avoid the influence of grain boundaries in such fundamental experiments. The results of the present work are comprehensive and contribute to providing new insight into the interplay between different atomic species and defects in complex materials. Theoretical methods similar to those used in this PhD Thesis may be employed in future studies of diffusion in various crystalline solids, with focus on the influence of substitutional atoms or dopants on the diffusion of foreign interstitial atoms, vacancies and self-interstitial atoms, as well as on (ii) the mutual influence of diffusion of intrinsic point defects and interstitial atoms.

## References:

- [1] H. Mehrer, N. Stolica, and N. A. Stolwijk, in *Diffusion in Solid Metals and Alloys*, edited by H. Mehrer (Springer, Berlin, 1990).
- [2] C. S. Becquart and C. Domain, Introducing chemistry in atomistic kinetic Monte Carlo simulations of Fe alloys under irradiation, *Phys. Status Solidi B* 247, 9 (2010).
- [3] L. Messina, N. Castin, C. Domain, and P. Olsson, Introducing ab initio based neural networks for transition-rate prediction in kinetic Monte Carlo simulations, *Phys. Rev. B* 95, 064112 (2017).
- [4] G. R. Odette, Recent Progress in Developing and Qualifying Nanostructured Ferritic Alloys for Advanced Fission and Fusion Applications, *Jom* 66, 2427 (2014).
- [5] W. Frank, H. J. Engell, and A. Seeger, Migration energy and solubility of oxygen in body centered cubic iron, *Z. Metallkd.* 58, 452 (1967).
- [6] M. T. Hepworth, R. P. Smith, and E. T. Turkdogan, Permeability, solubility, and diffusivity of oxygen in bcc iron, *Aime Met. Soc. Trans.* 236, 1278 (1966).
- [7] J. H. Swisher and E. T. Turkdogan, Solubility, permeability, and diffusivity of oxygen in solid iron, *Trans. Met. Soc. AIME* 426, 239 (1967).
- [8] J. Takada and M. Adachi, Determination of diffusion coefficient of oxygen in  $\alpha$ -iron from internal oxidation measurements in Fe-Si alloys, *J. Mater. Sci.* 21, 2133 (1986).
- [9] J. Takada, S. Yamamoto, S. Kikuchi, and M. Adachi, Internal oxidation of Fe-Al alloys in the  $\alpha$ -phase region *Oxid. Met* 25, 93 (1986).
- [10] J. Takada, S. Yamamoto, and M. Adachi, Diffusion coefficient of oxygen in  $\alpha$ -iron determined by internal oxidation technique, *Z. Metallkd.* 77, 6 (1986).
- [11] A. Seeger, Lattice Vacancies in High-Purity  $\alpha$ -Iron, *physica status solidi (a)* 167, 289 (1998).
- [12] N. Hashimoto, S. Sakuraya, J. Tanimoto, and S. Ohnuki, Effect of impurities on vacancy migration energy in Fe-based alloys, *J. Nucl. Mater.* 445, 224 (2014).
- [13] D. Simonovic, C. K. Ande, A. L. Duff, F. Syahputra, and M. H. F. Sluiter, Diffusion of carbon in bcc Fe in the presence of Si, *Phys. Rev. B* 81, 054116 (2010).
- [14] P. Liu, W. Xing, X. Cheng, D. Li, Y. Li, and X.-Q. Chen, Effects of dilute substitutional solutes on interstitial carbon in  $\alpha$ -Fe: Interactions and associated carbon diffusion from first-principles calculations, *Phys. Rev. B* 90, 024103 (2014).
- [15] C. Barouh, T. Schuler, C. C. Fu, and T. Jourdan, Predicting vacancy-mediated diffusion of interstitial solutes in  $\alpha$ -Fe, *Phys. Rev. B* 92, 104102 (2015).
- [16] S. L. Shang, H. Z. Fang, J. Wang, C. P. Guo, Y. Wang, P. D. Jablonski, Y. Du, and Z. K. Liu, Vacancy mechanism of oxygen diffusivity in bcc Fe: A first-principles study, *Corr. Sci.* 83, 94 (2014).
- [17] C. J. Ortiz, M. J. Caturla, C. C. Fu, and F. Willaime, Influence of carbon on the kinetics of He migration and clustering in  $\alpha$ -Fe from first principles, *Phys. Rev. B* 80 (2009).

- [18] D. Sholl, and Janice A. Steckel., Density functional theory-a practical introduction (John Wiley & Sons, 2011).
- [19] R. M. Martin, Electronic structure: basic theory and practical methods. (Cambridge university press, 2004).
- [20] Lecture of Prof. H. Sormann (2012), 8. Kapitel: Hartree-Fock Verfahren / Grundlagen Dichtefunktional-Theorie (leicht gekürzt), Technische Universität Graz.
- [21] P. Hohenberg and W. Kohn, Inhomogeneous Electron Gas, Physical Review 136, B864 (1964).
- [22] W. Kohn and L. J. Sham, Self-Consistent Equations Including Exchange and Correlation Effects, Physical Review 140, A1133 (1965).
- [23] J. P. Perdew and Y. Wang, Accurate and simple analytic representation of the electron-gas correlation energy, Phys Rev B Condens Matter 45, 13244 (1992).
- [24] J. P. Perdew, K. Burke, and M. Ernzerhof, Generalized Gradient Approximation Made Simple, Phys. Rev. Lett. 77, 3865 (1996).
- [25] G. Kresse and J. Hafner, Ab initio molecular dynamics for liquid metals, Phys. Rev. B 47, 558 (1993).
- [26] G. Kresse and J. Furthmüller, Efficient iterative schemes for ab initio total-energy calculations using a plane-wave basis set, Phys. Rev. B 54, 11169 (1996).
- [27] G. Kresse and J. Furthmüller, Efficiency of ab-initio total energy calculations for metals and semiconductors using a plane-wave basis set, Comput. Mater. Sci. 6, 15 (1996).
- [28] D. Vanderbilt, Soft self-consistent pseudopotentials in a generalized eigenvalue formalism, Phys Rev B Condens Matter 41, 7892 (1990).
- [29] P. E. Blöchl, Projector augmented-wave method, Phys. Rev. B 50, 17953 (1994).
- [30] G. Kresse and D. Joubert, From ultrasoft pseudopotentials to the projector augmented-wave method, Phys. Rev. B 59, 1758 (1999).
- [31] H. J. Monkhorst and J. D. Pack, Special points for Brillouin-zone integrations, Phys. Rev. B 13, 5188 (1976).
- [32] G. H. Vineyard, Frequency factors and isotope effects in solid state rate processes, J. Phys. Chem. Solids 3, 121 (1957).
- [33] A. F. Voter, Introduction to the kinetic Monte Carlo method (Springer, Dordrecht, 2007), Radiation Effects in Solids, p.^pp. 1-23.
- [34] H. Jonsson, G. Mills, and K. W. Jacobsen, Classical and quantum dynamics in condensed phase simulations (World Scientific, Singapore, New Jersey, London, Hongkong, 1998), p.^pp. 389-404.
- [35] G. Henkelman, B. P. Uberuaga, and H. Jonsson, A climbing image nudged elastic band method for finding saddle points and minimum energy paths, J. Chem. Phys. 113 (2000).
- [36] <http://theory.cm.utexas.edu/vtsttools>.

- [37] L. Messina, Multiscale modeling of atomic transport phenomena in ferritic steels, PhD thesis, 2015.
- [38] L. T. Kong and L. J. Lewis, Transition state theory of the preexponential factors for self-diffusion on Cu, Ag, and Ni surfaces, *Phys. Rev. B* 74, 073412 (2006).
- [39] M. W. Guinan, R. N. Stuart, and R. J. Borg, Fully dynamic computer simulation of self-interstitial diffusion in tungsten, *Phys. Rev. B* 15 (1977).
- [40] M. Posselt, F. Gao, and D. Zwicker, Atomistic study of the migration of di- and tri-interstitials in silicon, *Phys. Rev. B* 71, 245202 (2005).
- [41] N. Anento, A. Serra, and Y. Osetsky, Effect of nickel on point defects diffusion in Fe – Ni alloys, *Acta Mater.* 132, 367 (2017).
- [42] C. L. Fu, M. Krcmar, G. S. Painter, and X. Q. Chen, Vacancy mechanism of high oxygen solubility and nucleation of stable oxygen-enriched clusters in Fe, *Phys. Rev. Lett.* 99, 225502 (2007).
- [43] D. Murali, B. K. Panigrahi, M. C. Valsakumar, S. Chandra, C. S. Sundar, and B. Raj, The role of minor alloying elements on the stability and dispersion of yttria nanoclusters in nanostructured ferritic alloys: An ab initio study, *J. Nucl. Mater.* 403, 113 (2010).
- [44] A. Claisse and P. Olsson, First-principles calculations of (Y, Ti, O) cluster formation in body centred cubic iron-chromium, *Nucl. Instrum. Methods Phys. Res., B* 303, 18 (2013).
- [45] M. Methfessel and A. T. Paxton, High-precision sampling for Brillouin-zone integration in metals, *Phys. Rev. B* 40, 3616 (1989).
- [46] Y. Jiang, J. R. Smith, and G. R. Odette, Formation of Y-Ti-O nanoclusters in nanostructured ferritic alloys: A first-principles study, *Phys. Rev. B* 79, 064103 (2009).
- [47] C. Barouh, T. Schuler, C. C. Fu, and M. Nastar, Interaction between vacancies and interstitial solutes (C, N, and O) in  $\alpha$ -Fe: From electronic structure to thermodynamics, *Phys. Rev. B* 90, 054112 (2014).
- [48] D. Murali, M. Posselt, and M. Schiwarth, First-principles calculation of defect free energies: General aspects illustrated in the case of bcc Fe, *Phys. Rev. B* 92, 064103 (2015).
- [49] A. J. Samin, D. A. Andersson, E. F. Holby, and B. P. Uberuaga, Ab initio based examination of the kinetics and thermodynamics of oxygen in Fe-Cr alloys, *Phys. Rev. B* 99 (2019).
- [50] <http://theory.cm.utexas.edu/henkelman/code/bader/>.
- [51] L. Messina, M. Nastar, T. Garnier, C. Domain, and P. Olsson, Exactab initio transport coefficients in bccFe-X (X=Cr,Cu,Mn,Ni,P,Si) dilute alloys, *Phys. Rev. B* 90, 104203 (2014).
- [52] L. Messina, M. Nastar, N. Sandberg, and P. Olsson, Systematic electronic-structure investigation of substitutional impurity diffusion and flux coupling in bcc iron, *Phys. Rev. B* 93, 184302 (2016).
- [53] M. Mock and K. Albe, Diffusion of yttrium in bcc-iron studied by kinetic Monte Carlo simulations, *J. Nucl. Mater.* 494, 157 (2017).

- [54] A. C. Arokiam, A. V. Barashev, D. J. Bacon, and Y. N. Osetsky, Simulation of copper atom diffusion via the vacancy mechanism in a dilute Fe-Cu alloy, *Phys. Rev. B* 71 (2005).
- [55] T. Schuler and M. Nastar, Transport properties of dilute  $\alpha$ -Fe(X) solid solutions (X= C, N, O), *Phys. Rev. B* 93 (2016).
- [56] T. Schuler, L. Messina, and M. Nastar, KineCluE: a Kinetic Cluster Expansion code to compute transport coefficients beyond the dilute limit, *Computat. Mater. Sci.* 172, 109191 (2020).
- [57] T. Schuler, M. Nastar, and L. Messina, Mass-transport properties of ternary Fe(C,O) alloys revealed by multicomponent cluster synergies, *Physical Review Materials* 4 (2020).
- [58] X. Wang, M. Posselt, and J. Faßbender, Influence of substitutional atoms on the diffusion of oxygen in dilute iron alloys, *Phys. Rev. B* 98 (2018).
- [59] D. Sheppard, P. Xiao, W. Chemelewski, D. D. Johnson, and G. Henkelman, A generalized solid-state nudged elastic band method, *J. Chem. Phys.* 136, 074103 (2012).
- [60] <http://theory.cm.utexas.edu/henkelman/code/>.
- [61] S. Y. Huang, D. L. Worthington, M. Asta, V. Ozolins, G. Ghosh, and P. K. Liaw, Calculation of impurity diffusivities in  $\alpha$ -Fe using first-principles methods, *Acta Mater.* 58, 1982 (2010).
- [62] C. Domain and C. S. Becquart, Ab initio calculations of defects in Fe and dilute Fe-Cu alloys, *Phys. Rev. B* 65 (2001).
- [63] S. Choudhury, L. Barnard, J. D. Tucker, T. R. Allen, B. D. Wirth, M. Asta, and D. Morgan, Ab-initio based modeling of diffusion in dilute bcc Fe-Ni and Fe-Cr alloys and implications for radiation induced segregation, *J. Nucl. Mater.* 411, 1 (2011).
- [64] H. Amara, C. C. Fu, F. Soisson, and P. Maugis, Aluminum and vacancies in iron: Dissolution, diffusion, and clustering, *Phys. Rev. B* 81 (2010).
- [65] K. L. Wong, H.-J. Lee, J.-H. Shim, B. Sadigh, and B. D. Wirth, Multiscale modeling of point defect interactions in Fe-Cr alloys, *J. Nucl. Mater.* 386-388, 227 (2009).
- [66] C. C. Fu, J. D. Torre, F. Willaime, J. L. Bocquet, and A. Barbu, Multiscale modelling of defect kinetics in irradiated iron, *Nat. Mater.* 4, 68 (2004).
- [67] T. Schuler, C. Barouh, M. Nastar, and C. C. Fu, Equilibrium Vacancy Concentration Driven by Undetectable Impurities, *Phys. Rev. Lett.* 115, 015501 (2015).
- [68] E. A. Marquis, J. M. Hyde, D. W. Saxey, S. Lozano-Perez, V. d. Castro, D. Hudson, C. A. Williams, S. Humphry-Baker, and G. D. Smith, Nuclear reactor materials at the atomic scale, *Mater. Today* 12, 30 (2008).
- [69] M. K. Miller, D. T. Hoelzer, E. A. Kenik, and K. F. Russell, Nanometer scale precipitation in ferritic MA/ODS alloy MA957, *J. Nucl. Mater.* 329-333, 338 (2004).
- [70] H. Sakasegawa, F. Legendre, L. Boulanger, M. Brocq, L. Chaffron, T. Cozzika, J. Malaplate, J. Henry, and Y. d. Carlan, Stability of non-stoichiometric clusters in the MA957 ODS ferritic alloy, *J. Nucl. Mater.* 417, 229 (2011).

- [71] G. R. Odette, M. J. Alinger, and B. D. Wirth, Recent Developments in Irradiation-Resistant Steels, *Annu. Rev. Mater. Res.* 38, 471 (2008).
- [72] M. J. Alinger, G. R. Odette, and D. T. Hoelzer, On the role of alloy composition and processing parameters in nanocluster formation and dispersion strengthening in nanostructured ferritic alloys, *Acta Mater.* 57, 392 (2009).
- [73] C. C. Eiselt, M. Klimenkov, R. Lindau, and A. Möslang, Characteristic results and prospects of the 13Cr–1W–0.3Ti–0.3Y<sub>2</sub>O<sub>3</sub> ODS steel, *J. Nucl. Mater.* 386-388, 525 (2009).
- [74] P. He, M. Klimenkov, R. Lindau, and A. Möslang, Characterization of precipitates in nano structured 14% Cr ODS alloys for fusion application, *J. Nucl. Mater.* 428, 131 (2012).
- [75] A. J. London *et al.*, Effect of Ti and Cr on dispersion, structure and composition of oxide nano-particles in model ODS alloys, *Acta Mater.* 97, 223 (2015).
- [76] W. M. Lomer, Point defects and diffusion in metals and alloys, *Vakansii i drugie tochechnye defekty v metallakh i splavakh*, 99 (1958).
- [77] M. Posselt, D. Murali, and B. K. Panigrahi, Energetics, structure and composition of nanoclusters in oxide dispersion strengthened Fe–Cr alloys, *Model. Simul. Mater. Sci. Eng.* 22, 085003 (2014).
- [78] T. Schuler, M. Nastar, and F. Soisson, Vacancy-induced dissolution of precipitates in out-of-equilibrium systems: A test case of FeX (X=C,N,O) alloys, *Phys. Rev. B* 95 (2017).
- [79] J. Crangle and G. M. Goodman, The magnetization of pure iron and nickel, *Proc. R. Soc. A* 321, 477 (1971).
- [80] M. K. Miller, C. L. Fu, M. Krcmar, D. T. Hoelzer, and C. T. Liu, Vacancies as a constitutive element for the design of nanocluster-strengthened ferritic steels, *Front. Mater. Sci. China* 3, 9 (2008).
- [81] J. Xu, C. T. Liu, M. K. Miller, and H. Chen, Nanocluster-associated vacancies in nanocluster-strengthened ferritic steel as seen via positron-lifetime spectroscopy, *Phys. Rev. B* 79 (2009).
- [82] X. L. Wang, C. T. Liu, U. Keiderling, A. D. Stoica, L. Yang, M. K. Miller, C. L. Fu, D. Ma, and K. An, Unusual thermal stability of nano-structured ferritic alloys, *J. Alloys Compd.* 529, 96 (2012).
- [83] M. Vallinayagam, M. Posselt, and J. Fassbender, Interaction of O-Y and O-Y-Ti clusters embedded in bcc Fe with He, vacancies and self-interstitial atoms, *J. Phys.: Condens. Matter* 31, 485702 (2019).



## Appendix I

Related to Chapter 3: Influence of substitutional atoms on the diffusion of oxygen in dilute iron alloys

A. Volume change  $\Delta V(X) = V(X) - V_0$  and dimensions of the supercell obtained after placing oxygen on an octahedral interstitial site, or after replacing a Fe atom by Si, P, S, Ti, Cr, Mn, Ni, Y, Mo, or W, and subsequent relaxation.

In the case of an isotropic expansion/contraction only one supercell dimension is given while for tetragonal distortions the first line is related to the two equivalent directions (a) whereas the second line is related the third direction (b). In perfect bcc Fe the supercell dimension is 11.328 Å.

$X$	$\Delta V$ (Å <sup>3</sup> )	supercell dimension $d$ (Å)
O	13.477	11.342 (a) 11.407 (b)
Al	2.3963	11.335
Si	-0.0529	11.328
P	-1.1611	11.325
S	0.8578	11.331
Ti	4.0146	11.339
Cr	2.2522	11.334
Mn	2.5198	11.335
Ni	2.0916	11.334
Y	14.322	11.366
Mo	6.6809	11.346
W	6.4006	11.345

**B. Effective volume change  $\delta V$  ( $\text{\AA}^3$ ) (first line) and supercell dimensions  $d$  ( $\text{\AA}$ ) obtained after relaxation of a supercell containing an oxygen-solute pair.**

$\delta V = \Delta V(O-X) - \Delta V(X) - \Delta V(O)$ , where  $X$  and  $\Delta V$  denote the solute and the difference to the volume of a supercell with perfect bcc Fe, respectively. In the case of a tetragonal distortion the first line is related to the two equivalent directions (a) whereas the second line is related the third direction (b). In the case of an orthorhombic distortion three lines (a), (b), and (c) are given.

$O-X$	1nn	2nn	5nn	6nn	9nna	9nnb	10nn
O-Al	-2.1348	-1.3361	-0.5950	-0.3472	0.0142	-1.6040	0.0443
	11.345 (a)	11.347 (a)	11.345 (a)	11.349 (a)	11.348 (a)	11.344 (a)	11.346 (a)
	11.401 (b)	11.404 (b)	11.346 (b)	11.409 (b)	11.413 (b)	11.409 (b)	11.347 (b)
			11.413 (c)				11.416 (c)
O-Si	-1.4890	0.4775	-0.5243	-0.3244	-0.0213	-1.5066	0.2844
	11.345 (a)	11.349 (a)	11.337 (a)	11.343 (a)	11.341 (a)	11.342 (a)	11.340 (a)
	11.388 (b)	11.397 (b)	11.342 (b)	11.401 (b)	11.408 (b)	11.394 (b)	11.341 (b)
			11.407 (c)				11.411 (c)
O-P	-0.5172	2.2862	0.0412	-0.2388	0.2623	-0.9629	0.4865

	11.346 (a) 11.384 (b)	11.348 (a) 11.404 (b)	11.337 (a) 11.341 (b) 11.403 (c)	11.342 (a) 11.395 (b)	11.339 (a) 11.405 (b)	11.346 (a) 11.382 (b)	11.337 (a) 11.340 (b) 11.407 (c)
O-S	1.8078 11.346 (a) 11.418 (b)	2.1176 11.349 (a) 11.415 (b)	0.9043 11.343 (a) 11.349 (b) 11.412 (c)	0.0573 11.350 (a) 11.397 (b)	0.3936 11.345 (a) 11.409 (b)	-1.0893 11.354 (a) 11.381 (b)	0.7449 11.344 (a) 11.348 (b) 11.411 (c)
O-Ti	-0.3046 11.349 (a) 11.421 (b)	-0.6531 11.351 (a) 11.414 (b)	-0.2654 11.350 (a) 11.351 (b) 11.418 (c)	-0.2914 11.351 (a) 11.417 (b)	0.0155 11.352 (a) 11.417 (b)	-0.1074 11.347 (a) 11.427 (b)	-0.3123 11.351 (a) 11.417 (b)
O-Cr	-1.0385 11.342 (a) 11.416 (b)	-0.4087 11.346 (a) 11.413 (b)	-0.0727 11.348 (a) 11.411 (b)	-0.1192 11.346 (a) 11.414 (b)	0.1017 11.348 (a) 11.412 (b)	0.1486 11.344 (a) 11.421 (b)	0.1648 11.347 (a) 11.348 (b) 11.414 (c)

O-Mn	-2.8018 11.339 (a) 11.410 (b)	-3.1639 11.339 (a) 11.407 (b)	-3.3475 11.339 (a) 11.341 (b) 11.404 (c)	-0.7583 11.347 (a) 11.411 (b)	-2.7973 11.342 (a) 11.404 (b)	-3.0893 11.340 (a) 11.405 (b)	-2.8537 11.341 (a) 11.406 (b)
O-Ni	-0.7296 11.342 (a) 11.417 (b)	-0.3337 11.348 (a) 11.408 (b)	0.2285 11.347 (a) 11.349 (b) 11.412 (c)	0.5041 11.349 (a) 11.412 (b)	0.5706 11.348 (a) 11.414 (b)	1.1740 11.350 (a) 11.415 (b)	0.8155 11.348 (a) 11.349 (b) 11.416 (c)
O-Y	1.0245 11.375 (a) 11.459 (b)	-0.7925 11.383 (a) 11.428 (b)	-0.9586 11.362 (a) 11.385 (b) 11.446 (c)	0.0156 11.383 (a) 11.434 (b)	0.0777 11.376 (a) 11.449 (b)	0.3062 11.377 (a) 11.449 (b)	0.1376 11.375 (a) 11.379 (b) 11.448 (c)
O-Mo	0.1926 11.349 (a)	-1.2846 11.356 (a)	-1.0606 11.357 (a)	-0.8950 11.355 (a)	-0.8549 11.357 (a)	-0.4869 11.351 (a)	-0.8711 11.356 (a)

	11.445 (b)	11.419 (b)	11.420 (b)	11.425 (b)	11.421 (b)	11.435 (b)	11.423 (b)
O-W	1.0911	-0.6568	-0.2163	-0.2546	-0.3009	0.1400	-0.2373
	11.352 (a)	11.358 (a)	11.357 (a)	11.355 (a)	11.358 (a)	11.352 (a)	11.357 (a)
	11.445 (b)	11.419 (b)	11.359 (b)	11.427 (b)	11.421 (b)	11.437 (b)	11.358 (b)
			11.422 (c)				11.423 (c)

## Appendix II

Related to Chapter 3: Influence of substitutional atoms on the diffusion of oxygen in dilute iron alloys

### Qualitative interpretation of the dependence of the binding energy of the oxygen-solute pair on the kind of the substitutional solute

The dependence of the binding energy of the oxygen-solute pair on the type of the solute was investigated by studying the following characteristic quantities: (i) partial density of electronic states, (ii) magnetic moment, (iii) charge transfer, (iv) volume change of the supercell, (v) distance between the two atoms belonging to the pair. It was found that the results concerning the charge transfer determined by Bader analysis [Bader] seem to be most suitable for a qualitative interpretation of the trends found for the binding energy. For the particular oxygen solute pair the number of valence electrons considered in the pseudopotential (VASP POTCAR file), the number of valence electrons obtained by Bader analysis and the corresponding gain (positive) or loss (negative) of “electrons” (or negative charges) are shown in the **Table** below. The binding energy of the pairs is also given. If the pair is at the first neighbor distance (cf. Fig. 3.1 of Chapter 3) in most cases a significant attractive interaction occurs if the following two criteria are fulfilled simultaneously: Oxygen gains more than about 0.4 “electrons” and the solute loses more than about 0.6 “electrons”. This indicates an ionic-like bond. With the exception of the O-S and the O-Y pair, in the other cases the ionic character of one of the partners is obviously not sufficiently pronounced for an attraction. The **Figure** below depicts the binding energy of the O-solute pairs as function of their distance after relaxation. The unrelaxed distances according to Fig. 3.1 of Chapter 3 are also given. In all cases the (relaxed) distance between first-neighbor pairs is higher than the unrelaxed one. The largest increase is found for the O-S, O-Y, O-Mo, and O-W pairs. In these cases the distance between O and the substitutional solute is significantly higher than that to one or more of the neighboring Fe atoms, which may also explain the two exceptions mentioned above. It was found that the O-S pair forms a  $\langle 100 \rangle$  dumbbell that occupies a bcc lattice site. The distance between O (S) and this lattice site is about 1.362 Å (0.925 Å). The distance between five neighboring Fe atoms to O is smaller than the O-S distance, and the distance between five neighboring Fe atoms to S is also smaller than this pair distance. However, there is nearly no net transfer of electrons from these neighboring Fe atoms

to O or S. On the other hand, in total the O-S pair gains about one electron which might indicate a covalent-type bond and the formation of a kind of molecule inside bcc Fe. Furthermore, the **Figure** demonstrates that with increasing distance between O and a substitutional solute this distance approaches the value for the unrelaxed distance. Some peculiarities are found for the O-Si, O-P, and O-S pairs at second-neighbor distance. Here the (relaxed) distance is much larger than for the other pairs. Much more Fe atoms than expected from simple geometrical considerations based on Fig. 3.1 of Chapter 3 have a distance to atoms of the pair which is smaller than the pair distance. The O-S pair forms a kind of <110> dumbbell with a distance between O (S) to the respective bcc lattice site of about 2.172 Å (0.501 Å). The charge transfer from two surrounding Fe atoms may be the cause that the pair gains about one electron.

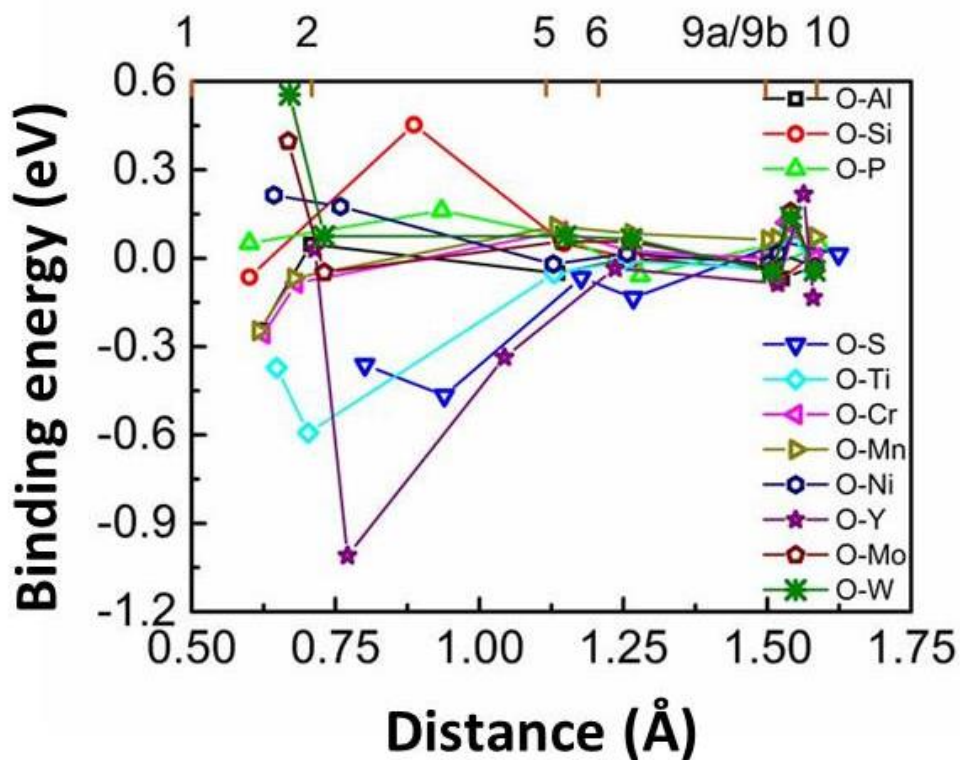


**Figure:** Binding energy of the O-solute pairs in dependence on the distance between O and the substitutional solute after relaxation. The nominal neighbor distances (before relaxation) are given on the top axis.

This could be again an indication for the formation of a kind of O-S molecule in bcc Fe. Due to the complex situation regarding the atomic configuration of the O-solute pair and the surrounding Fe atoms it cannot be expected that the above criteria based

on a simple charge transfer can be also applied to all pairs at 2<sup>nd</sup> distance. However, these criteria may be also used to interpret qualitatively the values of the binding energy of the O-Si, O-P, O-Ti, O-Cr, O-Mn, O-Ni, and O-Y pairs.

**Table:** Correlation between the binding energy of the O-solute pair and the results of the Bader analysis.

First-neighbor pair	$E_{bind}$ (eV)	$N_{valence\ electrons}$ in POTCAR	$N_{valence\ electrons}$ from Bader analysis	Gain/loss of "electrons"
O	-0.243	6	6.659	0.659
Al		3	0.669	-2.331
O	-0.064	6	6.159	0.159
Si		4	0.923	-3.077
O	0.051	6	6.212	0.212
P		5	3.237	-1.763
O	-0.361	6	7.039	1.039
S		6	5.957	-0.043
O	-0.372	6	6.381	0.381
Ti		12	10.648	-1.352
O	-0.257	6	6.699	0.699
Cr		12	10.862	-1.138
O	-0.246	6	6.918	0.918
Mn		13	12.316	-0.684
O	0.214	6	7.116	1.116
Ni		10	9.825	-0.175
O	0.031	6	6.817	0.817
Y		11	9.356	-1.644
O	0.397	6	6.119	0.119
Mo		14	12.478	-1.522
O	0.555	6	6.125	0.125
W		12	10.175	-1.825

Second-neighbor pair	$E_{bind}$ (eV)	$N_{valence\ electrons}$ in POTCAR	$N_{valence\ electrons}$ from Bader analysis	Gain/loss of "electrons"
----------------------	-----------------	------------------------------------	--	--------------------------



O	0.047	6	6.714	0.714
Al		3	1.413	-1.587
O	0.453	6	6.924	0.924
Si		4	3.457	-0.543
O	0.161	6	6.663	0.663
P		5	4.930	-0.070
O	-0.466	6	6.475	0.475
S		6	6.485	0.485
O	-0.593	6	6.798	0.798
Ti		12	10.455	-1.545
O	-0.085	6	6.794	0.794
Cr		12	11.480	-0.520
O	-0.068	6	6.987	0.987
Mn		13	12.630	-0.370
O	0.175	6	6.971	0.971
Ni		10	10.001	0.001
O	-1.010	6	6.891	0.891
Y		11	9.332	-1.668
O	-0.048	6	6.766	0.766
Mo		14	12.511	-1.489
O	0.075	6	6.816	0.816
W		12	9.967	-2.033

[Bader] <http://theory.cm.utexas.edu/henkelman/code/bader/>

## Appendix III

Related to Chapter 4: Efficient calculation method for the diffusion coefficient of interstitial solutes in dilute alloys

Comparison of the results obtained by the AKMC-based calculation method with those calculated by the cluster expansion approach of diffusion based on the self-consistent mean field (SCMF) method ([A], [B]): The example of O migration in a dilute iron alloy with a small amount of Ti

Results obtained by the method described in Chapter 4 were compared with those calculated by the method presented in Refs. [A] and [B]. The figure below shows the case of O diffusion in a dilute iron alloy with a small amount of Ti. Dr. Luca Messina (*DEN-Service de Recherches de Métallurgie Physique, CEA, Université Paris-Saclay, F-91191 Gif-sur-Yvette, France, and KTH Royal Institute of Technology, Nuclear Engineering, SE-114 21 Stockholm, Sweden*) performed the calculations with the code KineCluE. We are very grateful to Dr. Messina for providing us his results. In both calculations the same DFT data for the migration barriers were used. The agreement between results of both methods is very good. Therefore, one may assume that such an agreement also exists for other application considered in this thesis.

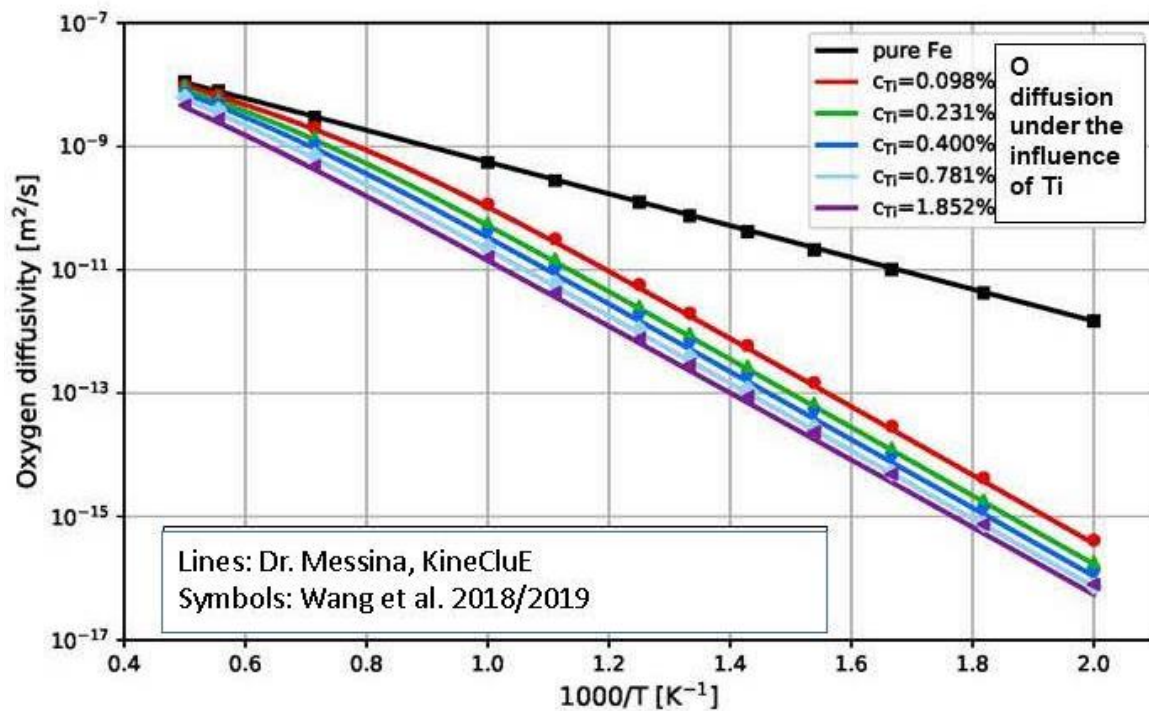


**Figure.** Dependence of the oxygen diffusion coefficient on temperature and on Ti concentration [lines: SCMF results obtained by Dr. Messina, symbols: results of our AKMC data (cf. Fig. 3.5 in Chapter 3 and Fig. 4.5 in Chapter 4)].

### References

- [A] T. Schuler and M. Nastar, Phys. Rev. B **93**, 224101 (2016).
- [B] T. Schuler, L. Messina, and M. Nastar, Computat, Mater. Sci. **172**, 109191 (2020).

## Appendix IV

Related to chapter 5: Mutual dependence of oxygen and vacancy diffusion in bcc Fe and dilute iron alloys

Data used in section 5.5 of the chapter 5

Fig. 1 shows the thermal solubility data of Frank *et al.* [A], Takada *et al.* [B], and Swisher *et al.* [C]. Frank *et al.* [A] obtained the data from a critical review of results published before 1967. The data of Takada *et al.* [B] were obtained by assuming equilibrium between Fe and FeO. Therefore, the oxygen concentration determined by these authors corresponds to that at the surface of the specimen where the equilibrium is maintained using FeO powder. It should be mentioned that this equilibrium was also considered in the paper of Frank *et al.* [A]. Furthermore, solubility data obtained from the theoretical work of Murali *et al.* [D] are depicted.

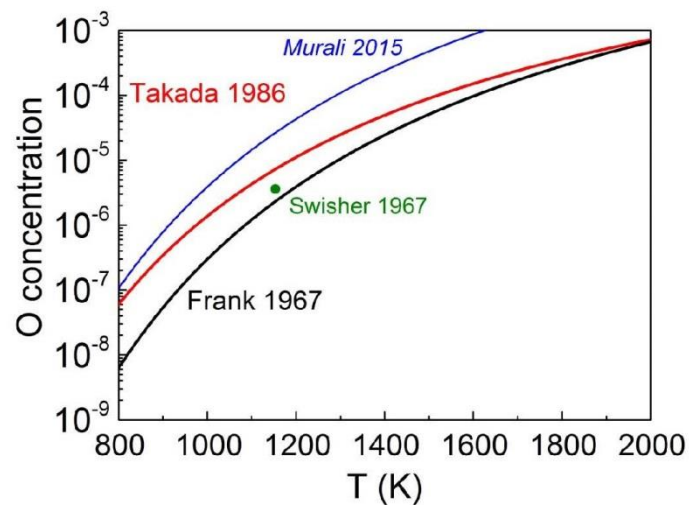


**Fig. 1** Thermal solubility limit of oxygen in pure Fe.

Figs. 2 (a) and (b) illustrate the concentration of monomers and clusters used in the calculation of oxygen diffusion [results are shown in Fig. 5.11 (a) of chapter 5] assuming temporary Ov and  $O_2v$  cluster formation (a) or temporary Ov formation only (b).

Figs. 2 (c) and (d) show the concentrations of monomers and clusters used to determine the vacancy diffusion coefficient (results are shown in Fig. 5.11 (b) of chapter

5) assuming temporary Ov and Ov<sub>2</sub> cluster formation (c) or temporary Ov formation only (d). Due to the very low concentration and the relatively low binding energy of Ov<sub>2</sub> the concentrations of O and Ov are nearly identical in both figures.

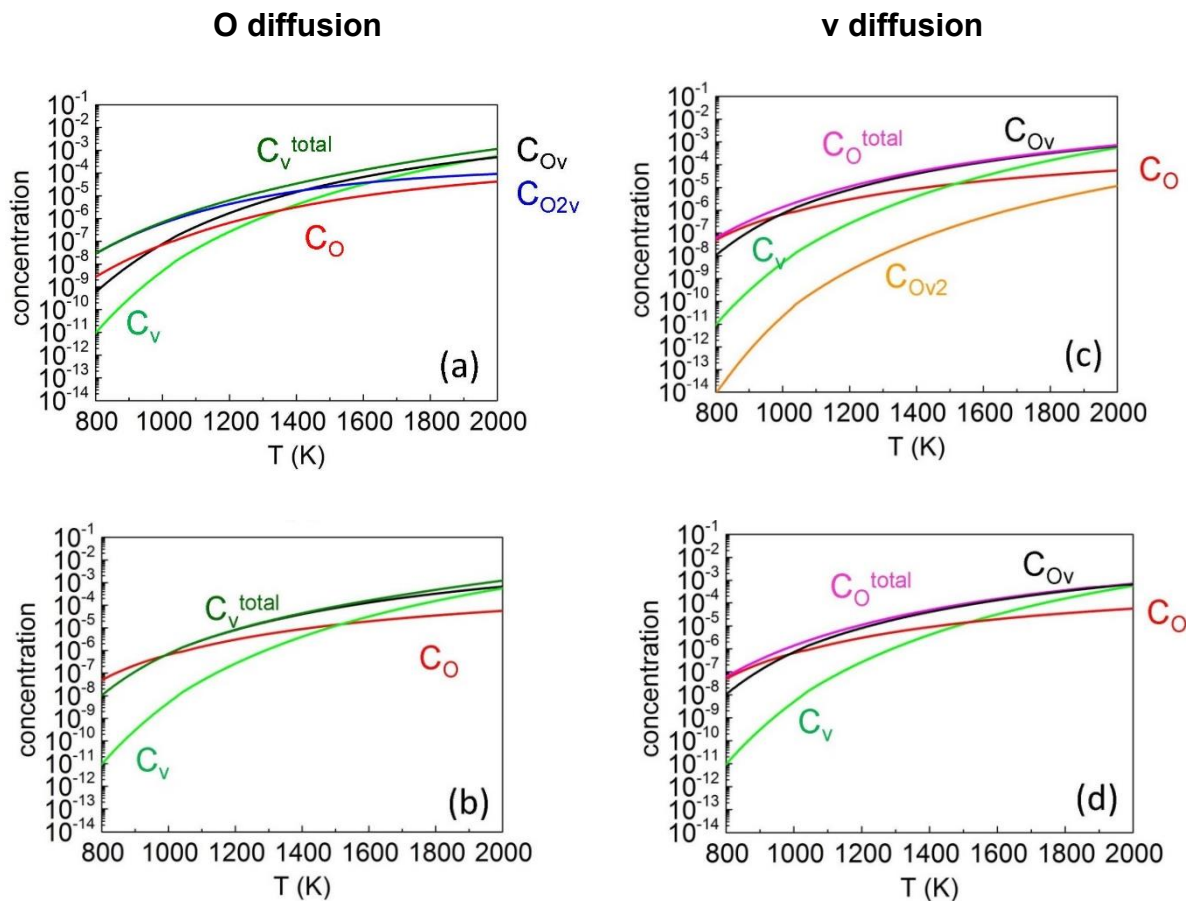


**Fig. 2** Concentration of monomers and clusters used in the calculation of oxygen (a-b) and vacancy (c-d) diffusion. The total vacancy and oxygen concentrations are also depicted.

### References

- [A] W. Frank, H. J. Engell, and A. Seeger, Z. Metallkd. **58**, 452 (1967).
- [B] J. Takada, S. Yamamoto, and M. Adachi, Z. Metallkd. **77**, 6 (1986).
- [C] J. H. Swisher and E. T. Turkdogan, Trans. Met. Soc. AIME **426**, 239 (1967).
- [D] D. Murali, M. Posselt, and M. Schiwarth, Phys. Rev. B **92**, 064103 (2015).

## Appendix V

Related to chapter 5: Mutual dependence of oxygen and vacancy diffusion in bcc Fe and dilute iron alloys

Diffusion coefficients of O and v in bcc Fe containing a pre-existing concentration of oxygen: Calculation using a further generalization of the AKMC-based efficient method

In the following bcc Fe with an oxygen concentration  $C_O^{\text{total}}$  close to the thermal solubility is considered. Due to pre-existing oxygen, in thermal equilibrium the total vacancy concentration is higher than in perfect iron due to the strong attraction between O and v. During migration O may be temporarily trapped by v (formation of a Ov pair), by Ov (formation of a  $O_2v$  cluster) and by other clusters containing O and v. During vacancy diffusion v may be temporarily trapped by O (formation of a Ov pair), by Ov (formation of a  $Ov_2$  cluster), etc. In the following only trapping by v or O and Ov is considered.

### **Oxygen diffusion**

The product of the O diffusion coefficient and time corresponds to a total sum of squared displacements of the migrating oxygen. This total sum consists of the squared displacements in the interaction regions with v and Ov, and in perfect bcc Fe (index “free”):

$$Dt_{\text{total}} = D_{\text{free}}t_{\text{free}} + D_{\text{inter}_v}t_{\text{inter}_v} + D_{\text{inter}_{Ov}}t_{\text{inter}_{Ov}} \quad (\text{A1})$$

with

$$t_{\text{total}} = t_{\text{free}} + t_{\text{inter}_v} + t_{\text{inter}_{Ov}} \quad (\text{A2})$$

$$1 = \frac{t_{\text{free}}}{t_{\text{total}}} + \frac{t_{\text{inter}_v}}{t_{\text{total}}} + \frac{t_{\text{inter}_{Ov}}}{t_{\text{total}}} \quad (\text{A3})$$

If one follows the diffusion of oxygen over a long time, one observes that O may be trapped by v, or by Ov, or it may migrate freely in pure bcc Fe. In other words, Ov pairs and  $O_2v$  clusters are temporarily formed. Thus, one can say that averaged over time the total oxygen concentration corresponds to the sum over the equilibrium

concentrations of O (monomer), Ov, and two times the equilibrium concentration of O<sub>2v</sub>. This may be written as

$$C_{\text{O}}^{\text{total}} = C_{\text{O}} + C_{\text{Ov}} + 2C_{\text{O2v}} \quad (\text{B1})$$

or

$$1 = \frac{C_{\text{O}}}{C_{\text{O}}^{\text{total}}} + \frac{C_{\text{Ov}}}{C_{\text{O}}^{\text{total}}} + \frac{2C_{\text{O2v}}}{C_{\text{O}}^{\text{total}}} \quad (\text{B2})$$

In the sense of this averaging the concentration ratios in (B2) may be identified with the time ratios in (A3).

The concentrations  $C_{\text{Ov}}$  and  $C_{\text{O2v}}$  can be determined using the method of Schuler *et al.* [A]:

$$\begin{aligned} C_{\text{v}}^{\text{total}} &= \sum_j n_j g_j \exp\left(\frac{\lambda_j}{k_B T}\right) \\ C_{\text{O}}^{\text{total}} &= \sum_j m_j(\text{O}) g_j \exp\left(\frac{\lambda_j}{k_B T}\right) \\ \lambda_j &= E_{\text{bind}}(j) + \sum_j (m_j(\text{O})\mu_{\text{O}} + n_j\mu_{\text{vFe}}) \end{aligned} \quad (\text{C})$$

where  $m_j$ ,  $n_j$  and  $g_j$  denote the number of oxygen and vacancies in the cluster  $j$ , and the number of the equivalent geometrical configurations of this cluster, respectively. The quantity  $E_{\text{bind}}$  is the total binding energy of the cluster  $j$ .  $\mu_{\text{O}}$  and  $\mu_{\text{vFe}}$  are the chemical potentials of O and v monomers, with  $\mu_{\text{vFe}} = -F_{\text{v}}^{\text{f}}$ , where  $F_{\text{v}}^{\text{f}}$  is the free formation energy of the vacancy in bcc Fe. The method described in Ref. [A] allows the consideration of clusters of different sizes. In the following we only consider Ov, O<sub>2v</sub> and Ov<sub>2</sub>. In the following, for a cluster with a given composition only the most relevant value of  $E_{\text{bind}}$  is taken into account. Then, the total O concentration may be also written as

$$C_{\text{O}}^{\text{total}} = 1 * 3 \exp\left(\frac{1 * \mu_{\text{O}}}{k_B T}\right) + 1 * 6 \exp\left(\frac{-E_{\text{bind}}^{\text{Ov}} + 1 * \mu_{\text{O}} + 1 * \mu_{\text{vFe}}}{k_B T}\right) + 2 * 3 \exp\left(\frac{-E_{\text{bind}}^{\text{O2v}} + 2 * \mu_{\text{O}} + 1 * \mu_{\text{vFe}}}{k_B T}\right) \quad (\text{D})$$

In this expression the stars show explicitly the multiplications with the corresponding values of  $m_j$ ,  $n_j$  and  $g_j$ . Data for the geometrical factor  $g_j$  may be found in Ref. [A].

Using

$$\exp\left(\frac{\mu_{\text{O}}}{k_B T}\right) = \frac{C_{\text{O}}}{3} \quad (\text{E1}) \quad \text{and} \quad C_{\text{v}} = \exp\left(\frac{\mu_{\text{vFe}}}{k_B T}\right) \quad (\text{E2})$$

leads to

$$C_{\text{O}}^{\text{total}} = C_{\text{O}} + 2C_{\text{O}}C_{\text{v}} \exp\left(\frac{-E_{\text{bind}}^{\text{Ov}}}{k_B T}\right) + 6\left(\frac{C_{\text{O}}}{3}\right)^2 C_{\text{v}} \exp\left(\frac{-E_{\text{bind}}^{\text{O2v}}}{k_B T}\right) \quad (\text{F})$$

Obviously, the last expression gives wrong results in the (hypothetical) limit of zero binding energies:

$$C_{\text{O}}^{\text{total}} = C_{\text{O}} + 2C_{\text{O}}C_{\text{v}} + \frac{2C_{\text{O}}^2}{3} C_{\text{v}} \quad (\text{G1})$$

which is not equal to  $C_{\text{O}}$ , as it should be.

Therefore, one may introduce corrections

$$C_{\text{O}}^{\text{total}} = C_{\text{O}} + 2C_{\text{O}}C_{\text{v}} \exp\left(\frac{-E_{\text{bind}}^{\text{Ov}}}{k_B T}\right) - 2C_{\text{O}}C_{\text{v}} + \frac{2C_{\text{O}}^2}{3} C_{\text{v}} \exp\left(\frac{-E_{\text{bind}}^{\text{O2v}}}{k_B T}\right) - \frac{2C_{\text{O}}^2}{3} C_{\text{v}} \quad (\text{G2})$$

which yield right results in that limit. However, for sufficiently high absolute values of binding energies, which is the standard application of Schuler's expressions, and due to the fact that  $C_{\text{v}} \ll 1$  and also  $C_{\text{O}} \ll 1$  the correction terms are negligible compared to the others.

If the term with  $E_{\text{bind}}^{\text{O2v}}$  is removed, the above expression corresponds to Lomer's equation [B]

$$C_{\text{O}}^{\text{total}} = C_{\text{O}} \left[ 1 - 2C_{\text{v}} + 2C_{\text{v}} \exp\left(\frac{-E_{\text{bind}}^{\text{Ov}}}{k_B T}\right) \right] \quad (\text{H})$$

which is also implicitly used in Eqs. (5.5) and (5.16) of chapter 5.

For the reasons mentioned above, the correction terms are neglected in the following.



Comparison of (B1) with (F) leads to

$$C_{Ov} = 2C_O C_v \exp\left(\frac{-E_{bind}^{Ov}}{k_B T}\right) \quad (I1) \quad C_{O2v} = \left(\frac{1}{3}\right) C_O^2 C_v \exp\left(\frac{-E_{bind}^{O2v}}{k_B T}\right) \quad (I2)$$

and therefore

$$\frac{t_{free}}{t_{total}} = \frac{C_O}{C_O^{total}} = \frac{1}{\left[1 + 2C_v \exp\left(\frac{-E_{bind}^{Ov}}{k_B T}\right) + \frac{2}{3} C_O C_v \exp\left(\frac{-E_{bind}^{O2v}}{k_B T}\right)\right]} \quad (J1)$$

$$\frac{t_{inter\_v}}{t_{total}} = \frac{C_{Ov}}{C_O^{total}} = \frac{2C_v \exp\left(\frac{-E_{bind}^{Ov}}{k_B T}\right)}{\left[1 + 2C_v \exp\left(\frac{-E_{bind}^{Ov}}{k_B T}\right) + \frac{2}{3} C_O C_v \exp\left(\frac{-E_{bind}^{O2v}}{k_B T}\right)\right]} \quad (J2)$$

$$\frac{t_{inter\_Ov}}{t_{total}} = \frac{2C_{O2v}}{C_O^{total}} = \frac{\frac{2}{3} C_O C_v \exp\left(\frac{-E_{bind}^{O2v}}{k_B T}\right)}{\left[1 + 2C_v \exp\left(\frac{-E_{bind}^{Ov}}{k_B T}\right) + \frac{2}{3} C_O C_v \exp\left(\frac{-E_{bind}^{O2v}}{k_B T}\right)\right]} \quad (J3)$$

The expression for  $t_{free} / t_{total}$ , together with Eq. (5.6) of chapter 5, is used in section 5.5 of chapter 5 to determine the O diffusion coefficient. The interaction terms in Eq. (A1) can be neglected since they are much lower than the term that contains  $D_{free}$ .

### Vacancy diffusion

The v diffusion under the influence of O and Ov is treated similarly to the above procedure for oxygen. That means the temporary formation of Ov and Ov<sub>2</sub> clusters must be considered. The total oxygen concentration is then given by

$$C_O^{total} = 1*3 \exp\left(\frac{1*\mu_O}{k_B T}\right) + 1*6 \exp\left(\frac{-E_{bind}^{Ov} + 1*\mu_O + 1*\mu_{vFe}}{k_B T}\right) + 1*1 \exp\left(\frac{-E_{bind}^{Ov2} + \mu_O + 2*\mu_{vFe}}{k_B T}\right) \quad (K1)$$

or

$$C_O^{total} = C_O + 2C_O C_v \exp\left(\frac{-E_{bind}^{Ov}}{k_B T}\right) + \frac{1}{3} C_O C_v^2 \exp\left(\frac{-E_{bind}^{Ov2}}{k_B T}\right) \quad (K2)$$

$$C_O^{total} = C_O + C_{Ov} + C_{Ov2} \quad (K3)$$

Then the monomer O concentration can be determined by

$$C_O = \frac{C_O^{\text{total}}}{1 + 2C_v \exp\left(\frac{-E_{bind}^{\text{Ov}}}{k_B T}\right) + \frac{1}{3} C_v^2 \exp\left(\frac{-E_{bind}^{\text{Ov2}}}{k_B T}\right)} \quad (\text{K4})$$

The total vacancy concentration is obtained from

$$C_v^{\text{total}} = C_v + C_{Ov} + 2C_{Ov2} \quad (\text{L})$$

with (see above)

$$C_{Ov2} = \frac{1}{3} C_O C_v^2 \exp\left(\frac{-E_{bind}^{\text{Ov2}}}{k_B T}\right) \quad (\text{M})$$

Then the relevant time ratio for vacancy diffusion is

$$\frac{t_{free}}{t_{total}} = \frac{C_v}{C_v^{\text{total}}} = \frac{1}{\left[1 + 2C_O \exp\left(\frac{-E_{bind}^{\text{Ov}}}{k_B T}\right) + \frac{2}{3} C_O C_v \exp\left(\frac{-E_{bind}^{\text{Ov2}}}{k_B T}\right)\right]} \quad (\text{N})$$

The expression for  $t_{free}/t_{total}$ , together with an equation similar to Eq. (5.6) of chapter 5, is used in section 5.5 of chapter 5 to determine the v diffusion coefficient.

The following DFT data for binding energies were determined and used in this work:

$$E_{bind}^{\text{Ov}} = -1.596 \text{ eV}, \quad E_{bind}^{\text{O2v}} = -3.349 \text{ eV}, \quad E_{bind}^{\text{Ov2}} = -2.502 \text{ eV}$$

## References

- [A] T. Schuler, C. Barouh, M. Nastar, and C. C. Fu, Phys. Rev. Lett. **115**, 015501 (2015).  
 [B] W. M. Lomer, *Vacancies and Other Point Defects in Metals and Alloys* (Institute of Metals, London, 1958), pp. 79–98.

## Publication list

### Thesis related

1. **X. Wang**, M. Posselt, J. Faßbender: Influence of substitutional atoms on the diffusion of oxygen in dilute iron alloys, *Phys. Rev. B* 98 (2018) 064103
2. **X. Wang**, J. Faßbender, M. Posselt: Efficient calculation methods for the diffusion coefficient of interstitial solutes in dilute alloys, *Materials* 12 (2019) 1491
3. **X. Wang**, J. Faßbender, M. Posselt: Mutual dependence of oxygen and vacancy diffusion in bcc Fe and dilute iron alloys, *Phys. Rev. B* 101 (2020) 174107

### Non-thesis-related

1. S. Prucnal, M. O. Liedke, **X. Wang** *et al.*: Dissolution of donor-vacancy clusters in heavily doped n-type germanium (submitted to Applied Physics Review)

### Conference presentations:

1. X. Wang; J. Faßbender; M. Posselt: Efficient calculation methods for the diffusion coefficient of interstitial solutes in dilute alloys, European Congress and Exhibition on Advanced Materials and Processes 2019, Sep. 1-5, 2019, Stockholm, Sweden. **Oral presentation**
2. X. Wang.; M. Posselt; J. Faßbender: Oxygen diffusion in bcc Fe under the influence of foreign atoms and vacancies, 9th Int. Multiscale Materials Modeling Conference (MMM 2018), Oct. 28 – Nov. 2, 2018, Osaka, Japan. **Oral presentation**
3. X. Wang.; M. Posselt; J. Faßbender: Diffusion of oxygen in bcc Fe under the influence of other foreign atoms, The 14th International Conference on Computer Simulation of Radiation Effects in Solids (COSIRES 2018), Jun.18.-22, 2018, Shanghai, China. **Poster**
4. X. Wang.; M. Posselt; J. Faßbender: Diffusion of oxygen in bcc Fe under the influence of other foreign atoms, Spring Meeting of the German Physical Society (DPG) and EPS-CMD27, March 11 – 16, 2018, Berlin, Germany. **Oral presentation**

5. X. Wang.; M. Posselt; J. Faßbender: Influence of foreign atoms on the diffusion of oxygen in bcc Fe, NSF/CECAM School on Computational Materials Science: From Basics to Applications, July 17 – 27, 2017, Lausanne, Switzerland. **Poster**

6. X. Wang.; M. Posselt; J. Faßbender: Influence of foreign atoms on the diffusion of oxygen in bcc Fe, 4th Int. Workshop on ODS materials, June 26 – 28, **2017**, Dresden, Germany. **Oral presentation**

## Curriculum Vitae

### 1 Personal data

Name: Xiaoshuang Wang

Birthday: 28 Jul. 1991

Birth place: Sichuan, China

### 2 Education

Sep.2006-Jul.2009 Deyang Middle school, China

Sep.2009-Jul.2013 Bachelor of Science

Sichuan University, China

Sep.2013-Jul.2016 Master of Engineering

Sichuan University, China

Oct.2016-Oct.2020 PhD. student

Helmholtz-Zentrum Dresden-Rossendorf, Germany

Technische Universität Dresden, Germany

### 3. short-term advanced school

Jul.17 – 27, 2017 NSF/CECAM School on Computational Materials Science: From Basics to Applications, Lausanne, Switzerland.

### 4. Teaching

Apr.2017-Jul.2017 Teaching assistant at Technische Universität Dresden, Germany

Lecture: Laboratory of Fundamental Physics

## Acknowledgements

Time passed so fast, and my four years' PhD life is coming to the end. I am grateful to have a chance to acknowledge the supports and kindness from people all around me during my PhD life.

I must begin with my supervisor Dr. Matthias Posselt. I still remember that at my first day in Helmholtz-Zentrum Dresden-Rossendorf, Dr. Posselt sat on the ground of my office to solve the connect problem of my computer. His patient guidance, encouragement and tolerance on my faults have accompanied me throughout the entire time of my work. I cannot imagine the PhD working life without the help of him.

I would like to show the greatest appreciation to my supervisor Prof. Jürgen Faßbender. I can always learn new knowledge through our fruitful discussion. His valuable suggestion and comments improve the quality of my PhD work.

I am grateful to colleagues in HZDR especially in FWI. Thanks for the support from Dr. Mao Wang, Dr. Ye Yuan, Dr. Chi Xu, Dr. Zhitao Zhang, and Dr. Binghuang Duan. I got the chance to learn a lot through their valuable suggestion.

I have to say Dresden is a magic city, where I meet a lot of friends. They are thanked here. Yuzhen, Ningning, Xuelin, Jin, Mo, Tian, Yufang, Mengyuan, Xu, Zhe, etc ... Life in Dresden is so colorful with them.

I would like to acknowledge the China Scholarship Council (CSC) for offering scholarship for my study in Germany.

I am very grateful to the Center for Information Services and High Performance Computing (ZIH) at Technische Universität Dresden and to the Department of Information Service and Computing at Helmholtz-Zentrum Dresden-Rossendorf for providing extensive computing time.

The work also contributes to the Joint Programme on Nuclear Materials (JPNM) of the European Energy Research Alliance (EERA).

Xiaoshuang Wang

Dresden

May, 2020

## Erklärung

Hiermit versichere ich, dass ich die vorliegende Arbeit ohne unzulässige Hilfe Dritter und ohne Benutzung anderer als der angegebenen Hilfsmittel angefertigt habe; die aus fremden Quellen direkt oder indirekt übernommenen Gedanken sind als solche kenntlich gemacht. Die Arbeit wurde bisher weder im Inland noch im Ausland in gleicher oder ähnlicher Form einer anderen Prüfungsbehörde vorgelegt.

Diese Dissertation wurde angefertigt im  
Helmholtz-Zentrum Dresden-Rossendorf  
Institut für Ionenstrahlphysik und Materialforschung  
Bautzner Landstr. 400, 01328 Dresden,

Die wissenschaftliche Betreuung der Arbeit erfolgte durch Prof. Dr. Jürgen  
Faßbender.

Ich versichere, an keiner Institution, auch nicht im Ausland, jemals den Antrag auf  
Eröffnung eines Promotionsverfahrens gestellt zu haben.

Ich erkenne die Promotionsordnung der Fakultät Mathematik und  
Naturwissenschaften der Technischen Universität Dresden an.

26.06.2020  
Xiaoshuang Wang